

Doctoral Thesis
Search for ${}^6_{\Lambda}\text{H}$ hypernucleus by the (π^-, K^+) reaction
at J-PARC

Hitoshi Sugimura



A dissertation submitted in partial fulfillment of
the requirements for the degree of

Doctor of Science

Department of Physics
Faculty of Science
Kyoto University

January, 2014

Abstract

A hypernucleus is a characteristic bound system of an ordinary nucleus and a few hyperon, such as Λ , Σ , Ξ . A Λ -hypernucleus consists of nucleons and one Λ hyperon. When a Λ hyperon is embedded into a nucleus, there are several interesting features theoretically expected for some specific neutron-rich hypernuclei. One example is the glue-like role of a Λ hyperon in the hypernuclei. The glue-like role gives a critical contribution to the binding especially around the proton- and neutron-drip lines, and may extend the boundary of nuclear stabilities. Another example is an effect of the Λ N- Σ N mixing. A non-zero isospin of the core nucleus is essential for the large mixing because the core nucleus is a buffer of the isospin to compensate the isospin difference between $\Lambda(I=0)$ and $\Sigma(I=1)$. Therefore, the studies on the neutron-rich Λ hypernuclei with a large isospin are important to understand the properties of the Λ N- Σ N mixing effect. To study its effects, we selected a ${}^6_{\Lambda}\text{H}$ hypernucleus which has one proton, four-neutron, and one Λ hyperon.

The present experiment was proposed aiming at a precise spectroscopic investigation of light neutron-rich Λ hypernuclei, ${}^6_{\Lambda}\text{H}$ by the (π^-, K^+) reaction at 1.2 GeV/c by using the SKS spectrometer (J-PARC E10). The FINUDA group reported the binding energy of ${}^6_{\Lambda}\text{H}$ based on three candidate events. We would like to much improve the precision of the binding energy and establish the existence in high statistics. By observing more than 100 events, not only the precise binding energy but also the production cross section can be obtained in a good statistical accuracy. It would be important in order to discuss the Λ N- Σ N mixing effect quantitatively. The structure of the ${}^6_{\Lambda}\text{H}$ will be revealed for the first time.

The ${}^6_{\Lambda}\text{H}$ production data by the ${}^6\text{Li}(\pi^-, K^+)$ reaction were taken for the first time in the K1.8 beam line of J-PARC Hadron Experimental Facility in two cycles in December 2012 and in January 2013. A ${}^6\text{Li}$ target 3.5 g/cm² in thickness was used. The total number of pions irradiated on the ${}^6\text{Li}$ target was 2.1×10^{12} .

In the missing-mass spectrum of ${}^6\text{Li}(\pi^-, K^+)$ reaction, no peak structure was observed. We estimated an upper limit of production cross section from the number of events with the missing-mass window. There were 3 events around the ${}^4_{\Lambda}\text{H}+2n$ threshold (5801.7 MeV/ c^2) We employed the upper limit of 6.68 events at 90% confidence level from the Poisson statistics, and the upper limit of production cross section was estimated to be 1.2 nb/sr at 90% confidence level.

Contents

1	Introduction	1
1.1	Neutron-rich Λ -hypernuclei	1
1.2	Experimental approaches for the neutron-rich Λ -hypernuclei	5
1.2.1	The $(K_{stopped}^-, \pi^+)$ reaction	5
1.2.2	(π^-, K^+) reaction	8
1.3	J-PARC E10	11
1.4	Theoretical approach for the ${}^6_{\Lambda}\text{H}$ hypernucleus	11
2	Experiment	15
2.1	Outline	15
2.2	J-PARC and Hadron experimental facility	15
2.3	K1.8 beam line	17
2.4	K1.8 beam line spectrometer	18
2.4.1	Particle ID counters	20
2.4.2	Tracking devices	23
2.5	Scattered-particle spectrometer (SKS)	27
2.6	Trigger	35
2.7	Data-acquisition system	38
2.8	Lithium-6 target	40
2.9	Data summary	41
3	Data Analysis	42
3.1	Outline	42
3.2	Analysis of beam	43
3.2.1	Identification of triggered beam particles	43
3.2.2	BFT analysis	43
3.2.3	BC3 and BC4 local tracking	45
3.2.4	Beam momentum reconstruction	48
3.3	Analysis of scattered particles	51
3.3.1	Hodoscope cut	51
3.3.2	SFT and SDC2 local tracking	51
3.3.3	SDC3 and SDC4 local tracking	51
3.3.4	Momentum reconstruction of a scattered particles	51
3.3.5	Particle identification in the SKS spectrometer	54
3.4	Vertex reconstruction	56

3.5	Analysis of the beam-through runs	58
3.6	Momentum correction	59
3.6.1	Overview	59
3.6.2	Momentum correction of scattered particles	59
3.6.3	Target energy loss and straggling	62
3.6.4	Momentum correction of beam pions	64
4	Experimental results	66
4.1	Good (π^- , K^+) events	66
4.2	Cross Section	68
4.2.1	Efficiency	69
4.3	Acceptance of SKS	79
4.4	Missing-mass spectrum of the ${}^6\text{Li}(\pi^-, K^+)$ reaction	81
5	Discussions	84
5.1	Analysis of ${}^1_2\Lambda\text{C}$	84
5.2	Analysis of the Σ^\pm	86
5.3	Background level	89
5.4	Estimation of upper limit	91
5.5	Structure of ${}^6_2\Lambda\text{H}$	92
6	Conclusion	93
A	Missing-mass spectrum of the ${}^6\text{Li}(\pi^-, K^+)$ reaction	96

List of Figures

1.1	Λ hypernuclear chart.	2
1.2	All the hypernuclear γ transitions observed and identified to date	3
1.3	Nuclear chart produced each reaction	6
1.4	Measurement of ($K_{stopped}^-, \pi^+$) reaction at KEK.	7
1.5	Evidence of 3 event of ${}^6_{\Lambda}\text{H}$ by FINUDA	8
1.6	The missing-mass spectrum of ${}^{10}\text{B}(\pi^-, K^+)$ reaction	9
1.7	Calculated inclusive excitation spectra	10
1.8	Theoretical calculation of ${}^6_{\Lambda}\text{H}$ binding energy.	12
1.9	${}^5\text{H}$ spectrum measured in coincidence with triton from the decay of the residual ${}^5\text{H}$ system [42].	13
1.10	Missing-mass spectra for the ${}^9\text{Be}(\pi^-, pt)\text{X}$ reaction	13
1.11	Missing-mass spectra for the ${}^9\text{Be}(\pi^-, dd)\text{X}$ reaction	14
2.1	A schematic view of J-PARC Facility	16
2.2	The schematic view of hadron experimental facility as of 2013.	16
2.3	Schematic view of K1.8 beam line	17
2.4	Typical beam profile at the target	18
2.5	Schematic view of K1.8 beam spectrometer.	19
2.6	The schematic view of GC.	21
2.7	A schematic view of BH2.	22
2.8	The structure of BFT	24
2.9	The cell structure of BC3·4	25
2.10	The picture of SSD.	26
2.11	Beam rate dependence of the SSD performances	27
2.12	A schematic view of the SKS	28
2.13	A schematic view of TOF.	30
2.14	Threshold and refractive index for Čerenkov radiation as a function of the momentum.	31
2.15	A schematic view of LAC.	31
2.16	A schematic view of LC.	32
2.17	Schematic view of SFT.	33
2.18	The cell structure of SDC3·4	34
2.19	PIK trigger logic diagram.	35
2.20	The selected TOF and LC segments region with the matrix trigger	36
2.21	Logic Scheme of the mass trigger	37
2.22	Diagram of the data-acquisition system.	39

2.23	The Picture of ${}^6\text{Li}$ target	40
3.1	Typical BH2 time spectrum of the incident beam particles	43
3.2	Slewing correction of BFT	44
3.3	Typical TDC distribution of BFT	44
3.4	Typical TDC distribution of one of BC3·4 layers	45
3.5	A scatter plot between the drift time and the drift length of one of the BC3·4 layers	46
3.6	Local position coordinate for the local straight tracking.	47
3.7	The VI and VO point in the K1.8 beam line spectrometer	47
3.8	(a) Typical residual distribution of one of the BC3·4 layers. (b) Typical χ^2 distribution of the BC3·4 tracking.	48
3.9	Typical distribution of the beam momentum at 1.2 GeV/ c	49
3.10	Typical distribution of XY and UV	50
3.11	Typical residual and χ^2 distributions of SFT·SDC2 local tracking.	52
3.12	Typical residual distribution of one of the SDC3·4 planes (left), and χ^2 distribution of SDC3·4 (right).	53
3.13	Typical χ^2 distribution of SKS tracking.	54
3.14	Scattered particle mass squared distribution for the ${}^6\text{Li}(\pi^-, K^+)$ data	55
3.15	The correlation of the mass squared and the momentum.	55
3.16	Typical distribution of the scattering angle difference	56
3.17	Distributions of a vertex and a closest distance.	57
3.18	The momentum difference between the two spectrometers.	58
3.19	The width of momentum difference	59
3.20	dx/dz and dy/dz correction for scattered particles	60
3.21	Distributions of the momentum difference between the two spectrometers with and without target	63
3.22	Momentum difference measured with the K1.8 beam line and the SKS. Filled circles represent beam through runs at beam momenta of 0.8, 0.9, 1.0 and 1.2 GeV/ c . Open circle represents momentum difference of the Σ^+ production run, where expected beam momentum is estimated with the mass difference from PDG value of Σ^+	65
4.1	Flow chart of the offline analysis	67
4.2	Time distribution of LAC in proton event in the (π, K) trigger.	72
4.3	The correlation of time-of-flight and scattering angle (dx/dz)	73
4.4	The SKS tracking efficiency as a function of the scattering angle.	74
4.5	The missing-mass resolution of Σ^- as a function of the χ^2_{sks}	75
4.6	The number of PIK tracks candidates.	76
4.7	Vertex reconstruction efficiency as a function of the scattering angle.	77
4.8	Scatter plot between the scattering angle and z-vertex distribution for the (π^-, K^+) data.	77
4.9	The acceptance of SKS in the 2.2 T mode.	80
4.10	The integrated acceptance of SKS in the 2.2 T mode.	81
4.11	Missing-mass spectrum of the ${}^6\text{Li}(\pi^-, K^+)$ reaction	83

5.1	Excitation energy spectrum of the $^{12}\text{C}(\pi^+, K^+)_{\Lambda}^{12}\text{C}$ reaction	85
5.2	Missing-mass spectrum of Σ^{\pm}	86
5.3	The differential cross section of the Σ^{-} production	87
5.4	The differential cross section of Σ^{+} production	87
5.5	The differential cross section of the Σ^{-} production compared with old experiment as a function of the beam momentum	88
5.6	The differential cross section of Σ^{+} production compared with old experiment as a function of the beam momentum	88
5.7	Background level in the over bound regions of the $^6\text{Li}(\pi^-, K^+)$ reaction .	90
5.8	Level structure of $^6_{\Lambda}\text{H}$ with respect to the particle decay threshold of $^4_{\Lambda}\text{H}+2n$	92

List of Tables

2.1	Design specifications of the K1.8 beam line spectrometer	19
2.2	Specifications of the particle identification counters in the beam line spectrometer	20
2.3	Specifications of the tracking devices in the beam line spectrometer.	23
2.4	Design specifications of the new SKS spectrometer at 2.16 T mode.	27
2.5	Specifications of the particle identification counters in the SKS spectrometer	29
2.6	Specifications of the tracking devices in the SKS spectrometer.	32
2.7	Summary of runs. Target material and thickness, and beam momentum and intensity are listed.	41
3.1	The position resolution of each layers.	46
3.2	Slit condition of ${}^6\text{Li}(\pi^-, K^+)$ production reaction	49
3.3	target energy loss and stragglings	62
3.4	momentum correction	64
4.1	The list of the experimental efficiency factors.	68
4.2	Typical materials in the spectrometers along the flight path.	78
A.1	The missing-mass spectrum of the ${}^6\text{Li}(\pi^-, K^+)$ reaction as a table	96

Chapter 1

Introduction

1.1 Neutron-rich Λ -hypernuclei

A hypernucleus is a characteristic bound system of a few hyperons, such as Λ , Σ , Ξ and an ordinary nucleus. A Λ -hypernucleus consists of one Λ hyperon and nucleons.

Hypernuclear investigations provide invaluable information on hadronic many-body systems by introducing a new degree of freedom “strangeness” [1, 2, 3]. New structures of baryonic many-body systems can be better studied with spectroscopic measurements. In particular, a Λ hyperon can be put deep inside a nucleus as an impurity and provides a sensitive probe of the nuclear interior. Since the Λ hyperon does not suffer from Pauli blocking with other nucleons, it can penetrate into the nuclear interior and form deeply-bound hypernuclear states. It is expected that new forms of hadronic many-body systems can be investigated using this new degree of freedom, strangeness, and hypernucleus is also a good tool to investigate the two-body Λ -N interaction.

Since the first discovery of a cosmic-ray induced hyperfragment production event in emulsion [4], various Λ -hypernuclei have been observed. The binding energies of light ($A < 16$) Λ hypernuclei were measured from their weak decays in emulsion, and the Λ potential depth was found to be $\sim 2/3$ that of the nucleon. However, at that time, the experimental data was limited to the binding energies of ground states, and excited states were not able to be investigated.

In 1970s and 1980s, extensive studies have been made with counter experiments by using K^- beams at the European Organization for Nuclear Research (CERN) and later at Brookhaven National Laboratory (BNL) [5, 6, 7]. Spectroscopic studies including excited states of hypernuclei had become possible with the in-flight (K^-, π^-) reaction. A noble method of the in-flight (K^-, π^-) reaction in an almost recoilless condition was introduced and hypernuclei such as ${}^9_{\Lambda}\text{Be}$, ${}^{12}_{\Lambda}\text{C}$ and ${}^{16}_{\Lambda}\text{O}$ were intensively studied [8, 9, 10, 11].

The use of (π^+, K^+) reaction began at the Alternating Gradient Synchrotron (AGS) of BNL and High Energy Accelerator Research Organization (KEK)-Proton Synchrotron [12, 13, 14, 15]. The (π^+, K^+) reaction selectively populates angular momentum stretched states because of a large momentum transfer of ~ 350 MeV/ c to a recoil hypernucleus. This is in contrast to the (K^-, π^-) reaction, which transfers a small momentum to a hypernucleus and therefore favors the excitation of substitutional states. By using this reaction, high-quality excitation energy spectra were measured for various Λ hypernuclei

and hypernuclear spectroscopy was established as a broadly applicable, quantitative tool up to ${}_{\Lambda}^{208}\text{Pb}$.

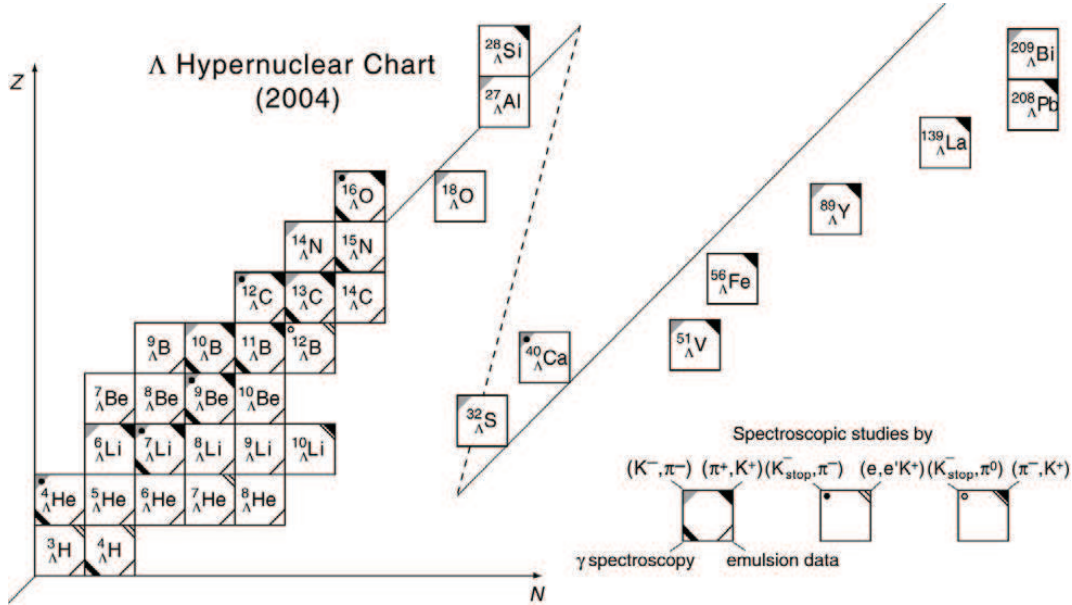


Figure 1.1: Λ hypernuclear chart. The experimentally identified Λ hypernuclei and the experimental methods used to study them (reaction spectroscopies of (K^-, π^-) , (π^+, K^+) , $(e, e'K^+)$, etc., γ spectroscopy, and the emulsion method) are shown.

In light Λ hypernuclei, the spin-dependent parts of the Λ -N interaction such as spin-spin, spin-orbit, and tensor interactions have important roles on fine level structures. A high energy resolution of less than a few 100 keV is required to measure the splitting because the spin-dependent Λ -N interactions are known to be very small. Precision spectroscopy has been carried out with unprecedented resolution of a few keV through the use of a germanium detector array called Hyperball [16]. It has provided new quantitative information on spin-spin, spin-orbit and tensor interactions of the Λ -N interaction by observing the fine structures as shown in Fig 1.2. Although, we have a long history of Λ -hypernuclei, the observed Λ hypernuclear species are limited as shown in Fig. 1.1.

On the other hand, as for the Σ hypernuclei, the observation of ${}_{\Sigma}^4\text{He}$ bound state by the in-flight (K^-, π^-) reaction at BNL [17] was one of the great success confirming of any bound state of hypernuclei containing Σ hyperon which was first claimed in KEK using $(K_{stopped}^-, \pi^\pm)$ reaction [18]. Existence of this bound state in ${}^4\text{He}$ was first predicted in theory by Harada *et al.* in 1990 [19]. According to their theory, a strong isospin-dependence of the Σ N interaction plays an important role in populating the rather narrow bound state. And no other bound states in medium to heavy Σ hypernuclei are expected after a measurement of ${}^{28}\text{Si}(\pi^-, K^+)$ reaction suggesting a strong repulsion of about 30 MeV [20].

Interesting property connecting Λ and Σ hypernuclei is the effect of the "AN- Σ N mixing". The AN- Σ N mixing was first discussed by Gibson *et al.* for s -shell Λ hypernuclei [21]. Since the mass difference of Λ and Σ , $M_\Sigma - M_\Lambda \sim 80 \text{ MeV}/c^2$ is narrower than that of ordinary nuclei, $M_\Delta - M_N \sim 290 \text{ MeV}/c^2$, this situation makes the effect

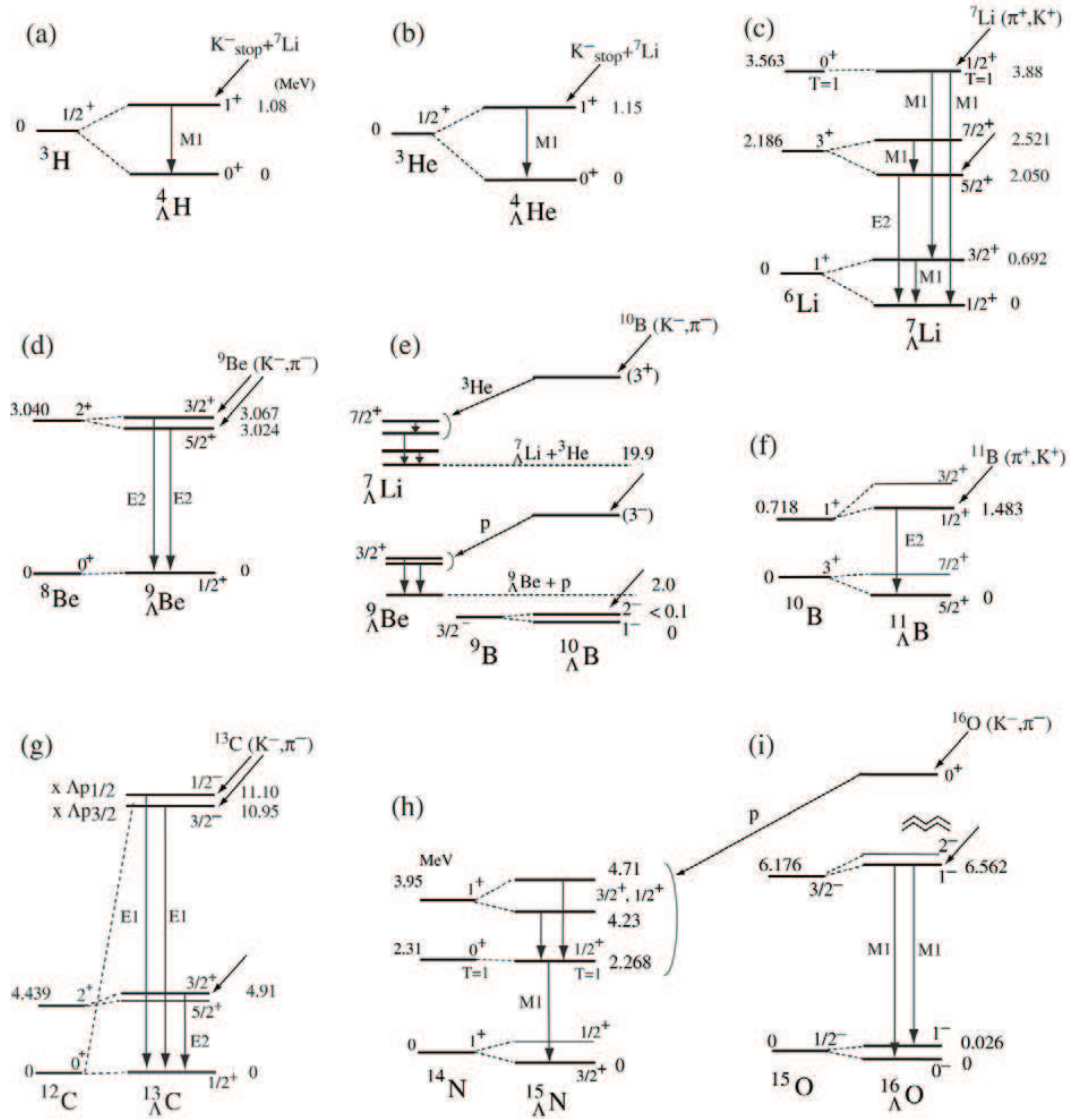


Figure 1.2: All the hypernuclear γ transitions observed and identified to date for ${}^4_{\Lambda}\text{H}$ [22], ${}^4_{\Lambda}\text{He}$ [23], ${}^7_{\Lambda}\text{Li}$ [24], ${}^9_{\Lambda}\text{Be}$ [25], ${}^{10}_{\Lambda}\text{B}$ [26], ${}^{11}_{\Lambda}\text{B}$ [27], ${}^{15}_{\Lambda}\text{N}$ [28], ${}^{16}_{\Lambda}\text{O}$ [28]. The level schemes of these hypernuclei with the energies (in MeV) and the assigned spins and parities are shown together with the reactions used to populate the excited states in γ spectroscopy experiments.

of the Λ N- Σ N coupling strong. A non-zero isospin of the core nucleus is essential for the large mixing because the core nucleus is a buffer of the isospin to compensate the isospin difference between Λ ($I=0$) and Σ ($I=1$). The idea has been extended to the coherent Λ N- Σ N mixing by Akaishi *et al.* to understand the binding energy of s -shell Λ -hypernuclei systematically [29]. The strong Λ N- Σ N coupling introduces an additional effective two-body attraction between Λ and nucleon.

Therefore, the studies on the neutron-rich Λ -hypernuclei with a large isospin are important to understand the properties of the Λ N- Σ N mixing effect. Since the Λ N- Σ N mixing induces the three-body Λ NN interaction, the mixing effect may play an important role in the high-density strange matter, such as the matter in the core of the neutron stars [30]. The study of the neutron-rich Λ hypernuclei is one of approaches to understand the details of the effect of the Λ hyperon at the boundary of stability of nuclei and the Λ NN three-body interaction.

To study these effects, we selected a ${}^6_{\Lambda}\text{H}$ hypernucleus which has one proton, four-neutron, and one Λ hyperon. We would expect large structure change of the core nucleus beyond the neutron drip line by the addition of a Λ hyperon. If it is bound, we would obtain information of Λ N- Σ N mixing effect from the binding energy and production cross section. The study of the ${}^6_{\Lambda}\text{H}$ hypernucleus also provide the information of the structure of ${}^5\text{H}$.

1.2 Experimental approaches for the neutron-rich Λ -hypernuclei

The single charge-exchange reaction (SCX), such as the $(e, e'K^+)$ reaction converts one proton to one Λ hyperon ($p \rightarrow \Lambda$). The double charge-exchange (DCX) reaction, such as the (K^-, π^+) and (π^-, K^+) reactions, converts two protons to one Λ hyperon and one neutron ($pp \rightarrow n\Lambda$). These two reactions are promising spectroscopic tools to access the Λ -hypernuclei close to the neutron drip-line [31]. Figure 1.3(b) shows the hypernuclei which have ever produced in the $A < 16$ region: purple and green colored ones were observed as hyperfragments in nuclear emulsion experiments. Although the chart looks already compatible with that of the ordinary nuclei, Fig 1.3(a), a variety of Λ hypernuclei are expected to exist due to a glue-like role of a Λ hyperon. By using the SCX or DCX reactions, wider areas can be accessed as shown in Fig 1.3(c).

1.2.1 The $(K^-_{stopped}, \pi^+)$ reaction

The first study of the neutron-rich Λ -hypernuclei with the DCX reaction was performed at the KEK 12-GeV proton synchrotron facility by using the $(K^-_{stopped}, \pi^+)$ reaction [32]. There are a few processes contributing to the $(K^-_{stopped}, \pi^+)$ spectra. One is a quasi-free Σ^- production of

$$K^- + p \rightarrow \pi^+ + \Sigma^-, \quad (1.1)$$

which produces π^+ 's with their momenta lower than 170 MeV/c. The signal of the $2p \rightarrow \Lambda n$ conversion process is assumed to be produced through a two-step process of

$$K^- + p \rightarrow \Lambda + \pi^0, \pi^0 + p \rightarrow \pi^+ + n. \quad (1.2)$$

In reaction 1.2, π^+ momentum region of interest is around the end point of quasi-free Λ production (π^+ momentum ~ 250 MeV/c) where the binding energy between hyperon and core nucleus is zero. Another source of π^+ 's comes from the decay of $\Sigma^+ \rightarrow \pi^+ n$ produced from a quasi-free production of $K^- p \rightarrow \Sigma^+ \pi^-$. The π^+ momentum range overlaps in the signal region. Figure 1.4 shows the π^+ momentum spectra measured from three kinds of targets, ${}^9\text{Be}$, ${}^{12}\text{C}$ and ${}^{16}\text{O}$. Due to the in-flight decay π^+ background from $\Sigma^+ \rightarrow n\pi^+$, no clear peak was observed, and upper limits of the formation probabilities per stopped K^- were estimated to be 2.3×10^{-4} in ${}^9_\Lambda\text{He}$, 6.1×10^{-5} in ${}^{12}_\Lambda\text{Be}$ and 6.2×10^{-5} in ${}^{16}_\Lambda\text{C}$, respectively.

The Fisica Nucleare a DAΦNE(FINUDA) collaboration also performed a measurement with the ${}^6\text{Li}(K^-_{stopped}, \pi^+)$ reaction in their first data taking [33]. The clear identification of the production of the neutron-rich hypernuclei, however, was not accomplished in the inclusive π^+ spectra. Recently, in the second data taking by improving the statistics, they have succeeded to observe three candidate events of ${}^6_\Lambda\text{H}$ with the simultaneous detection of both the production of $(K^-, \pi^+)_\Lambda^6\text{H}$ and the mesonic decay of ${}^6_\Lambda\text{H} \rightarrow \pi^- + {}^6\text{He}$ [34]. Figure 1.5 shows the momentum correlation between the produced π^+ and decay π^- from ${}^6_\Lambda\text{H}$ after a kinematical cut. The left figure shows tight kinematical cut and right one shows the loose cut. They reported the number of events (3 event) in the red box does not change for both figures. On the other hand, number of events in

1.2. EXPERIMENTAL APPROACHES FOR THE NEUTRON-RICH Λ -HYPERNUCLEI

the blue box are decreased in the tight cut. Therefore, they interpreted the 3 events are not background but candidates of ${}^6_{\Lambda}\text{H}$ hypernucleus. The production rate was estimated to be $(2.9 \pm 2.0) \times 10^{-6}/K_{stop}^-$. Furthermore, they reported a binding energy for ${}^6_{\Lambda}\text{H}$ was (4.0 ± 1.1) MeV with respect to ${}^5\text{H}+\Lambda$. However, because of the small number of the candidate events, the FINUDA observation should be confirmed with higher statistics.

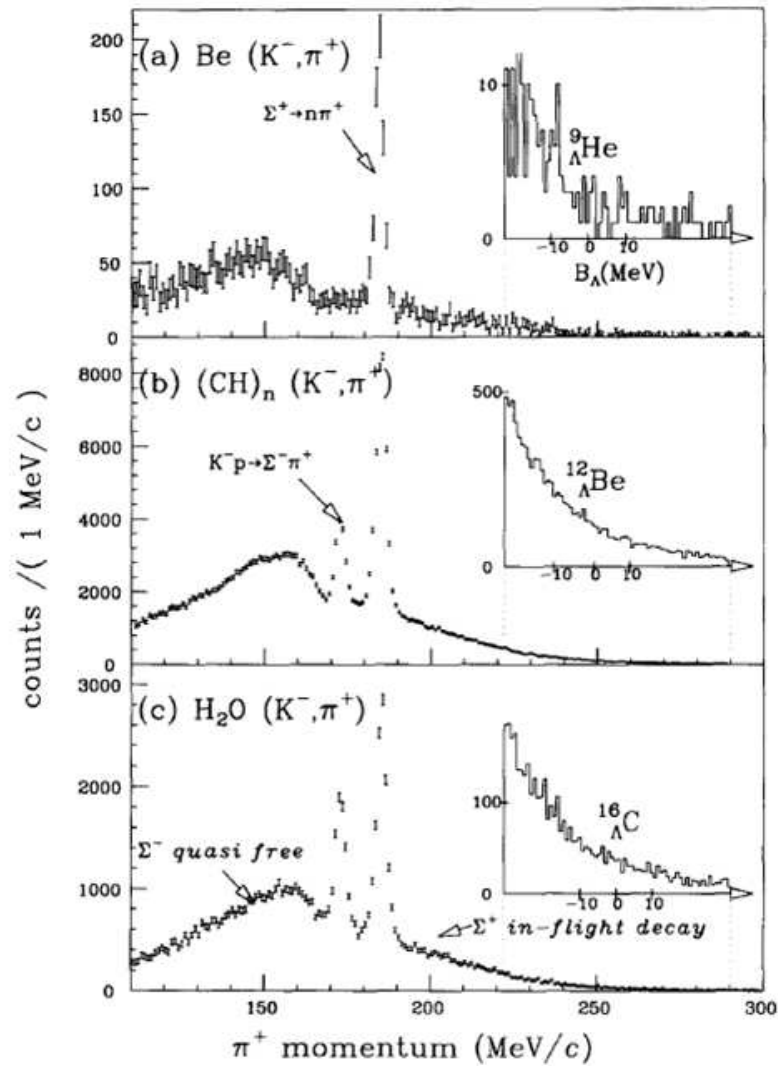


Figure 1.4: π^+ momentum spectra in the $(K_{stopped}^-, \pi^+)$ reaction on (a) ${}^9\text{Be}$, (b) ${}^{12}\text{C}$ and (c) ${}^{16}\text{O}$ targets [32].

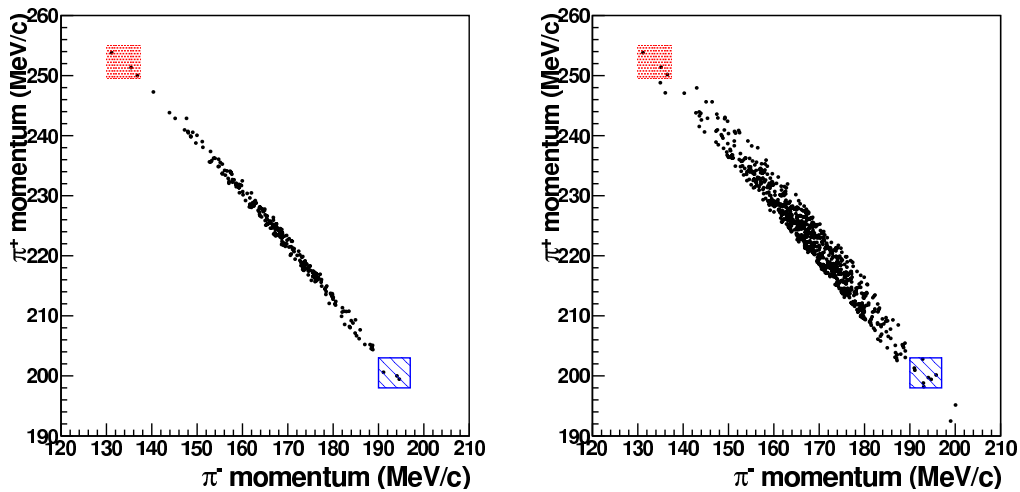


Figure 1.5: π^+ momentum vs π^- momentum for ${}^6\text{Li}$ target events. The shaded (red) rectangle on each side consists of a subset of events with $p_{\pi^+} = 250\text{--}255$ MeV/ c and $p_{\pi^-} = 130\text{--}137$ MeV/ c . The figures were taken from the literature [34].

1.2.2 (π^-, K^+) reaction

Another DCX reaction, the ${}^{10}\text{B}(\pi^-, K^+)$ reaction at 1.05 and 1.2 GeV/ c , was measured in the KEK-E521 experiment [35].

Naive reaction mechanisms of the (π^-, K^+) reaction are the "two-step" reactions as follows;

$$\pi^- + p \rightarrow K^0 + \Lambda, \quad K^0 + p \rightarrow K^+ + n,$$

and

$$\pi^- + p \rightarrow \pi^0 + n, \quad \pi^0 + p \rightarrow K^+ + \Lambda.$$

The two-step reaction mechanisms usually predict larger cross sections at the pion beam momentum around 1.05 GeV/ c because the Λ production reactions in the two-step process have a local maximum at the beam momentum. However, they observed the beam momentum dependence different from this expectation.

There could be another reaction mechanism of a one-step reaction mechanism as follows,

$$\pi^- + p \rightarrow K^+ + \Sigma^-, \quad \Sigma^- p \rightarrow \Lambda n.$$

The second step in the process is the conversion from $\Sigma^- p$ to Λn through the ΛN - ΣN mixing. The one-step mechanism predicts larger cross section at higher beam momenta because the pion beam momentum for the virtual Σ^- production favors higher momenta.

KEK-E521 experiment was performed with SKS spectrometer system [36] in K6 beam line at KEK Proton Synchrotron Facility. At first, they set the beam pion momentum at 1.05 GeV/ c where the cross section has the maximum if the two-step process is dominant. However, the events in the bound region was only 7 counts, and they obtained the cross section of 5.8 ± 2.2 nb/sr, which is much smaller than a theoretical estimation for the ground state doublet based on the two-step mechanism.

Thus, the beam momentum was raised to 1.2 GeV/ c , and the number of measured events was increased to 47 events. The production cross section was 11.3 ± 1.9 nb/sr.

Figure 1.6 shows the missing-mass spectrum of $^{10}\text{B}(\pi^-, K^+)$ reaction. Since there was no physical background in the (π^-, K^+) reaction in the bound region, the $^{10}_{\Lambda}\text{Li}$ production events were clearly observed. From this result, the production cross section of DCX is found to be roughly 10^{-3} of that of the non charge-exchange (π^+, K^+) reaction. Based

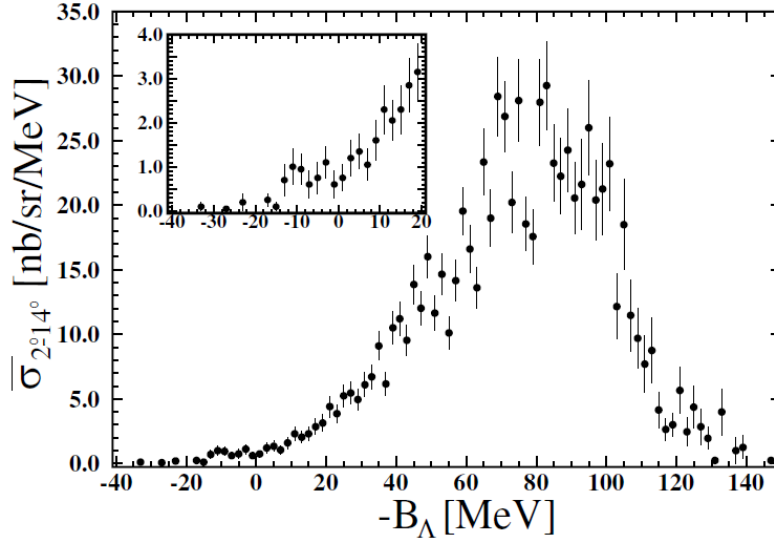


Figure 1.6: The missing-mass spectrum of the $^{10}\text{B}(\pi^-, K^+)$ reaction measured in [35]. The inset shows a closeup of the Λ bound region.

on the KEK-E521 experiment, a theoretical calculation of the double charge-exchange reaction was performed by Harada *et al.* [37]. Figure 1.7 shows the calculated inclusive excitation spectrum with the one-step mechanism for the $^{10}\text{B}(\pi^-, K^+)$ reaction at $p_\pi = 1.20$ GeV/ c . In the top figure, intermediate Σ nucleus potential, W_Σ , is scanned when the mixing potential of $V_{\Lambda\Sigma}$ is fixed at 11 MeV. In the bottom figure, $V_{\Lambda\Sigma}$ is scanned when W_Σ is 20 MeV. As a result, when the magnitude of probability of $\Lambda - \Sigma$ mixing is 0.57%, the theoretical spectrum is in good agreement with the experimental data.

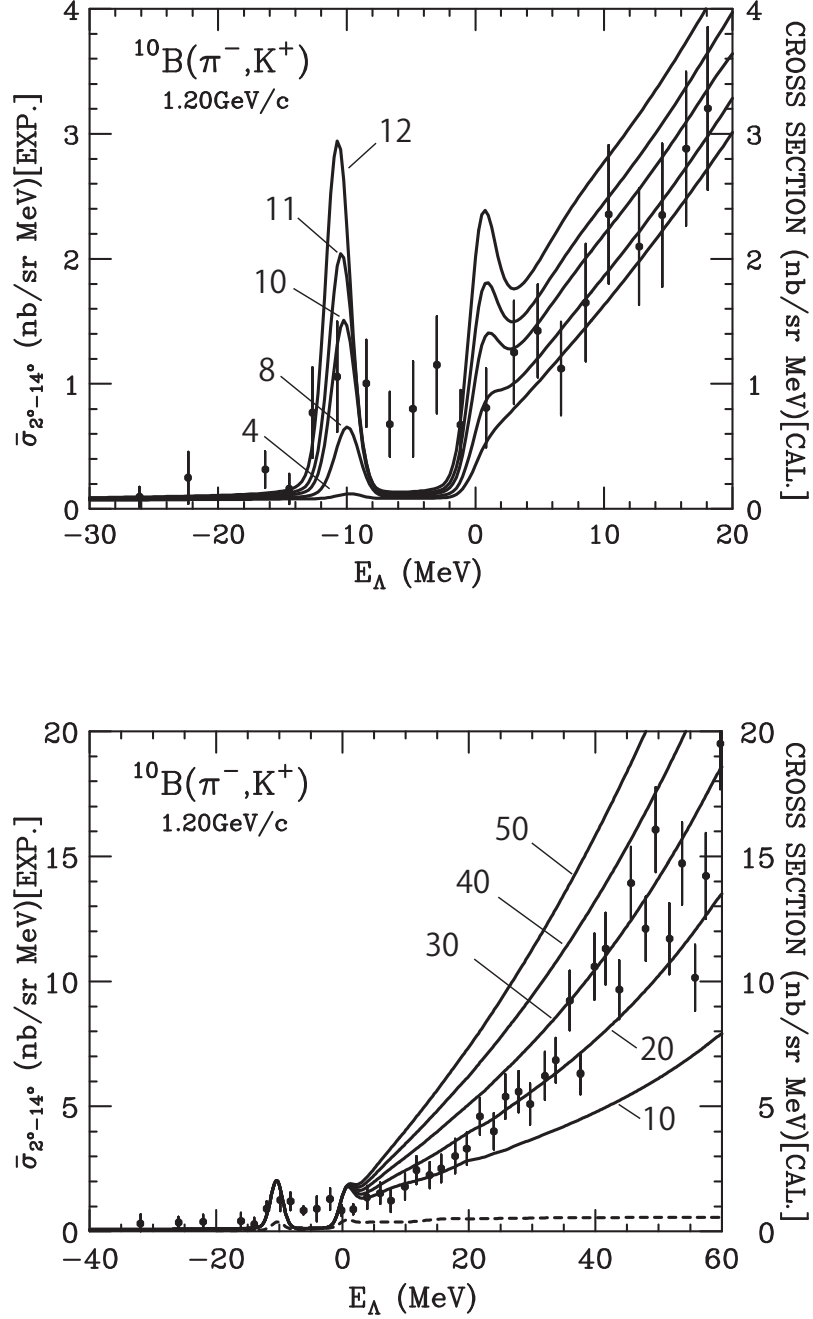


Figure 1.7: Calculated inclusive excitation spectra with the one-step mechanism for the $^{10}\text{B}(\pi^-, K^+)$ reaction at $p_\pi = 1.20 \text{ GeV}/c$, together with the experimental data [35]. (Top) The solid curves denote the K^+ spectra by $V_{\Sigma\Lambda} = 4, 8, 10, 11, 12$ MeV when $-W_\Sigma = 20$ MeV, with a detector resolution of 2.5 MeV (FWHM). (Bottom) The solid curves denotes $-W_\Sigma = 10, 20, 30, 40, 50$ MeV when $V_{\Sigma\Lambda} = 11$ MeV ($P_\Sigma = 0.57\%$). The dashed curve denotes the inclusive Λ spectrum by the two-step mechanism.

1.3 J-PARC E10

The present experiment was proposed aiming at a precise spectroscopic investigation of light neutron-rich Λ -hypernuclei, ${}^6_{\Lambda}\text{H}$ via the (π^-, K^+) reaction by using the SKS spectrometer.

The same π^- momentum of 1.2 GeV/ c was selected as in the KEK-E521 experiment. The FINUDA group reported the binding energy of ${}^6_{\Lambda}\text{H}$ based on three candidate events. We would like to much improve the precision of the binding energy and establish the existence in high statistics. A high-intensity π^- beam at J-PARC and a large acceptance of the SKS spectrometer have good merits for this purpose. We also introduced high-rate tracking detectors such as scintillating fiber detectors and silicon strip detectors for the E10 experiment. By observing more than 100 events, not only the precise binding energy but also the production cross section can be obtained in a good statistical accuracy. It would be important in order to discuss the $\Lambda\text{N}-\Sigma\text{N}$ mixing effect, quantitatively. The structure of the ${}^6_{\Lambda}\text{H}$ will be revealed for the first time.

1.4 Theoretical approach for the ${}^6_{\Lambda}\text{H}$ hypernucleus

Theoretical calculations on ${}^6_{\Lambda}\text{H}$ have been performed with various models and interactions. We have summarized the binding energy of the ${}^6_{\Lambda}\text{H}$ ground state of theoretical calculations compared with FINUDA data in Fig. 1.8. The ground state of ${}^5\text{H}$ is the resonance of 1.7 MeV with respect to ${}^3\text{H}+2n$, and ${}^4_{\Lambda}\text{H}$ hypernucleus is bound by 2.0 MeV with respect to ${}^3\text{H}+\Lambda$.

A highly neutron-rich Λ -hypernucleus ${}^6_{\Lambda}\text{H}$ was first discussed by Dalitz and Levi-Setti [38]. They predicted the Λ binding energy of the ground state to be 4.2 MeV by using central part of ΛN interaction. Akaishi *et al* suggested a considerably large binding energy of 5.8 MeV for the 0^+ ground state of ${}^6_{\Lambda}\text{H}$ due to a rather large contribution of 1.4 MeV from the coherent $\Lambda\text{N}-\Sigma\text{N}$ coupling [39]. The coherent $\Lambda\text{N}-\Sigma\text{N}$ coupling was considered to solve over binding problem of s -shell hypernuclei such as ${}^3_{\Lambda}\text{H}$, ${}^4_{\Lambda}\text{H}$, ${}^4_{\Lambda}\text{He}$ and ${}^5_{\Lambda}\text{He}$ [29]. Gal and Millener estimated it by a phenomenological shell-model calculation [40], and obtained the binding energy of $3.83 \pm 0.08 \pm 0.22$ MeV. Hiyama *et al.* performed the four-body cluster-model calculation with $t(\text{triton}) + n + n + \Lambda$, and obtained the binding energy of 2.57 MeV [41]. This calculation is the only one that considers dynamically the ${}^5\text{H}$ core as a three-body ${}^3\text{H}-n-n$ resonance, and it disregards the $\Lambda - \Sigma$ coupling effect. These theoretically calculated binding energies were distributed as shown in Fig. 1.8 from bound to unbound regions with respect to the ${}^4_{\Lambda}\text{H}+2n$ decay threshold, which corresponded to the Λ binding energy of 3.7 MeV. They were quite sensitive to the ΛN interaction and the properties of the core nucleus ${}^5\text{H}$.

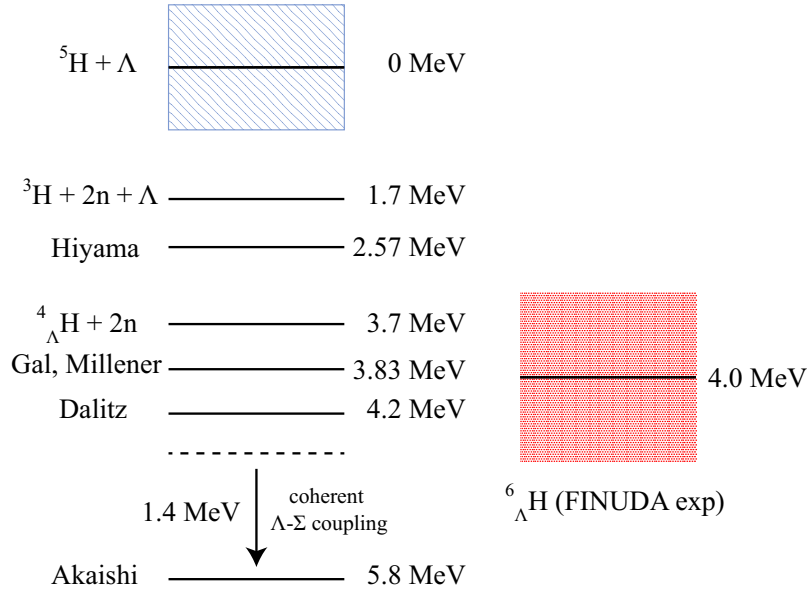


Figure 1.8: Theoretical calculation of ${}^6_{\Lambda}\text{H}$ binding energy.

${}^5\text{H}$, the core nucleus of ${}^6_{\Lambda}\text{H}$, was first produced at Joint Institute for Nuclear Research (JINR). They measured two protons emitted from the decay of ${}^2\text{He}$ with the reaction of $p({}^6\text{He}, {}^2\text{He})$ [42], and found the ${}^5\text{H}$ is the resonance state of 1.7 ± 0.3 MeV with respect to $t + n + n$ threshold with a width of 1.9 ± 0.4 MeV. Figure 1.9 shows the missing-mass spectrum of the $p({}^6\text{He}, {}^2\text{He})$ reaction. Extensive studies have been made at Helmholtzzentrum für Schwerionenforschung GmbH (GSI) and Los Alamos Meson Physics Facility (LAMPF) [43, 44] by using ${}^9\text{Be}(\pi^-, pt)$ and ${}^9\text{Be}(\pi^-, dd)$ reactions as shown in Fig 1.10 and Fig 1.11. No clear peak structure was observed in both experiments not only bound states but also resonance states. Therefore, the existence of the ${}^5\text{H}$ state is not established yet. A precise study will be conducted at RCNP in the near future.

The present thesis consists of six chapters and one appendix. Chapter 2 describes the experimental apparatus. As mention above, to accumulate large number of event, it is necessary to use high intensity beam. In preparing of the present experiment, we have developed some new detectors and electronics for high rate operation. Chapter 3 describes the data analysis. After data taking, I analyzed all the data, in which special cares were taken to reduce the background event around the bound region. Since the production cross section of (π^-, K^+) reaction is a few nb/sr level, it is important to reduce the background event as much as possible. Also, in that chapter, elaborate calibration procedures of the momentum is described. Chapter 4 describes the experimental results, Chapter 5 the physics discussions about the results, and Chapter 6 a conclusion.

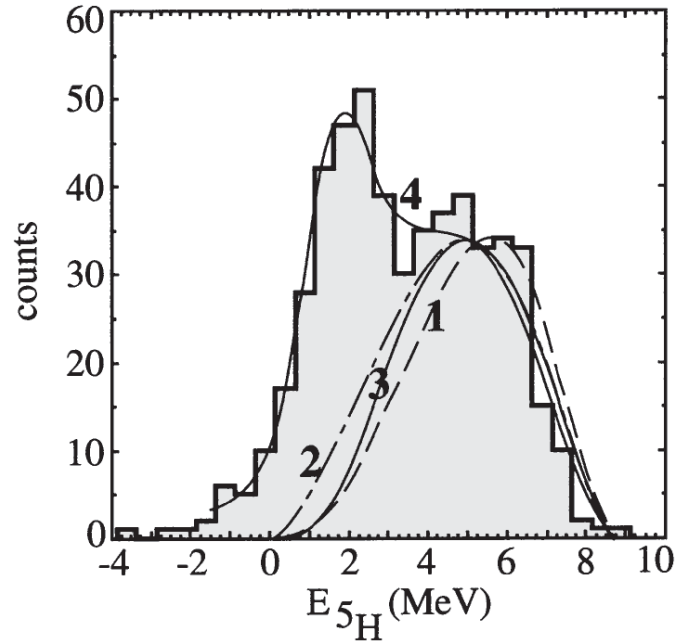


Figure 1.9: ${}^5\text{H}$ spectrum measured in coincidence with triton from the decay of the residual ${}^5\text{H}$ system [42].

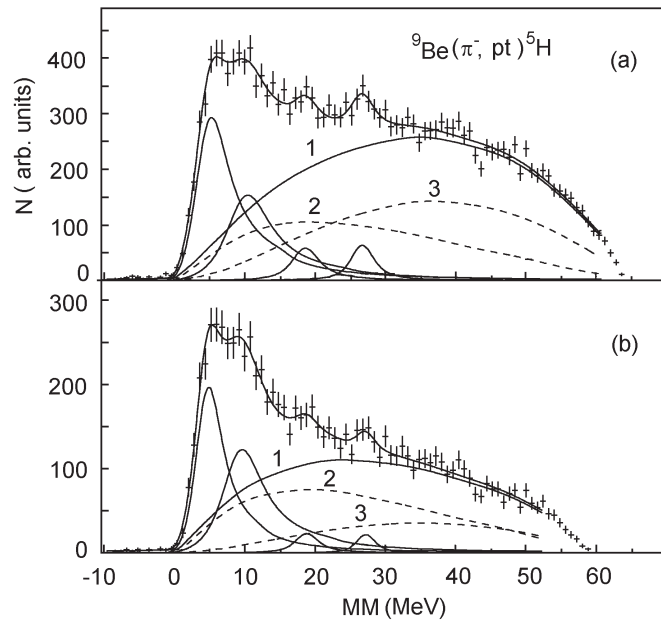


Figure 1.10: Missing-mass spectra for the ${}^9\text{Be}(\pi^-, pt)\text{X}$ reaction without (a) and with (b) restriction on the momentum of residual nuclei. The solid lines are the fit and Breit-Wigner distributions. Curve 1 is the sum of phase space distributions for all open channels, curve 2 is the phase space distribution for the break up of ${}^9\text{Be}$ into $p+t+{}^4\text{H}+n$, curve 3: $p+t+t+n+n$; curve 4: $p+t+d+n+n+n$.

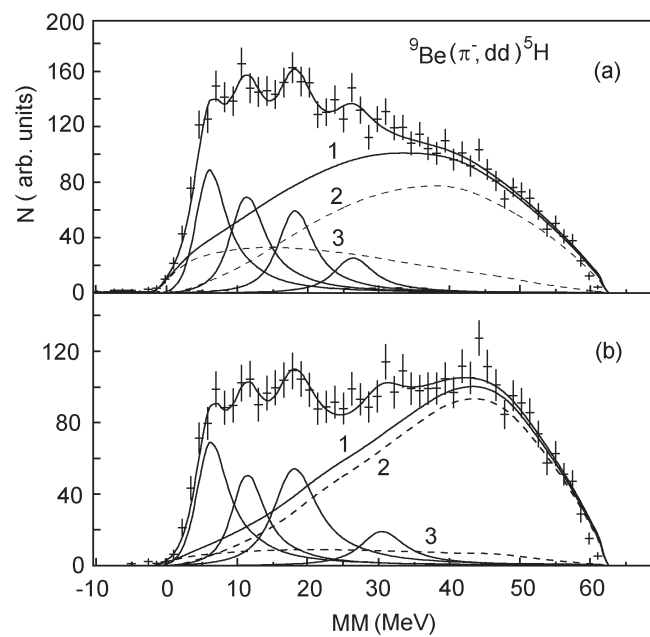


Figure 1.11: Missing-mass spectra for the ${}^9\text{Be}(\pi^-, dd)X$ reaction without (a) and with (b) restriction on the momentum of residual nuclei. The solid lines are the fit and Breit-Wigner distributions. Curve 1 is the sum of phase space distributions for all open channels, curve 2 is the phase space distribution for the breakup of ${}^9\text{Be}$ into $d+d+{}^4\text{H}+n$; curve 3: $d+d+t+n+n$

Chapter 2

Experiment

2.1 Outline

The present experiment was carried out from December 2012 to January 2013 as J-PARC E10 in the K1.8 beam line of J-PARC Hadron Experimental Facility. The purpose of the experiment is to produce the neutron-rich Λ -hypernucleus ${}^6_{\Lambda}\text{H}$ by the (π^-, K^+) reaction with good energy resolution and high statistics, and to study its structure and establish the existence of ${}^6_{\Lambda}\text{H}$. To obtain the high energy resolution, we used the K1.8 beam line spectrometer and superconducting kaon spectrometer (SKS). In Chap.2.2, The accelerator of J-PARC and Hadron Experimental Facility are described. In Chap.2.3, The detail of K1.8 beam line is described. The details of the K1.8 beam line and the SKS spectrometers are described in Chap. 2.4 and Chap. 2.5, respectively.

2.2 J-PARC and Hadron experimental facility

J-PARC (Japan Proton Accelerator Research Complex) (Fig. 2.1) [45] is a high intensity proton accelerator facility which aims to pursue frontier in nuclear physics, particle physics, materials and life science and nuclear technology, using a new proton accelerator complex with the highest beam power in the world.

H^- is produced at an ion source and accelerated by Linac upto 400 MeV (50 mA) [46]. The accelerated H^- is converted to a proton (H^+) and injected to the 3 GeV Rapid-Cycling Synchrotron (RCS) which accelerates protons to 3 GeV (333 μA) [47]. Finally, part of protons are injected to Main Ring (MR) and accelerated up to 50 GeV (15 μA) [48]. The 50-GeV proton beams are provided to the hadron facility and the secondary hadron beams are produced for experiments. In 2010, the beam energy after Linac was 189 MeV. In the phase-1 of the J-PARC construction, the beam energy is 30 GeV and the goal of the beam intensity is 9 μA (270 kW). The operation of the J-PARC accelerator was started in 2009.

The primary proton beam from the main ring was extracted for a duration of 2.0 seconds in every 6.0 seconds, which is synchronized to the J-PARC 30-GeV PS operation cycle. This duration of the beam extraction is called a spill.

The J-PARC E10 experiment was performed at the K1.8 beam line in the hadron experimental facility (Fig. 2.2). The facility consists of a primary beam line, several

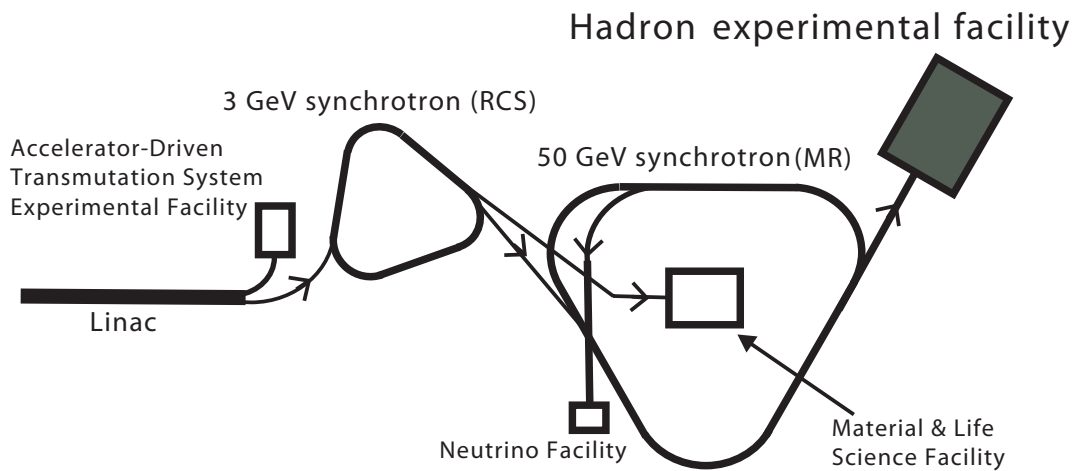


Figure 2.1: A schematic view of J-PARC Facility.

secondary beam lines where individual experiments are set up. The proton beam is transported from the Main Ring to the hadron facility and bombarded to the production target, T1. In the present experiment, the production target was a gold rod ($6 \times 6 \times 60$ mm). The hadronic beams (kaons, pions, and so on) produced at T1 are delivered to an experimental area through secondary beam lines. Thus, the secondary beams are available for several lines (K1.8BR, K1.1BR and KL) simultaneously.

Hadron Experimental Facility

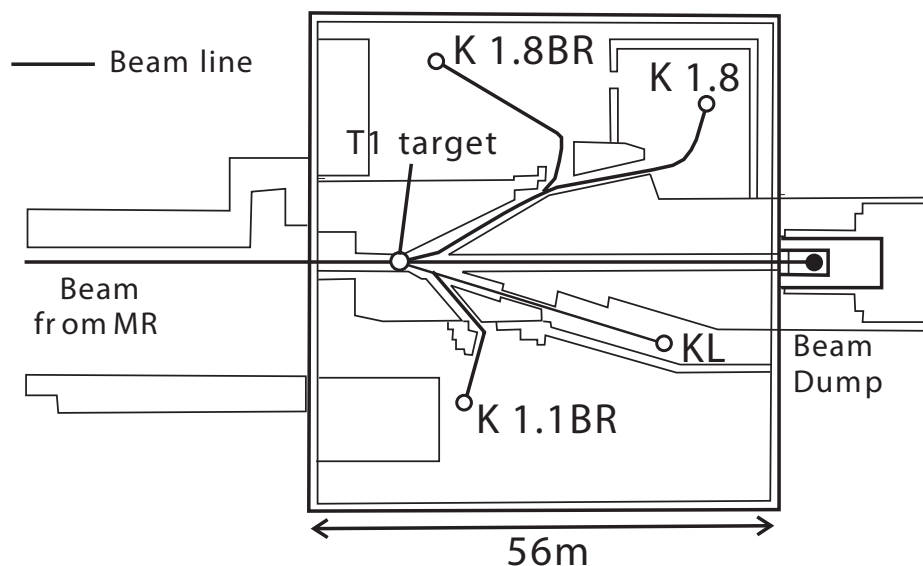


Figure 2.2: The schematic view of hadron experimental facility as of 2013.

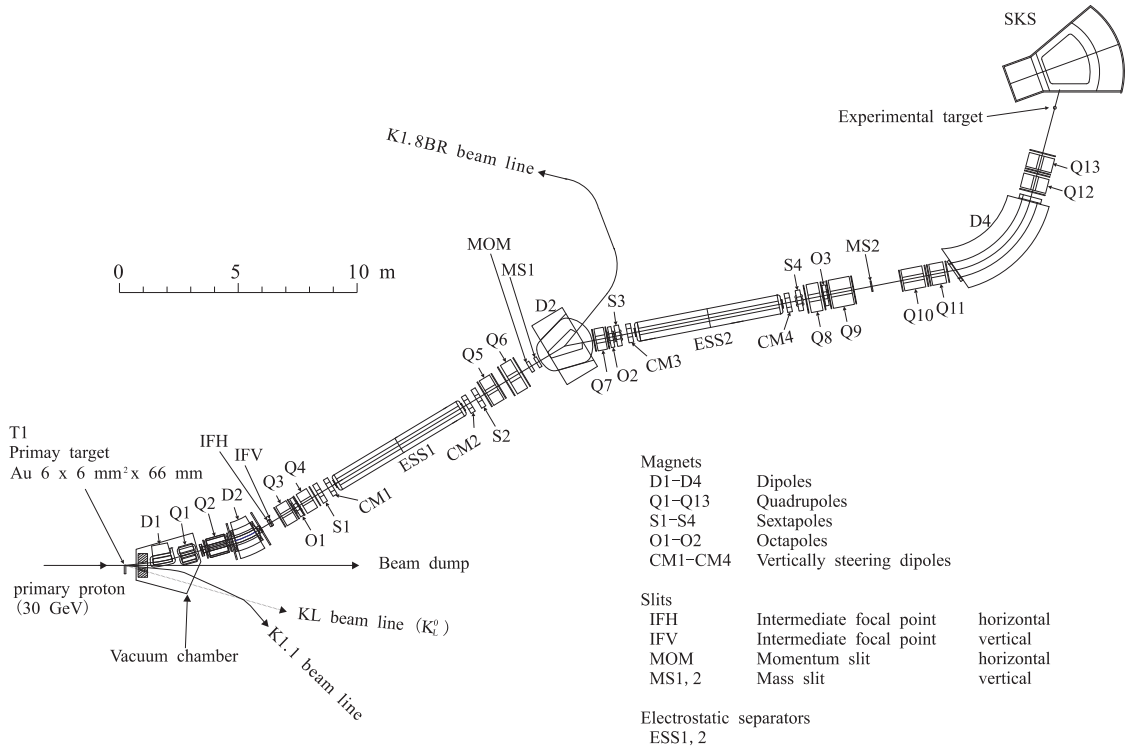


Figure 2.3: Schematic view of K1.8 beam line

2.3 K1.8 beam line

The K1.8 beam line is a general-purpose mass-separated beam line that can supply various secondary hadron beams up to $2.0 \text{ GeV}/c$ [49]. The most important design principle is to supply both high-intensity and high-purity kaon beams for an investigation of the $S = -2$ hypernuclei. The K1.8 beam line is designed to archive the K^-/π^- ratio of larger than 1 providing the kaon beam intensity of 10 MHz on an experimental target.

Figure 2.3 shows a schematic view of the K1.8 beam line. The beam line consists of four dipole magnets(D1–D4), thirteen quadruple magnets(Q1–Q13), four sextuple magnets(S1–S4), two electrostatic separators(DC separator) with four correction magnets(CM1–CM4) and four slits(IF, MOM, MS1, MS2). The total length of the beam line is about 46 m.

The secondary pions were produced by the primary proton beam in a production target located at the most upstream of the K1.8 beam line as shown in Fig.2.2. In the present experiment, a gold rod of $6 \text{ mm} \times 66 \text{ mm}$ was used as a production target. The primary beam intensity on the production target was typically $1.4 \times 10^{13}/\text{spill}$ (10kW operation) in December 2012 and $1.8 \times 10^{13}/\text{spill}$ (15kW operation) in January 2013, respectively. The pion beam was selected by the DC separators. The maximum gradient of the electro static field is $750 \text{ kV}/\text{cm}$ between the 10 cm gap. In the present experiment, both the DC separators were set to $150 \text{ kV}/\text{cm}$.

After the momentum and mass selections, the pion beam was achromatically focused on the experimental target. In the present experiment, the central beam momentum was set at $1.2 \text{ GeV}/c$ for the ${}^6\text{Li}(\pi^-, K^+)$ reaction. A typical momentum bite was about

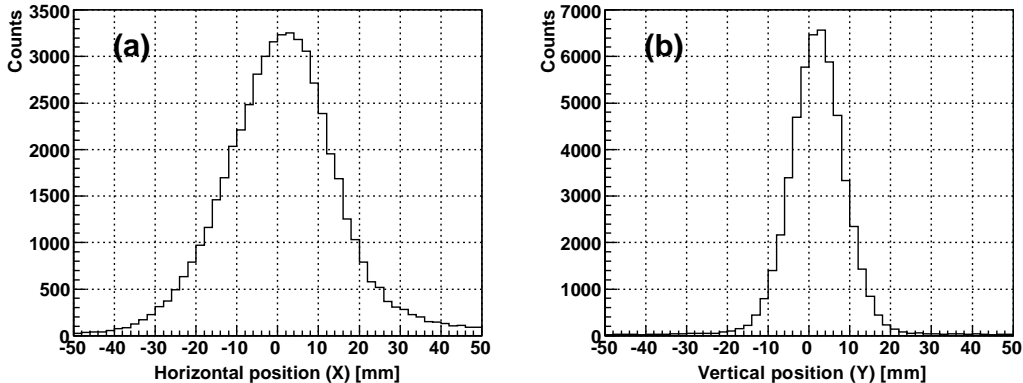


Figure 2.4: Typical beam profile at the experimental target in the E10 experiment measured by tracking chambers at the downstream of the K1.8 beam line spectrometer. The horizontal (a) and vertical (b) positions are shown.

2% (FWHM) determined by the setting of the momentum slit (MOM). The measured beam size at the experimental target position by tracking chambers at the downstream of the K1.8 beam line spectrometer was typically $56^W \times 28^H$ (mm²) in FWTM, as shown in Figure 2.4.

2.4 K1.8 beam line spectrometer

The end-part of the K1.8 beam line is used as a beam spectrometer [50] to analyze momentum and trajectory of each beam particle. Figure 2.5 shows the schematic view of the K1.8 beam line spectrometer. The beam spectrometer consists of a gas Čerenkov counter (GC), a scintillating fiber tracker (BFT), QQDQQ magnets, two drift chambers (BC3 and BC4) and a timing plastic scintillation hodoscope (BH2).

Beam trajectories are measured by BFT and BC3-BC4 for momentum analysis and reaction vertex reconstruction. For the momentum reconstruction, a third-order transfer matrix was used through the QQDQQ system. In order to minimize the multiple scattering effect on the momentum resolution, the $\langle x|\theta \rangle$ term of the transport matrix was tuned to be zero. The design momentum resolution is 3.3×10^{-4} (FWHM) with the position accuracy of 0.2 mm (rms). The magnetic field of the dipole magnet (D4) was monitored during the experiment with a high-precision Hall Probe [Digital Tesla meter 151 (DTM-151)] with the accuracy of 1.7×10^{-6} [51]. The observed fluctuation was less than 0.05% during the data taking period. Design specifications of the K1.8 beam line spectrometer are listed in Table 2.1.

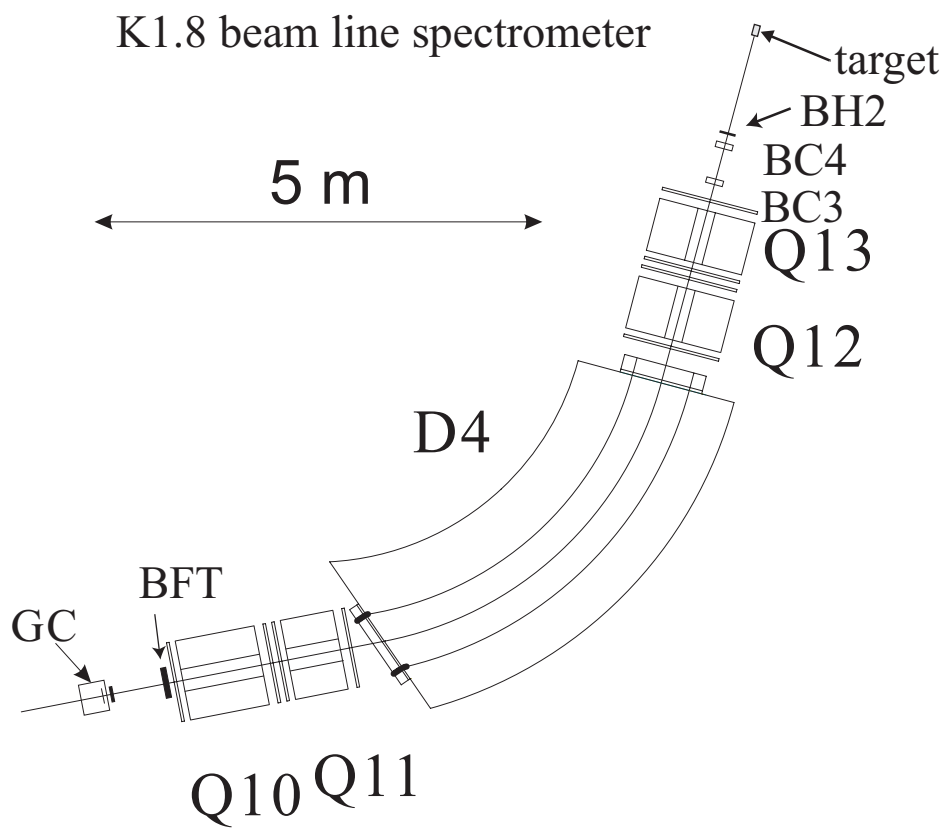


Figure 2.5: Schematic view of K1.8 beam spectrometer.

Table 2.1: Design specifications of the K1.8 beam line spectrometer

Momentum resolution	3.3×10^{-4} (FWHM)
Maximum momentum	2.0 GeV/ c
Bending angle	64°
Flight path (BH1–BH2)	10.4 m
Effective length (D4)	4 m

2.4.1 Particle ID counters

Particle ID counters of K1.8 beam line spectrometer were comprised of GC and BH2. Specifications of the particle ID counters are listed in Table 2.2. GC and BH2 are installed for identifying incoming pion beam.

Table 2.2: Specifications of the particle identification counters in the beam line spectrometer

Name	Sensitive area W×H×T (mm)	Spec.	PMT (Hamamatsu)
GC	340×80(mirror), 290 ^L	iso-C ₄ H ₁₀ , n~1.002 (1.5 atm)	R1250-03 (UV glass)
BH2	118×60×5	8 segments, 3-stage booster	E10679

GC

The Čerenkov counter, GC, is installed at the most upstream of the K1.8 beam line spectrometer in order to reject electrons. Figure 2.6 shows a schematic view of GC. The pressured isobutane-gas (0.15 MPa) was used. In addition, to increase the detection efficiency, the 5" PMT with a UV transparent window was equipped. A reflection mirror was made of a borosilicate glass coated with aluminum. In order to resist against oxidation, the surface of the aluminium was coated with the manganese fluoride (MgF₂) which is transmissive in the ultraviolet-light region. The configuration of the mirror and the PMT was optimized to focus the Čerenkov radiation on to the photo-cathode of the PMT. The number of photo-electrons detected by GC was about 5 for electrons with the momentum of larger than 0.5 GeV/*c*.

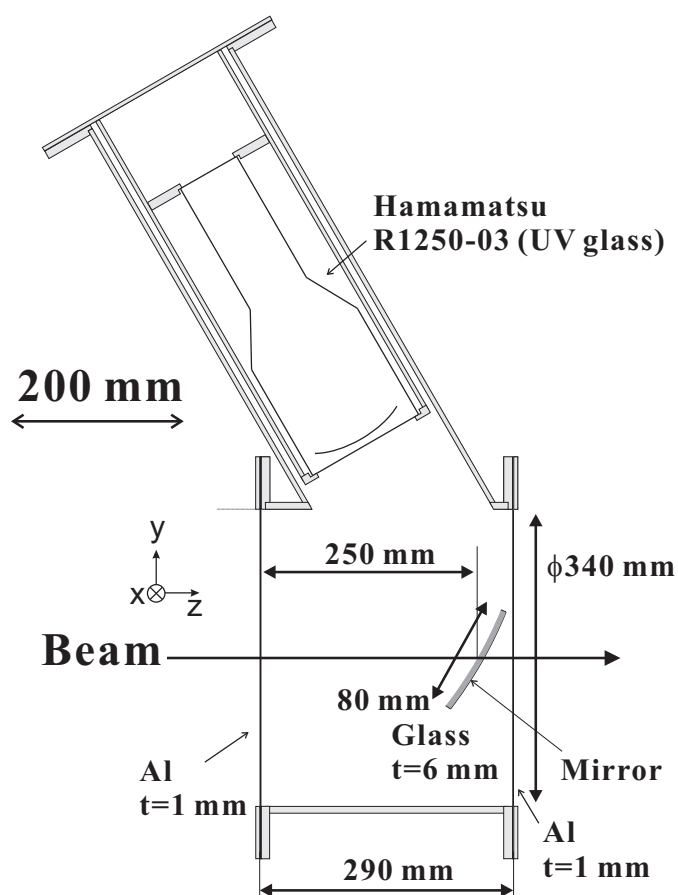


Figure 2.6: The schematic view of GC.

BH2

BH2 is a segmented plastic scintillation counter located 120 cm upstream of the experimental target to define the time zero for all the timing measurements. Figure 2.7 shows a schematic view of BH2. It was segmented into 8 vertical pieces of 5-mm thick plastic scintillators. The horizontal size of each segment is adjusted for the single counting rate of each segment to be uniform considering the beam profile. $3''/8$ phototubes with a three-stage booster were connected on both ends of each segment.

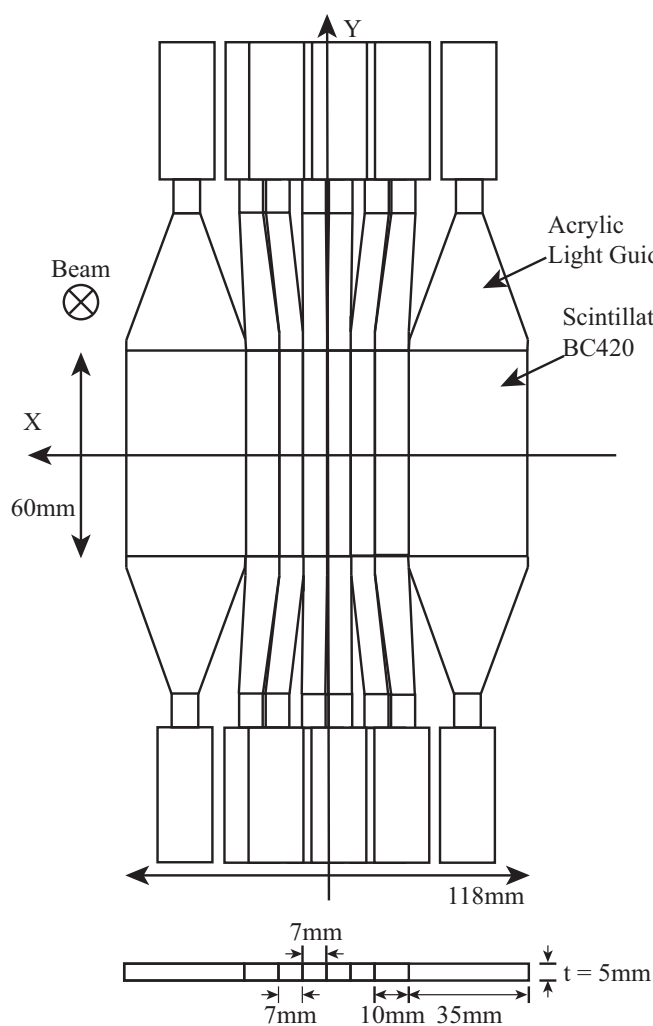


Figure 2.7: A schematic view of BH2.

2.4.2 Tracking devices

Specifications of the tracking devices in the beam line spectrometer are summarized in Table 2.3.

Table 2.3: Specifications of the tracking devices in the beam line spectrometer.

Name	Effective area W×H (mm)	pitch (mm)	Wires	Angle (x, u, v) (°)	Typical resolution (μm in r.m.s)
BFT	160×80	1.0	xx'	0	200
BC3	192×150	1.5	$xx'uu'vv'$	0, +15, -15	200
BC4	192×150	1.5	$vv'uu'xx'$	0, +15, -15	200
SSD	61×61	0.08	xy	0, +90	20

BFT

At the entrance of the K1.8 beam line spectrometer, particle trackers should be operated under a very high counting rate at 10–20 MHz. To improve the high-rate tolerance and measure the time information precisely, a scintillating fiber tracker (BFT) was installed just upstream of Q10 magnet. The high-rate tolerance was checked by using proton beam at 400 MeV in RCNP [52]. The efficiency was kept more than 95% at 1 MHz/fiber. BFT is a scintillating fiber tracker with a xx' structure and is made of scintillating fibers with 1 mm diameter. The light signals from the scintillating fibers are read out by Multi Pixel Photon Counters(MPPCs). The Extended Analogue SiPM ReadOut Chip (EASIROC) system was used [53] as read out electronics. The EASIROC was developed at Linac Accelerator Laboratory (LAL) in France. EASIROC has 32 MPPC inputs and all essential functions to operate many MPPCs such as amplifier, discriminator and bias adjustment for MPPCs. The multi-hit tdc program has developed by rewriting the FPGA in EASIROC chip. The encoded data is transferred through the SiTCP connection.

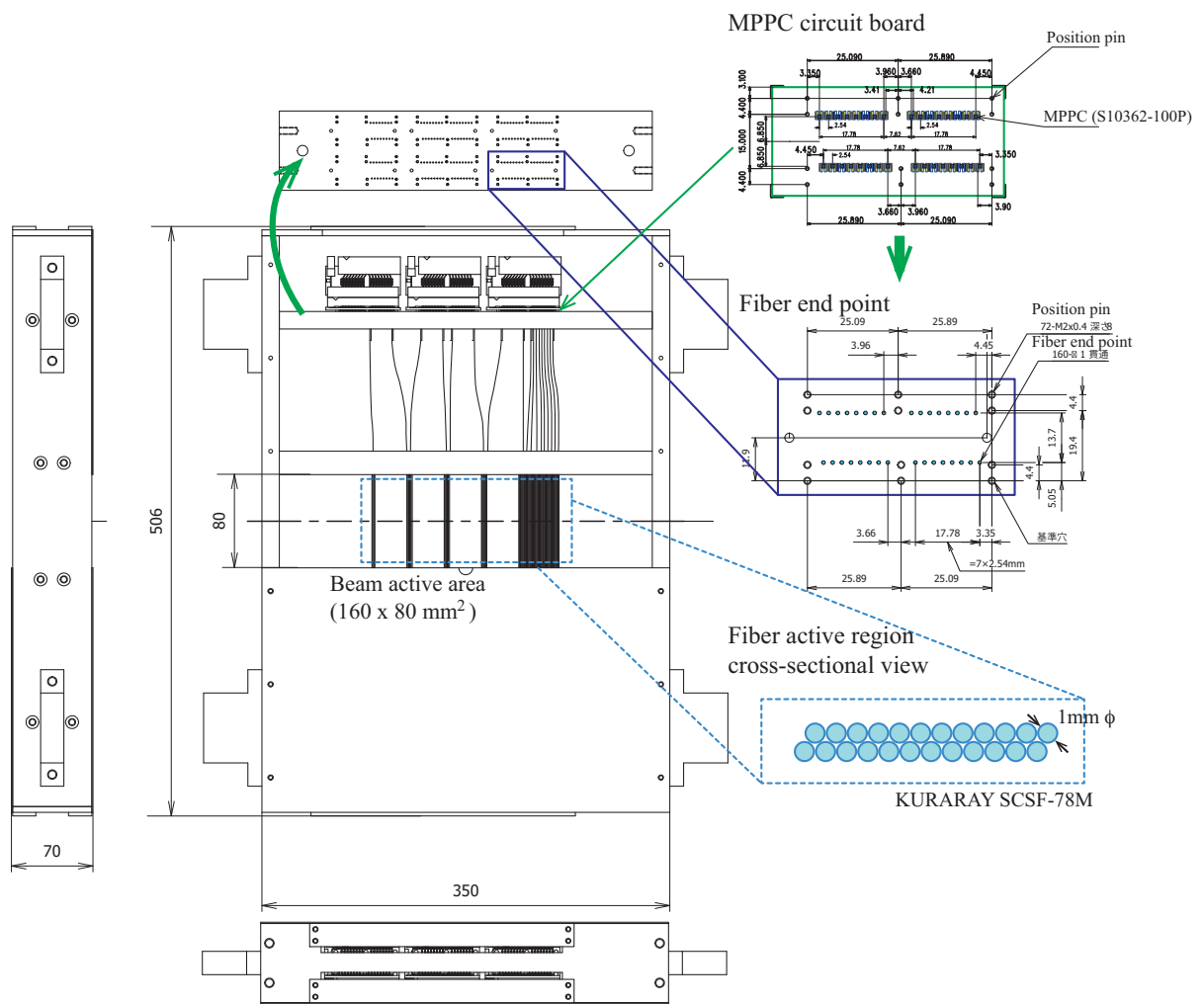


Figure 2.8: The structure of BFT

BC3 and BC4

The drift chambers BC3 and BC4 with a 3 mm wire pitch was located at the exit of the K1.8 beam line spectrometer. Figure 2.9 shows the cell structure of BC3 and BC4. The sense wire was a gold-plated $12.5 \mu\text{m}$ diameter tungsten wire and the field wire was a gold-plated $75 \mu\text{m}$ diameter copper-beryllium wire. The cathode planes are made of $20 \mu\text{m}$ -thick graphite pasted on a $12 \mu\text{m}$ -thick aramid film. The drift chambers have 6 layers (xx', uu', vv'), where u and v wires were tilted by $\pm 15^\circ$ with respect to the x wires. The wire position of each pair plane was shifted by a half of the cell size. The gas mixture was $\text{Ar}(76\%) + \text{C}_4\text{H}_{10}(20\%) + \text{Methylal}(4\%)$. The front-end read-out electronics was made of ASD (Amplifier-Shaper-Discriminator) chips with 16ns integration time developed for ATLAS Thin Gap Chamber. The timing information of the BC3 and BC4 hit was digitized by the COPPER Multi-hit TDC module[54] as described in Chap. 2.6.

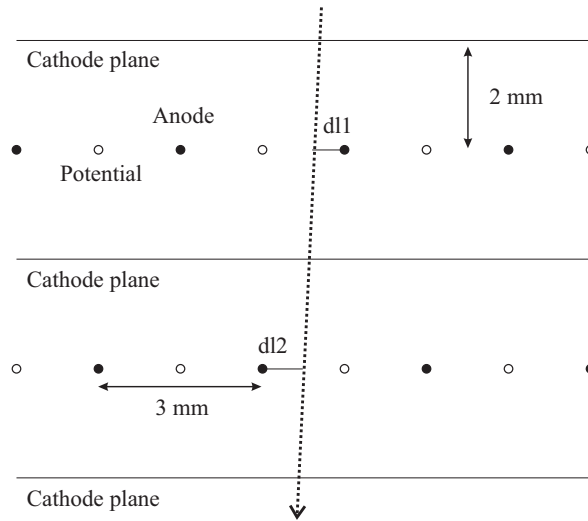


Figure 2.9: The cell structure of BC3-4

Silicon Strip Detector (SSD)

Since there is a 1200 mm distance from BH2 to a target, even if the BC3 and BC4 local tracking is succeeded, the extrapolated target position is broadened due to multiple scattering in the BH2 and air between BH2 to the target. Since we use a high intensity beam, we may have a lot of accidental hits in the tracking detectors with a finite time resolution, which eventually produce many fake tracks. Also, it is important to have a good vertex resolution to suppress background coming from the materials other than the target. Therefore, silicon strip detectors (SSD) with xy structure and $80\ \mu\text{m}$ strip pitch are installed at the upstream of the target. Figure 2.10 shows a picture of SSD. The sensor is developed by ATLAS group in LHC. The effective area is $61^W \times 61^H$ (mm^2), and thickness is $300\ \mu\text{m}$. A readout chip, APV25-s1 chip, was developed by CMS group in LHC. The signal is multiplexed after amplified and shaped, and is transferred serially each 25 nsec (40 MHz clock sampling) to APVDAQ-VME system. APVDAQ system digitizes the serialized analog data each 25 nsec, and then suppress pedestals within 3σ of the pedestal resolution. To reduce the dead time of the data acquisition, a double buffer mode is applied, which enables us to read and send the data simultaneously. The rate tolerance was checked at LNS and RCNP test experiment [52]. As shown in figure 2.11, the efficiency of SSD was kept more than 95% at 10^5 Hz/strip which corresponds to 2×10^7 Hz beam at J-PARC.

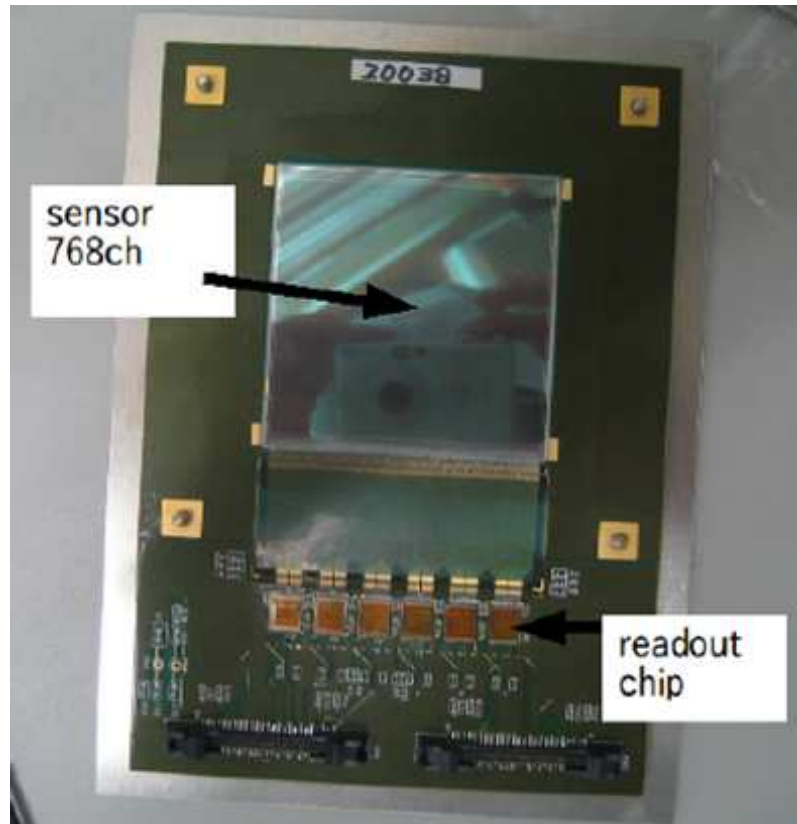


Figure 2.10: The picture of SSD.

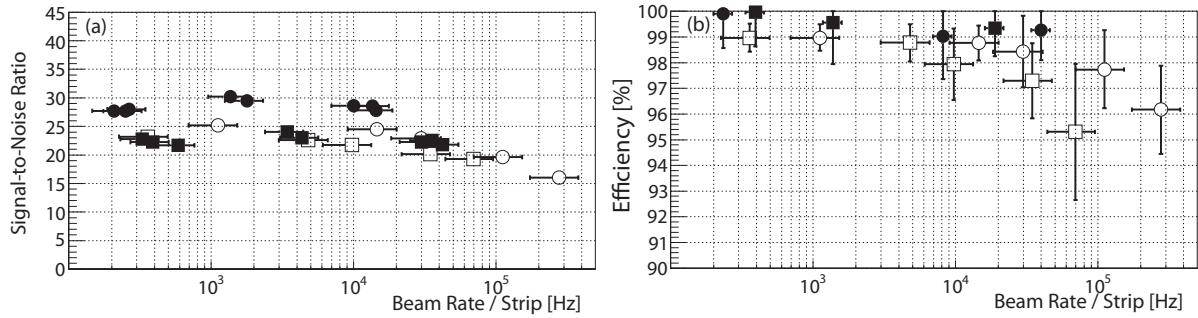


Figure 2.11: Beam rate dependence of the SSD performances. The horizontal axis represents the incident beam intensity in units of beam rate per strip. The results of the LNS data are represented by open markers, and the results of the RCNP data are represented by filled markers, where the box and the circle indicate respective SSDs. (a) Signal-to-noise ratio versus beam rate. (b) Hit efficiency versus beam rate.

2.5 Scattered-particle spectrometer (SKS)

The superconducting kaon spectrometer (SKS) was designed and constructed for the study of Λ -hypernuclei with the (π^+, K^+) reaction [36]. Design parameters of the SKS are summarized in Table 2.4. The characteristic feature of the SKS is to have a good momentum resolution of 0.1% together with a large acceptance of 100 msr at around 0.9 GeV/c. In addition, it keeps the flight path as short as 5.5 m for the central trajectory in order to minimize kaon decay-in-flight, and has a powerful kaon identification ability. The SKS magnetic field is excited at 2.16 T (300A). The SKS enables us to perform hypernuclear spectroscopy with a good energy resolution and in high statistics.

Table 2.4: Design specifications of the new SKS spectrometer at 2.16 T mode.

Maximum magnetic field	2.5 T
Stored energy	6.3 MJ
Pole gap	49.75 cm
Conductor	NbTi/Cu
Ampere Turn	2.1 MA·T
Maximum current	400 A
Total weight	280 t
Momentum resolution	0.1% FWHM at 0.9 GeV/c
Maximum momentum	1.1 GeV/c
Momentum range	0.70–1.10 GeV/c
Bending angle	85° for central trajectory
Solid angle	100 msr
Flight path	~5.5 m for central trajectory

Figure 2.12 shows schematic view of the SKS. The SKS consists of a scintillating fiber tracker (SFT), three drift chambers (SDC2–4) for the momentum reconstruction, a superconducting magnet, a timing plastic scintillation hodoscope (TOF) and two threshold-type Čerenkov counters (LAC and LC) for particle identification. The particle momentum was reconstructed with the Runge-Kutta method [61] from the hit information of fiber tracker, drift chambers and a calculated field map. In order to reduce multiple scattering effects on the momentum resolution, helium bags were installed in the spaces along the particle trajectory (the SKS pole gap and the space between SDC3 and the SKS magnet). The magnetic field was monitored with an NMR probe during the experiment to correct for the fluctuation of the field in the offline analysis. The accuracy of the NMR probe is 1.0×10^{-6} [55].

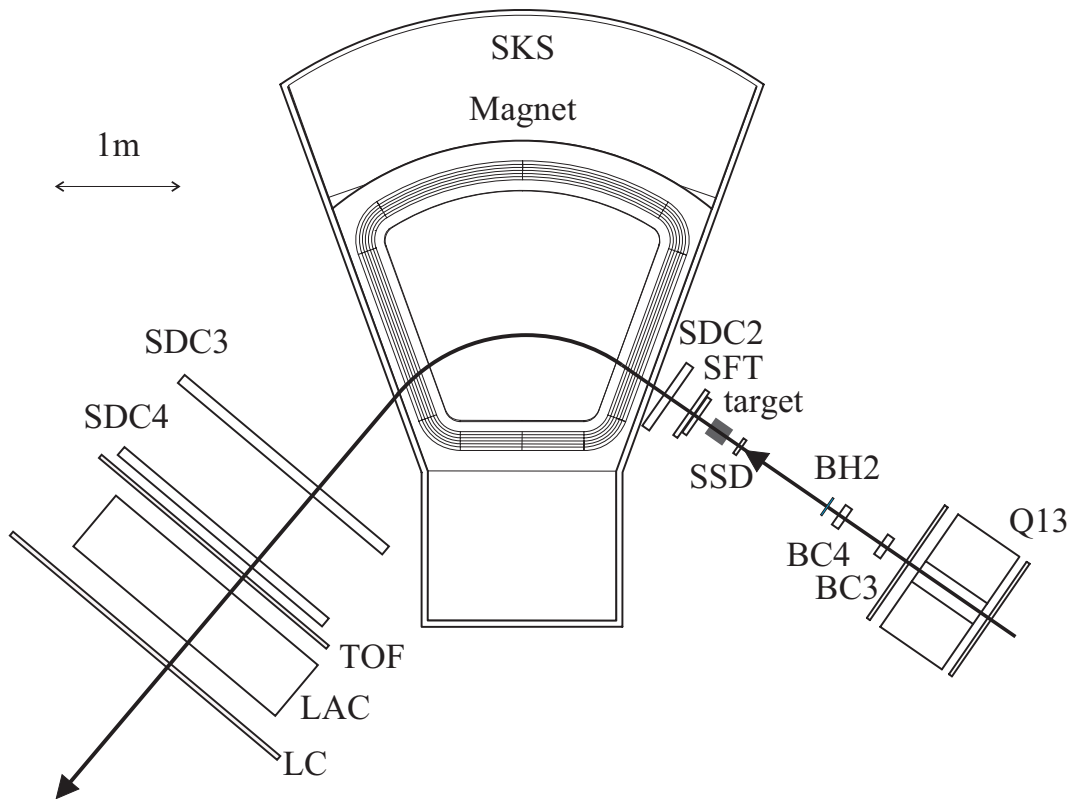


Figure 2.12: The schematic view of the SKS. SFT was scintillating fiber tracker. SDC2–4 were drift chambers. TOF was a plastic scintillation counter hodoscope for the Time-of-flight measurement. LAC was aerogel Čerenkov counter ($n=1.05$). LC was a Lucite (Acrylic) Čerenkov counter ($n=1.49$).

Trigger counters

Specifications of the trigger counters are listed in Table 2.5. In the trigger, a combination of three kinds of trigger counters were used to identify pions, kaons and protons. The TOF counter is sensitive to all charged particles, LAC are sensitive only to pions, and LC is insensitive to protons.

Table 2.5: Specifications of the particle identification counters in the SKS spectrometer

Name	Sensitive area W×H×T (mm)	Spec.	PMT (Hamamatsu)
TOF	2240×1000×30	32 segments	H1949
LAC	1050×1200×113	Aerogel; n=1.05	R1584-02
LC	2800×1400×40	28 segments, Acrylic; n=1.49	H1949, H6410

TOF

TOF is a segmented plastic scintillation hodoscope located at just a downstream of SDC4 to identify scattered particles by the time-of-flight measurement with BH2. Figure 2.13 shows a schematic view of TOF. The TOF counter was horizontally segmented into 32 pieces of 70×1000×30 mm³ scintillators. The signal of each segment was detected by small transit time spread phototubes (H1949) on the top and bottom sides. The typical time-of-flight resolution between TOF and BH2 was measured to be 85±6.2 ps (rms). This is sufficient to separate the scattered pions, kaons and protons.

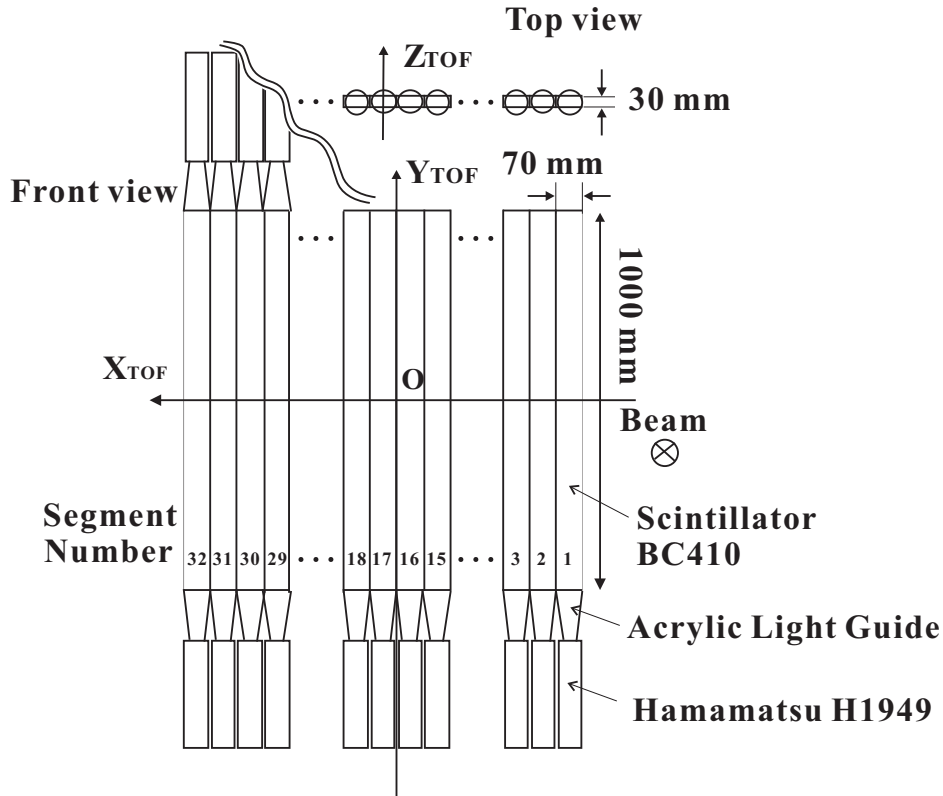


Figure 2.13: A schematic view of TOF.

LAC

LAC is a threshold-type silica aerogel Čerenkov counter to reject pions in the trigger level. As shown in Fig. 2.14, pions with a threshold of $0.45 \text{ GeV}/c$ were rejected by the refractive index of silica aerogel of 1.05. LAC was installed just behind of the TOF counter. Figure 2.15 shows a schematic view of LAC. The sensitive area of LAC was $1050 \times 1200 \times 113 \text{ mm}^3$. For the uniform efficiency without any dead space over a large sensitive area, LAC was not segmented but of a large one-box type. Phototubes which were sensitive to a single photon were placed on both sides. The number of photo electrons was typically 6 over the whole area for scattered pions at $0.9 \text{ GeV}/c$.

LC

LC is a threshold-type Čerenkov counter installed just downstream of LAC. Figure 2.16 shows a schematic view of LC. It was segmented into 28 vertical pieces of $100 \times 1400 \times 40 \text{ mm}^3$ Lucite (Acrylic) radiator with the reflection index of 1.49. Each segment is equipped with fast phototubes on the top and bottom sides. In the Acrylic radiator, a wavelength shifter of bis-MSB was mixed by 10 ppm. On the other hand, due to the scintillating radiation from the wavelength shifter, several percent of protons were detected below the threshold. As shown in Fig. 2.14, most of protons slower than $0.85 \text{ GeV}/c$ were rejected.

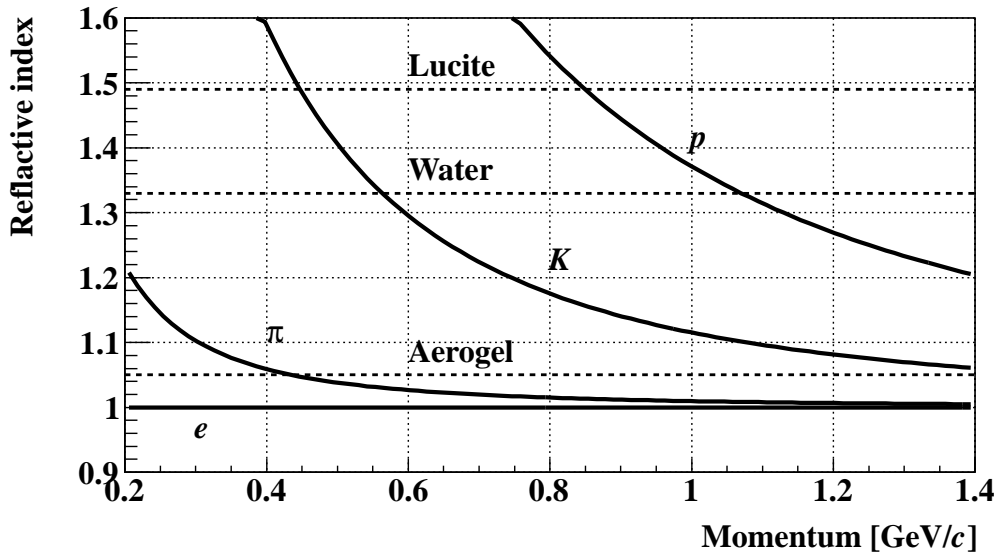


Figure 2.14: Threshold and refractive index for Čerenkov radiation as a function of the momentum.

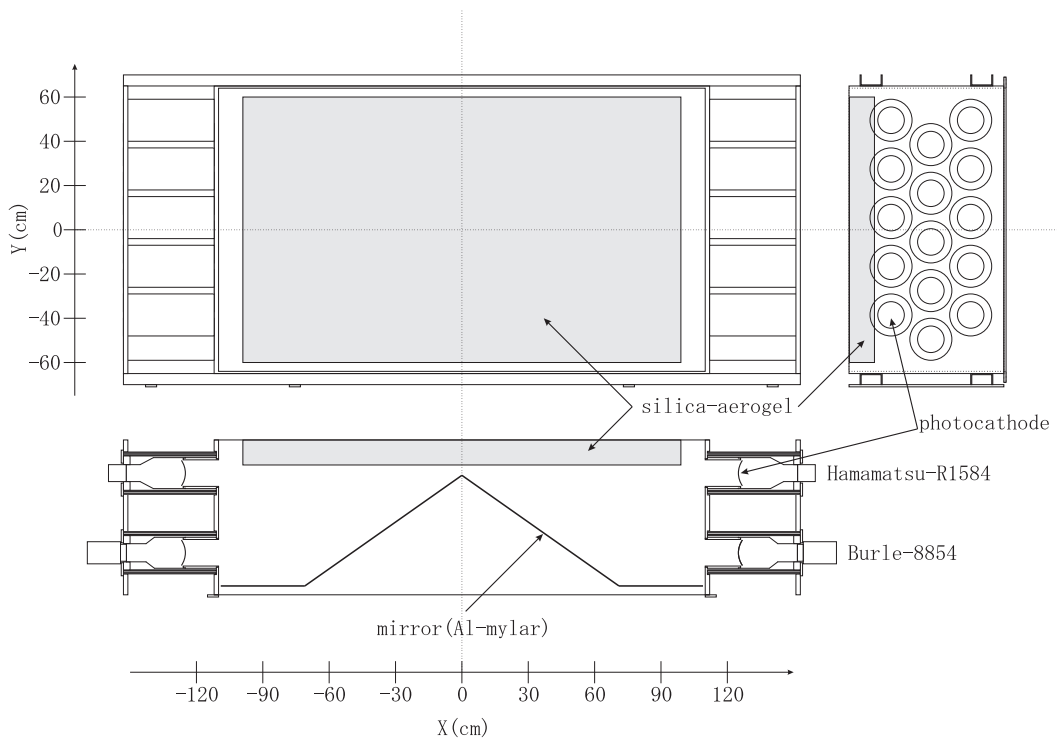


Figure 2.15: A schematic view of LAC.

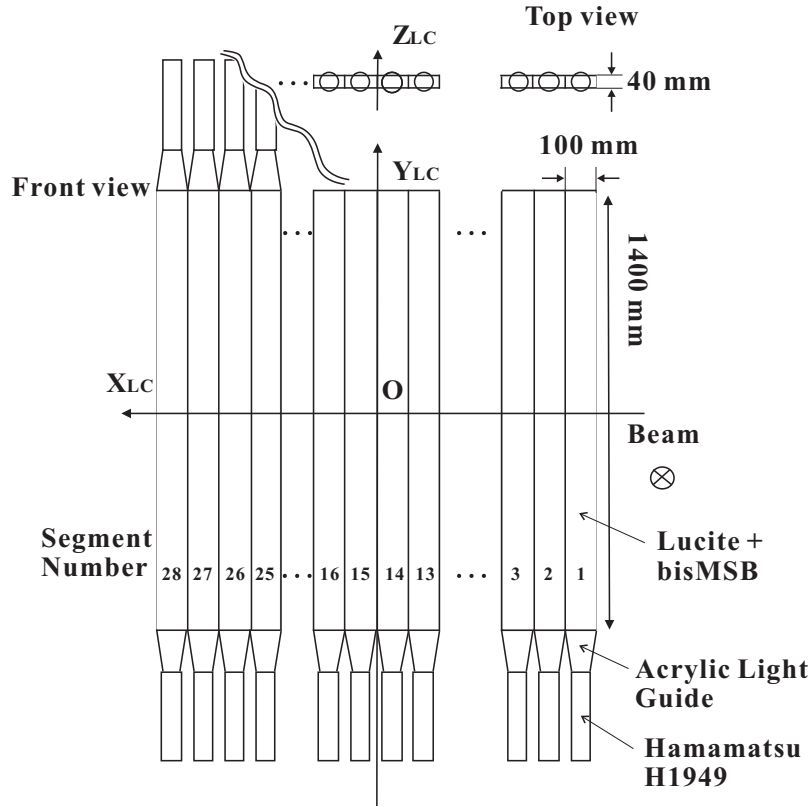


Figure 2.16: A schematic view of LC.

Tracking devices

Specifications of the tracking devices in SKS are summarized in Table 2.6.

Table 2.6: Specifications of the tracking devices in the SKS spectrometer.

Name	Effective area W×H (mm)	pitch (mm)	Wires	Angle (x, u, v) (°)	Typical Resolution (μm in r.m.s)
SFT	256×150	1.0(xx'), 0.75(uv)	$xx'vu$	0, +45, -45	200(xx'), 230(uv)
SDC2	400×150	5.0	$vv'uu'xx'$	0, +15, -15	200
SDC3	2140×1140	20	$vxuvxu$	0, +30, -30	300
SDC4	2140×1140	20	$vxuvxu$	0, +30, -30	300

SFT

The scintillation fiber tracker (SFT) was newly installed just upstream the target. SFT has a $xx'vu$ structure. The x and x' planes have a similar structure of BFT. The v and u planes tilted by 45 degrees are made of small scintillating fibers with 0.5 mm diameter to reduce materials as much as possible. For v and u planes, one MPPC reads out three bundled fibers to reduce the readout channels. The same read-out electronics as those for BFT was used.

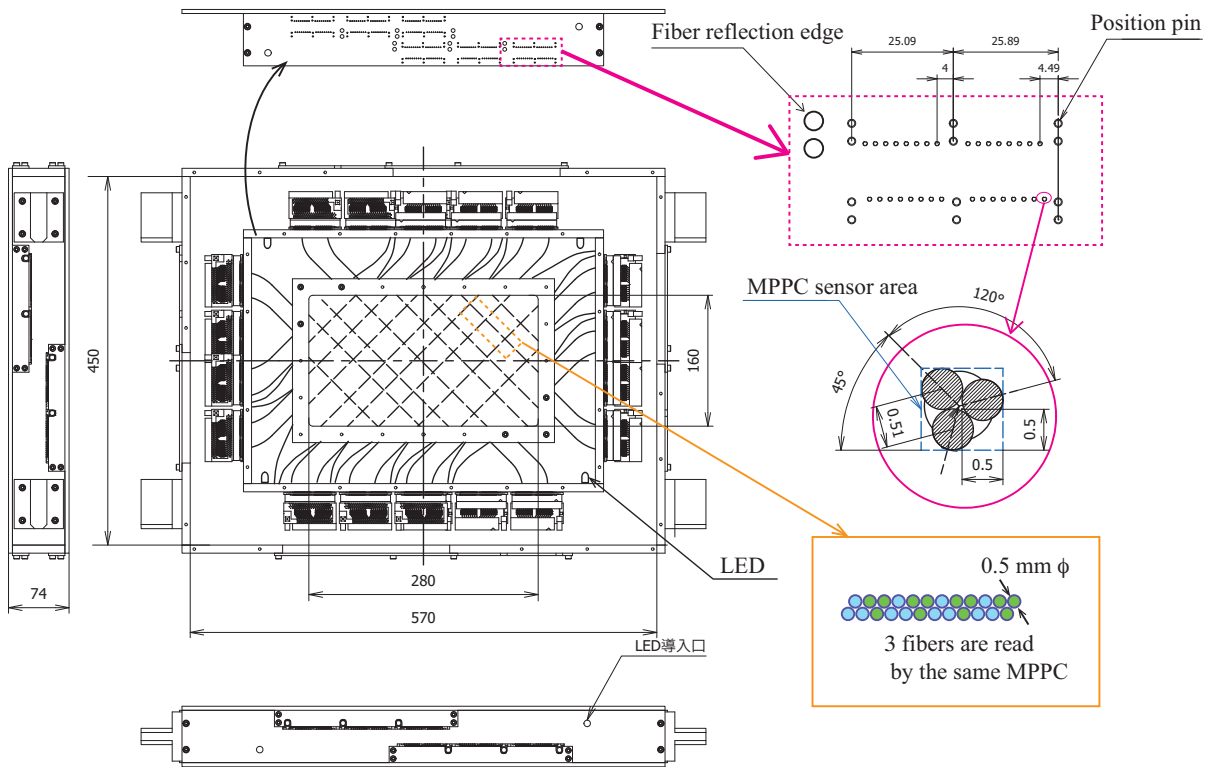


Figure 2.17: Schematic view of SFT.

SDC2

SDC2 is a drift chamber installed downstream of the SFT. The anode wire pitch of the SDC2 was 5 mm. The wire configuration of the SDC2 was $vv'uu'xx'$, where u and v wires were tilted $\pm 15^\circ$ with respect to the x wires. The sense wire was gold-plated $12.5 \mu\text{m}$ diameter tungsten wire, and the field wire was gold-plated $75 \mu\text{m}$ diameter copper-beryllium wire, and the cathode planes were made of $20 \mu\text{m}$ thick carbon pasted on a $12 \mu\text{m}$ thick aramid film. The gas mixture and read-out electronics were the same as those of BC3 and BC4.

SDC3 and SDC4

SDC3 and SDC4 are located at the exit of SKS. The size of the effective area was $2140 \times 1140 \text{ mm}^2$. The anode wire was a gold-plated $25 \mu\text{m}$ diameter tungsten wire, and both field wire and cathode wire were gold-plated $80 \mu\text{m}$ diameter copper-beryllium wire. The pitch of the cathode wires was 2 mm. SDC3 and SDC4 have $vxuvxu$ configuration, where u and v wires were tilted $\pm 30^\circ$ with respect to the x wires. The gas mixture was $\text{Ar}(50\%) + \text{C}_2\text{H}_6(50\%)$. The front-end read-out electronics of SDC3 and SDC4 was made of ASD chips. The timing information of the SDC3 and SDC4 hit was digitized by the TKO Dr.TII TDC module as described in Sec 2.6.

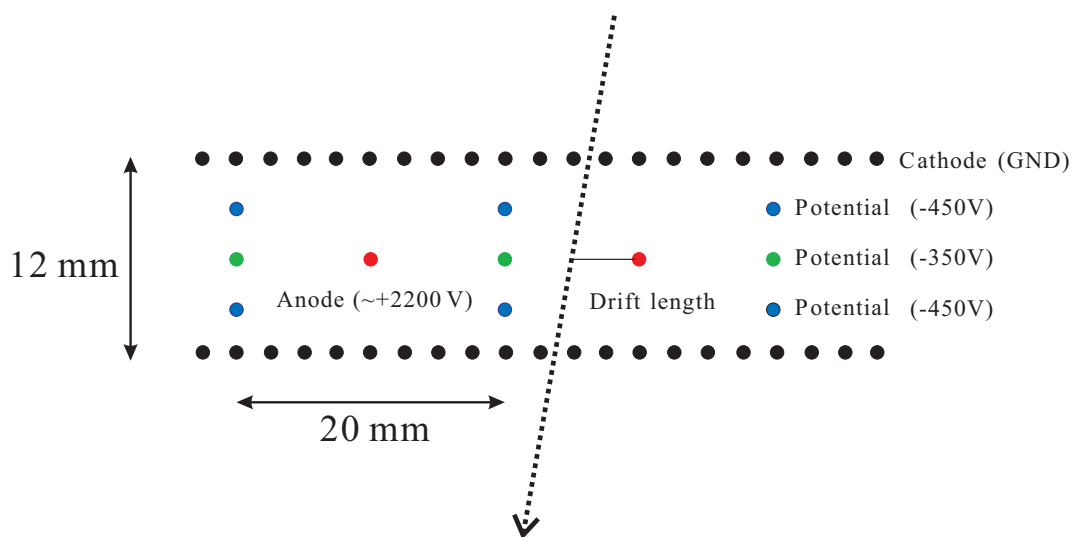


Figure 2.18: The cell structure of SDC3-4

2.6 Trigger

In the (π^-, K^+) reaction, many background particles are produced through the pion-nucleus reactions, such as $(\pi, p)X$ and $(\pi, \pi)X$. Especially, protons produced from $\pi^- p \rightarrow \pi^- \pi^0 p$ reaction is a main background in the SKS momentum acceptance because the cross section is 10^3 times larger than that for the (π^-, K^+) reaction. Therefore, a powerful (π^-, K^+) trigger system is very important. In the present system, the 1st level (π, K) trigger, TOF-LC matrix trigger and the 2nd level mass-trigger systems are introduced. Prescaled beam trigger and (π, π) trigger was mixed into them.

The 1st level (π, K) trigger

The 1st level (π, K) trigger was comprised of four kinds of counters, BH2, TOF, LAC and LC, and defines as:

$$PIK \equiv BH2 \times TOF \times \overline{LAC} \times LC$$

BH2, TOF, and LC had two PMTs at both ends, and mean timer modules were used to remove the incident position dependence of the trigger timing. The PIK trigger logic diagram is shown in Fig. 2.19.

The BH2 timing was used as the STOP signal of the TDC's for BFT, BC3, BC4, SFT and SDC2, while the TOF timing was used as stop for SDC3,4 because the flight time from BH2 to TOF varies a lot depending on the different flight paths and momenta of scattered particles.

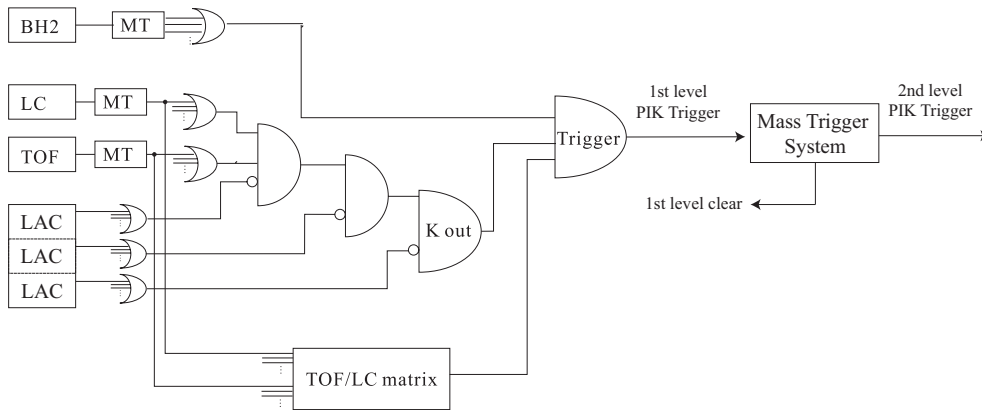


Figure 2.19: PIK trigger logic diagram.

Beam and (π, π) trigger

The 1st level beam and (π, π) trigger are defined as,

$$\begin{aligned} BEAM &\equiv BH2 \\ PIFI &\equiv BH2 \times TOF \times LC \end{aligned}$$

These triggers are mixed in the (π, K) trigger with prescale factors to monitor each counter's efficiency and to adjust calibration parameters for detectors. The prescale factor is $1/(256 \times 256 \times 4)$ in the beam trigger and $1/300$ in the (π, π) trigger, respectively.

Matrix trigger with LC and TOF

In high rate pion beam experiments, many of particles scattered at other materials such as SKS yoke and beam line Q-magnets hit the TOF and LC, and make fake triggers. To reduce such fake triggers, a matrix trigger is introduced.

The matrix trigger is generated when the appropriate hit combinations between TOF and LC segments are matched. For constructing the matrix trigger, we used an FPGA module called TUL (Tohoku Universal Logic Module) [56]. Figure 2.20 shows the selected combinations of the TOF and LC segments. In the figure, the selected region is indicated by solid lines and the background events are located out of the region. The 1st level (π, K) trigger is reduced by 10% with the matrix trigger.

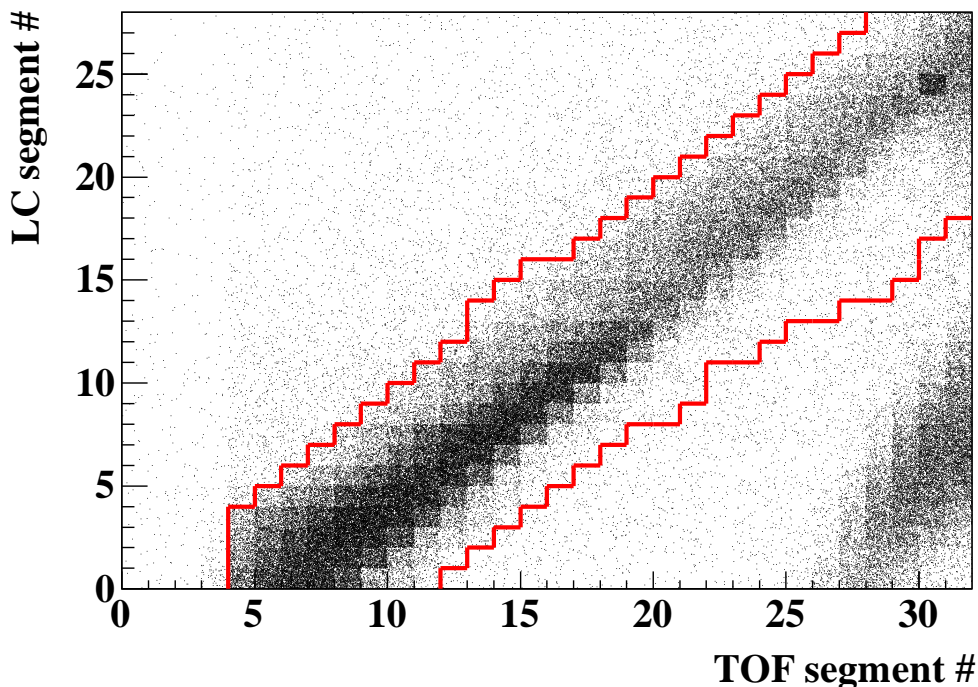


Figure 2.20: The hit pattern of TOF and LC segments without the matrix trigger. The selected TOF and LC segment region for the matrix trigger was indicated in red lines.

The 2nd level mass trigger

The outgoing particles are roughly identified from the difference of time-of-flight by selecting hit combination of TOF and LC. The particle identification can be done by setting a suitable window against time-of-flight of TOF.

The trigger scheme for the mass trigger is illustrated in Fig. 2.21. The timing information of the TOF signals were digitized with a LeCroy 4303 TFC(Time-to-Fera Converter) module. The hit addresses and the timing information of TOF were stored in the memories in the FERA driver, and the hit information of LC was stored in TUL. The FERA driver sends the 4 bit of hit address information and 9 bit of time-of-flight information to TUL. Hit information of TOF and LC, and time-of-flight information is handled in the TUL module. If the time-of-flight of TOF is in the time window we set, the 2nd level (π, K) trigger is generated. If not, the 1st trigger clear signal is generated and all the stored data in each DAQ modules is cleared. The decision time of the mass trigger was about $15 \mu\text{s}$. In the present experiment, 60% of the 1st level (π, K) triggers are rejected.

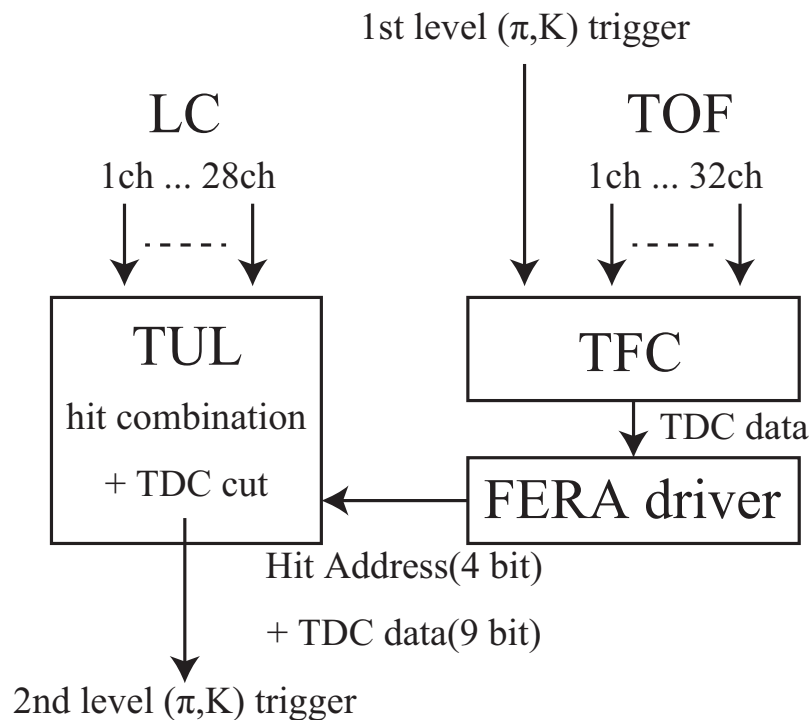


Figure 2.21: Logic Scheme of the mass trigger.

2.7 Data-acquisition system

Figure 2.22 shows a diagram of the data-acquisition system. The raw signals of trigger counters and SDC3 and SDC4 were digitized with the TKO high resolution TDC and ADC modules and the TKO TDC (Dr.TII) modules [57], respectively. For the TKO modules, the digitized signals were transferred to the VME-SMP (Super Memory Partner), which was installed in the VME box together with a VME-CPU module. Then, the data were read out by the VME-CPU (V7807RC) module and transferred to the host computer.

The timing information of the BC3-4 and SDC2 was digitized by the FINESSE Multi-hit TDC installed in the COPPER modules. COmmon Pipelined Platform for Electronics Readout(COPPER) [54] is a new platform module for the KEK-VME specification that realizes various types of analog-to-digital conversion and pipelines digital data processing functions in a unified scheme. The MHTDC module encoded the timing information with an accuracy of 1 ns. The BC3, BC4 and SDC2 data on the COPPER modules were directly transferred to the host computer by the SiTCP connection. The data-acquisition cycle was processed event by event.

The timing information of the BFT and SFT was digitized by the EASIROC Multi-hit TDC [53]. EASIROC is developed by Linear Accelerator Laboratory (LAL) in France. EASIROC has many functions such as amplifier, shape EASIROC chip digitized leading and trailing edge as time-over-threshold with an accuracy of 1 ns. Since the EASIROC board does not have CPU, data acquisition is controlled by daughter computer with SiTCP communication. The data were transferred to host computer via the daughter computer.

The signal from SSD was digitized by the FADC system (APVDAQ). At first analog signal is multiplexed by the APV25 chip mounted on the SSD board, then the serialized signal transferred to FADC VME module (APVDAQ) via a CAT7 Ethernet cable every 25 ns. APVDAQ digitizes the analog signal, and transfers it to the VME-CPU controller (XVB601).

For building up an event by combining data sets coming from the different modules, we need to write the event number and the spill number to each data set and to check their consistency event by event in the event building. For this purpose, we have developed a trigger/tag distribution system. When the trigger signal was generated, the Master Trigger Module (MTM) accepted the trigger signal and distributed the event and spill numbers to Receiver Modules (RM) in each node by using Ethernet cables. After finishing the analog to digital conversion of all the modules in each node, MTM distributed the read-out signal to all the RMs and the event data with the same event and spill numbers were transferred to the host computer. The event and spill numbers were distributed to the data bus by RM in each node. The information of those numbers were transferred together with the digitized raw data to the host computer.

The data transferred from each module to the host computer were at first processed by the Event-Builder. Then they were transferred to the Event-Distributor and to HDD data storage as well as to the on-line analyzer.

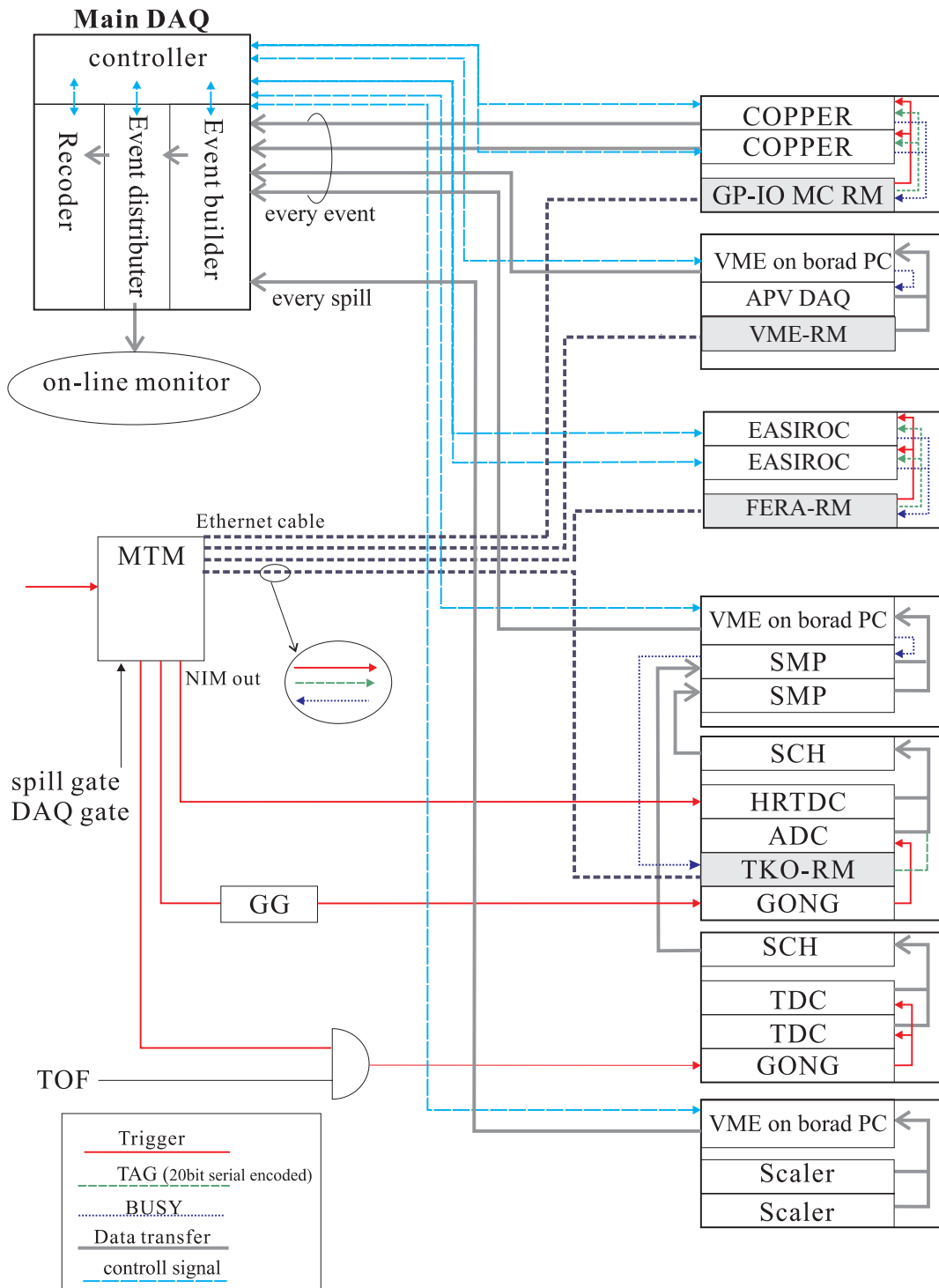


Figure 2.22: Diagram of the data-acquisition system.

2.8 Lithium-6 target

An enriched ${}^6\text{Li}$ target (95.54%) of 3.5 g/cm^2 in thickness and $70^W \times 40^H (\text{mm}^2)$ in size was used as shown in Fig 2.23. The typical beam profile, $56^W \times 28^H (\text{mm}^2)$ (FWTM), is fully covered with the target. Although, it is the best preservation way to use aluminium laminated package in order to suppress the oxidization of Lithium, we are not able to monitor where the Lithium is located. Therefore, we use (Z-86) bag [58] so that we could monitor the position.

Z-86 has a low rate of the oxygen transmission ($80 \text{ ml/m}^2/\text{MPa}$ at 20C°) and a two-layer structure of polyethylene, oriented polypropylene coated with polyvinylidene chloride. The thickness was $55 \mu\text{m}$. The ${}^6\text{Li}$ target was doubly packed with Z86 in the Argon gas grove box. Before and after the experiment, we checked oxidization of ${}^6\text{Li}$, and there was no oxidization of surface at visual monitoring level.



Figure 2.23: The Picture of ${}^6\text{Li}$ target

2.9 Data summary

The ${}^6_\Lambda\text{H}$ production data by the ${}^6\text{Li}(\pi^-, K^+)$ reaction were taken in two cycles in December 2012 and in January 2013 as listed in Table 2.7. The total number of pions irradiated on the ${}^6\text{Li}$ target was 2.1×10^{12} . At first, we took ${}^{12}_\Lambda\text{C}$ production data to evaluate the missing-mass resolution. Next, we made measurements of the Σ^- and Σ^+ production reaction from hydrogen on a $(\text{CH}_2)_n$ target at a beam momentum of 1.377 GeV/ c . We also performed the beam-through runs at four momentum settings, 0.8, 0.9, 1.0 and 1.2 GeV/ c , with and without the ${}^6\text{Li}$ target to evaluate the amount of energy straggling and the energy loss in the target.

Table 2.7: Summary of runs. Target material and thickness, and beam momentum and intensity are listed.

run	target		momentum (GeV/ c)	beam	
	material	thickness (g/cm 2)		intensity (pion/spill)	irradiated pion
${}^6\text{Li}(\pi^-, K^+)$	${}^6\text{Li}$	3.5	1.2	$1.2\text{--}1.4 \times 10^7$	2.1×10^{12}
${}^{12}\text{C}(\pi^+, K^+)$	graphite	3.6	1.2	4.1×10^6	5.4×10^{10}
$p(\pi^-, K^+)\Sigma^-$	$(\text{CH}_2)_n$	3.4	1.377	1.3×10^7	4.1×10^{10}
$p(\pi^+, K^+)\Sigma^+$	$(\text{CH}_2)_n$	3.4	1.377	3.5×10^6	3.1×10^9
beam-through	none		0.8, 0.9, 1.0, 1.2	$\sim 10^4$	

Chapter 3

Data Analysis

3.1 Outline

The mass of the produced particle (M) was obtained as a missing mass in the (π, K) reaction from

$$M = \sqrt{(E_\pi + M_A - E_K)^2 - (p_\pi^2 + p_K^2 - 2p_\pi p_K \cos \theta_{\pi K})},$$

where E_π and p_π are the total energy and momentum of a pion, E_K and p_K are those of a kaon, M_A is the mass of a target nucleus, and $\theta_{\pi K}$ is the scattering angle.

The beam momentum and kaon momentum were reconstructed from the tracking information on BFT, BCs, SFT and SDCs. At the first stage of the tracking analysis, straight-line track candidates were determined both at the entrance and the exit of the spectrometer system. Then the best track candidates were selected from the combination of the straight-line tracks so as to give the least chi-squares in the momentum reconstruction. For the track reconstruction of K1.8 beam line spectrometer, a beam transport matrix in third-order was used. In the track reconstruction of SKS, a calculated field map was used, and the SKS track was reconstructed with the Runge-Kutta method. After the track reconstruction, the identification of kaon was carried out by using the time-of-flight between BH2 and TOF with the flight path and the reconstructed momentum of SKS. Then, a vertex point of the (π, K) reaction event was reconstructed from the trajectories of pion and kaon, and finally the missing mass was obtained.

3.2 Analysis of beam

3.2.1 Identification of triggered beam particles

At first, incident hadron beam such as pion, kaon and proton was separated with the electro static separator (ESS1,2) as already shown in Fig.2.3. The contamination of proton and kaon was negligibly small. However, light lepton particles such as electron and muon can not be rejected with ESS. The contamination of electron was estimated with GC hits at low intensity beam and the contamination of muon was estimated from the Decay TURTLE simulation [59]. The details are described in Chap. 4.2.1. An incident triggered beam was selected by a time window of 2 ns in the BH2 hits as shown in Fig 3.1. The ratio of single hit of BH2 within the 2 ns was estimated to be $91.0 \pm 2.0\%$. In present analysis, we selected only single hit of BH2 as triggered segment.

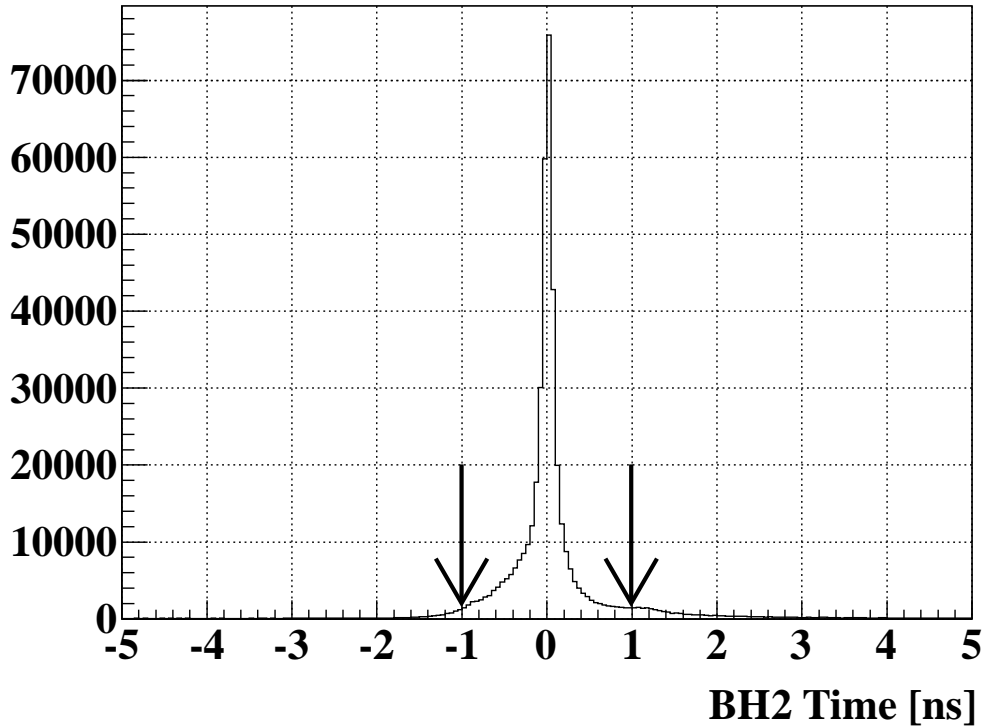


Figure 3.1: Typical BH2 time spectrum of the incident beam particles. The selected time window was indicated by arrows.

3.2.2 BFT analysis

The timing information of BFT was digitized by the EASIROC multihit-tdc by the sampling time interval of 1 ns (1 GHz sampling). In the digitization, both leading edge and trailing edge information of raw signals were taken as time over threshold (TOT). The time resolution of BFT can be improved with the time walk correction by using the TOT. Figure 3.2 shows the correlation of the TOT and time before the correction. The

time is corrected with a 2nd-order poly-nominal function. After the correction, the time resolution is found to be 1.12 ± 0.03 ns.

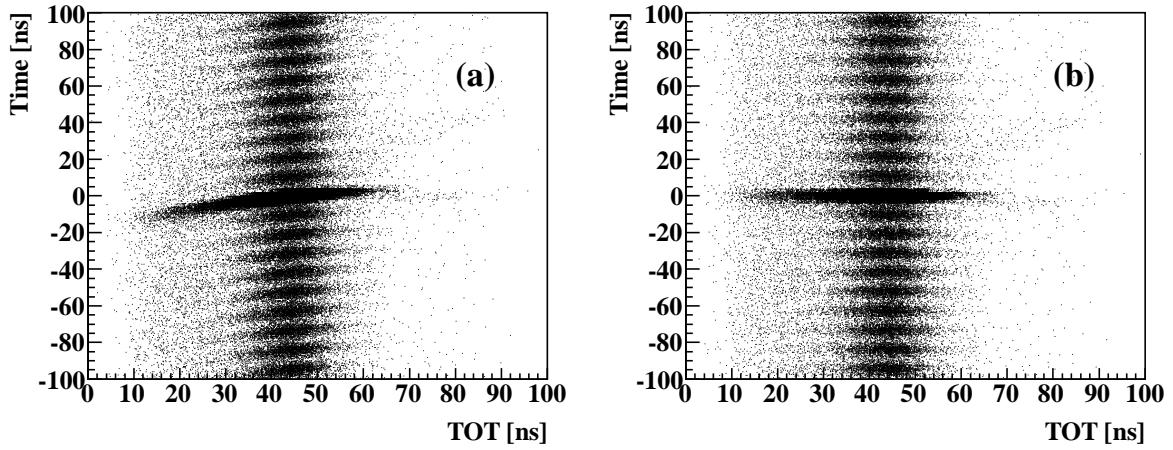


Figure 3.2: Slewing correction of BFT.

Figure 3.3 shows the time projection of Figure 3.2(b). In the present analysis, the time gate with a ± 3 ns width was set as indicated by arrows. When there were hits on

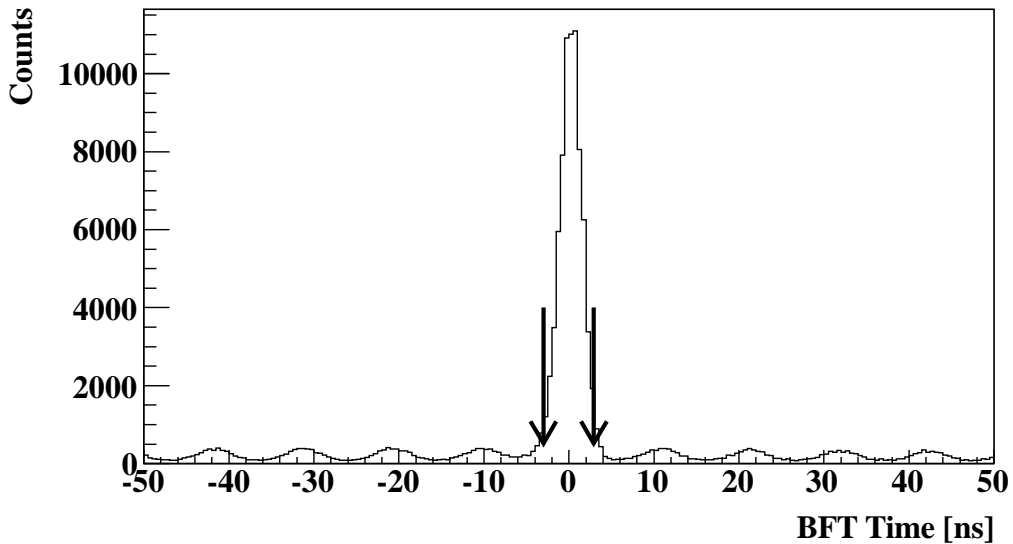


Figure 3.3: Typical TDC distribution of BFT. The Tdc distribution was the sum of all hits in a fiber. All multi-hit signals were shown in the distribution.

adjacent fibers whose signal is matched each other within the ± 3 ns time gate, those fibers were made up into a cluster. For the tracking analysis, the position of the central fiber in the cluster was used.

3.2.3 BC3 and BC4 local tracking

BC3 and BC4 drift length calculation

For the position calibration of BC3 and BC4, at first, the TDC information was converted to the drift time information. Figure 3.4 shows a typical TDC distribution for one of the BC3 and BC4 layers. A bump structure in the tail of the distribution was caused by satellite signals due to the ringing in the ASD card. Those satellite signal events were rejected in the tracking process because the timing of the satellite signals was far from the drift time range and their coincidence rate was quite low. The flat background distribution was caused by accidental events due to high intensity beam pions. The

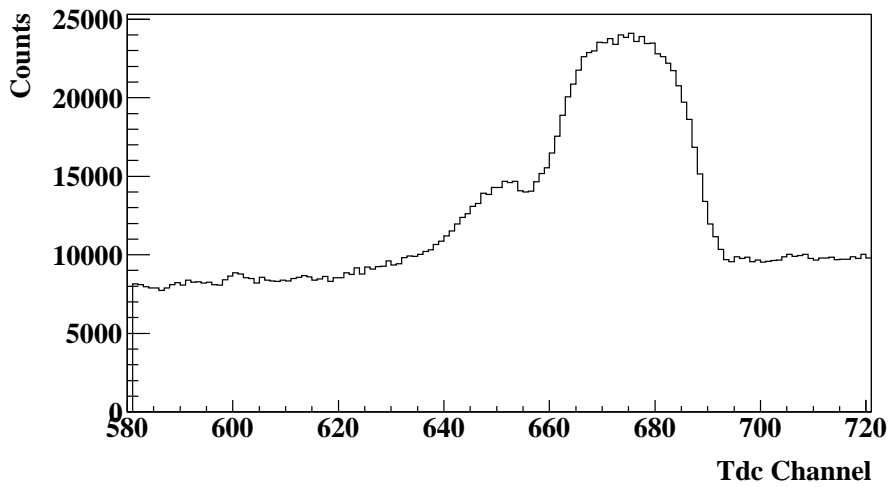


Figure 3.4: Typical TDC distribution of one of BC3-4 layers. The TDC distribution was the sum of all hits in a layer, and all multi-hit signals were shown in the distribution.

origin of the drift timing was roughly determined with the edge of the TDC distribution (about 700 ch in Fig. 3.4) and the TDC channels were converted to the drift time using the MHTDC channel width of 1 ns. The conversion function from the drift time to drift length was obtained with the following equation by assuming the uniform hit distribution,

$$DL(t) = \frac{\int_{t_0}^t dt DT(t)}{\int_{t_0}^{t_{max}} dt DT(t)} \times \text{max drift length}, \quad (3.1)$$

where t_0 is the time origin, t_{max} is the maximum drift time for the maximum drift length, and $DT(t)$ is the observed drift time distribution.

Figure 3.5 shows a scatter plot between the drift time and the drift length ($DL(t)$) for one of the BC3 and BC4 layers. The scatter plot was fitted by using a 5th-order polynomial function. This function was optimized in iteration.

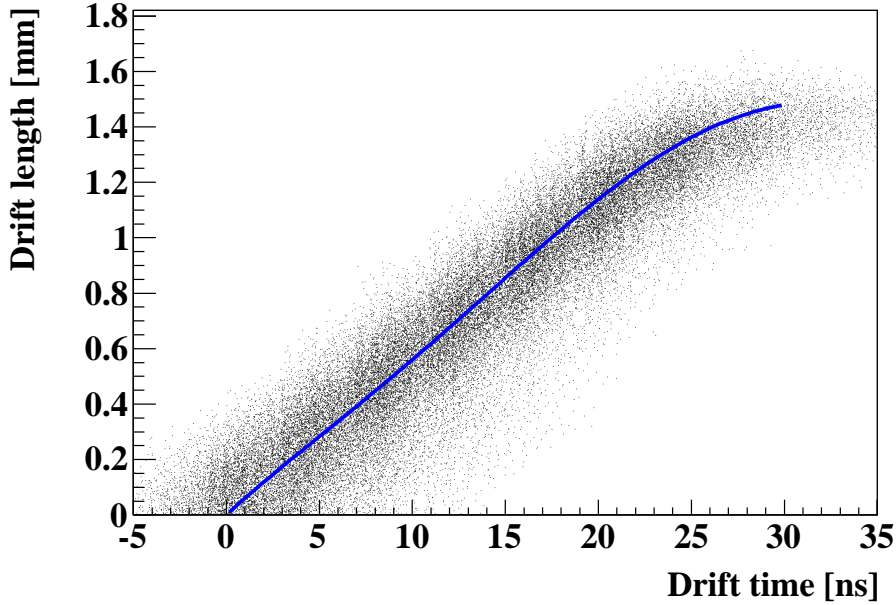


Figure 3.5: A scatter plot between the drift time and the drift length of one of the BC3 layers with the fitting result in black line. The scatter plot was the sum of all hits in a layer.

Table 3.1: The position resolution of each layers.

BC3-Layer	resolution [μm]	Layer	resolution [μm]
BC3- x	210 ± 0.4	BC4- u	197 ± 0.4
BC3- x'	200 ± 0.4	BC4- u'	196 ± 0.4
BC3- u	205 ± 0.5	BC4- v	203 ± 0.5
BC3- u'	203 ± 0.4	BC4- v'	205 ± 0.5
BC3- v	196 ± 0.4	BC4- x	213 ± 0.7
BC3- v'	208 ± 0.5	BC4- x'	219 ± 0.7

Local straight track search

In finding BC3 and BC4 tracks, all combination of all the hit positions in each layer were examined. Those local straight tracks were found by using the least squares method. The local position coordinate was shown in Fig. 3.6. For the origin of the local coordinate, we defined optical focal points as VI and VO. The VI is the position of BFT and the VO is 130 mm downstream of the end-guard of the exit Q-magnet (Q13). The location of the VI and VO points were shown in Fig. 3.7.

The track parameters (x_0 , y_0 , $u_0(dx/dz)$, $v_0(dy/dz)$) and the drift direction (L/R) were obtained for a local track candidates giving the least χ^2 . Figure 3.8(b) shows a χ^2 distribution of the BC3 and BC4 tracking. In the local track search, the tracks were accepted to be less than 30 of the χ^2 value. Figure 3.8(a) shows a residual distribution of one of the BC3 and BC4 layers. In the calculation of the residual distribution, the calculated layer was not included in the tracking analysis. The obtained position resolution of each layer is listed in Table. 3.1.

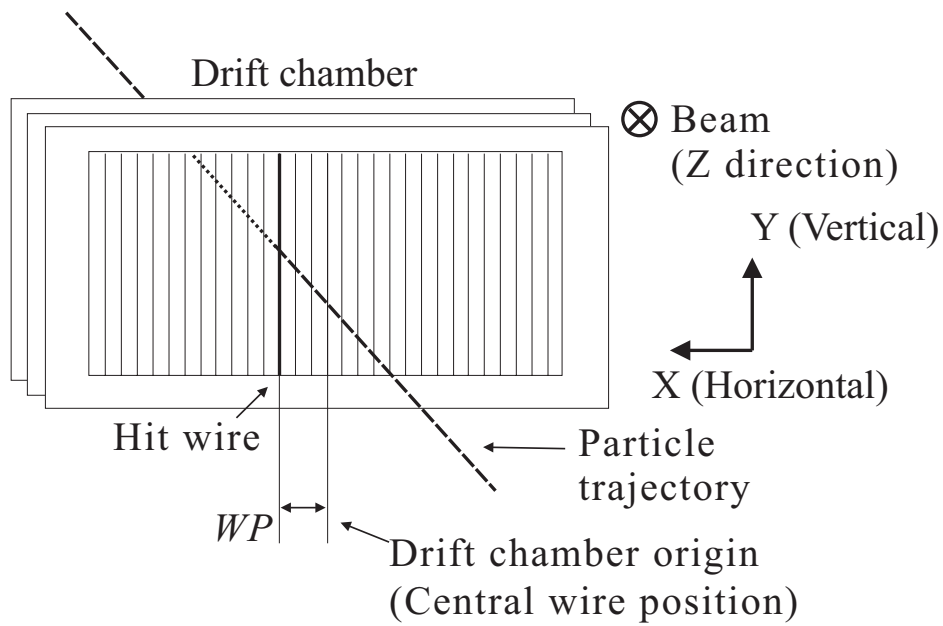


Figure 3.6: Local position coordinate for the local straight tracking.

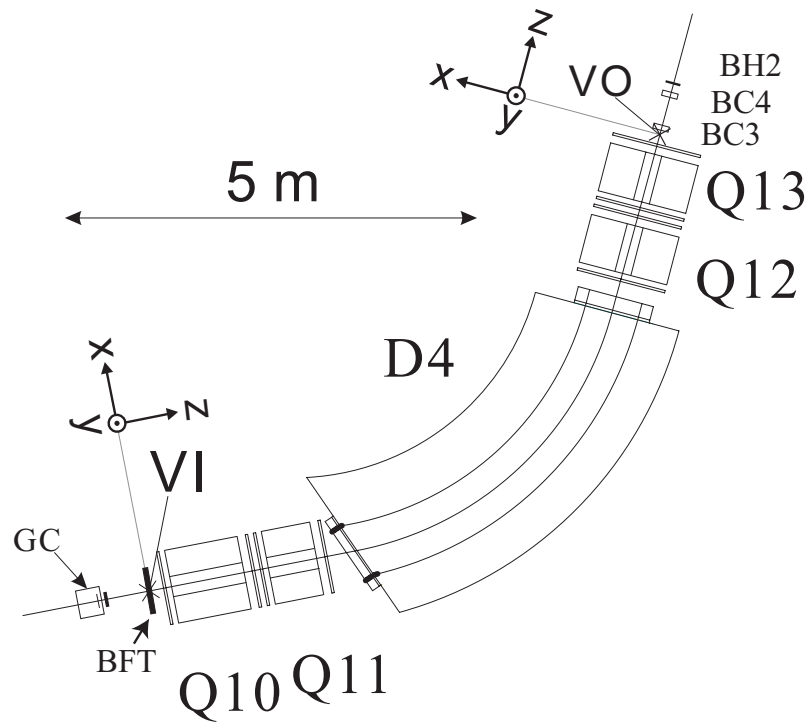


Figure 3.7: The VI and VO point in the K1.8 beam line spectrometer. The position of VI and VO which were the origin of the local coordinate.

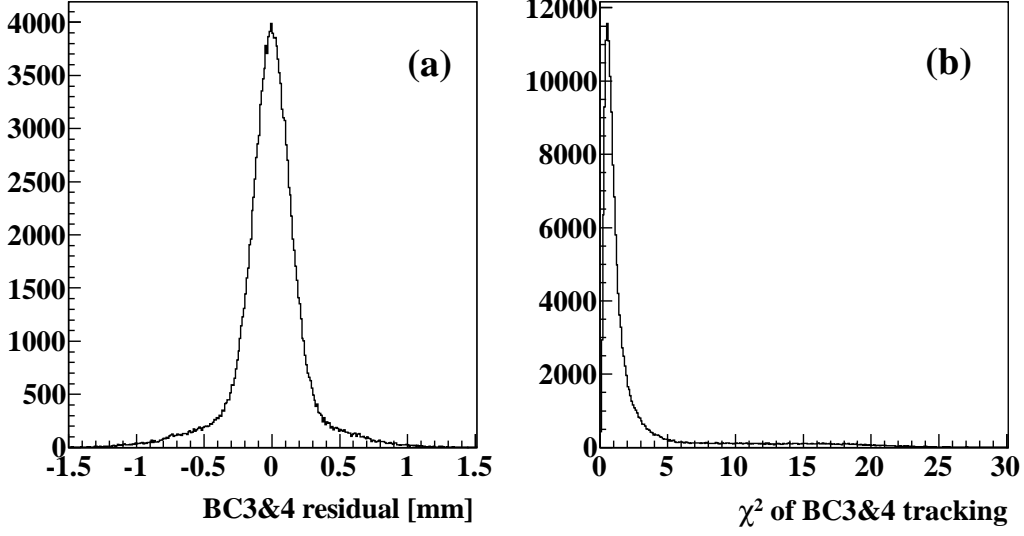


Figure 3.8: (a) Typical residual distribution of one of the BC3·4 layers. (b) Typical χ^2 distribution of the BC3·4 tracking.

3.2.4 Beam momentum reconstruction

The beam momentum was analysed from the hit position information of BFT and the local track information of BC3 and BC4 by using the 3rd-order transport matrix M calculated with the ORBIT code [60] as follows,

$$\vec{X}_{in} = M(\vec{X}_{out}, \delta),$$

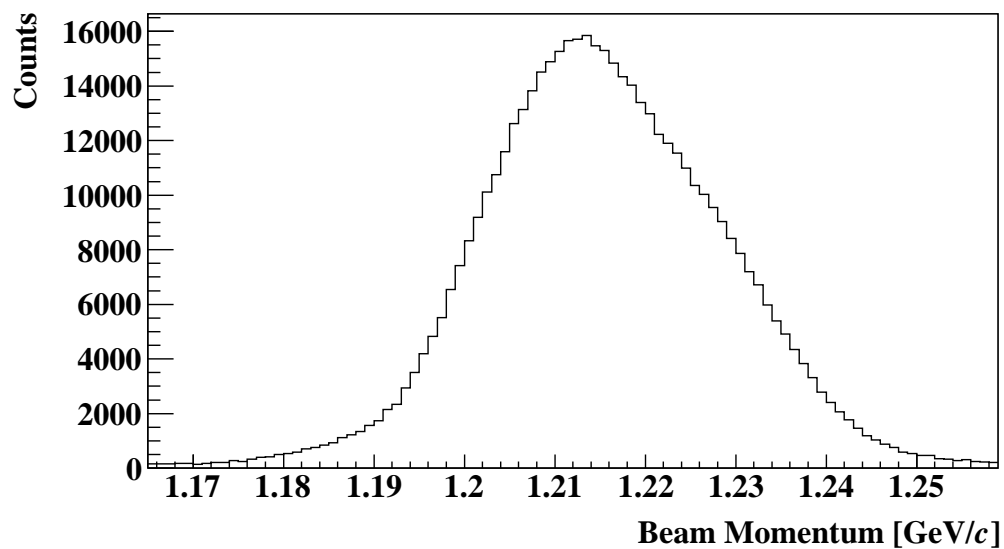
$$\vec{X}_{in} = \left(x_{in}, y_{in}, \frac{dx_{in}}{dz}, \frac{dy_{in}}{dz} \right),$$

$$\vec{X}_{out} = \left(x_{out}, y_{out}, \frac{dx_{out}}{dz}, \frac{dy_{out}}{dz} \right),$$

where \vec{X}_{in} and \vec{X}_{out} are the horizontal and vertical positions and their derivatives at the entrance (VI) and the exit (VO) of the K1.8 beam line spectrometer and δ is momentum deviation from the central momentum denoted as $p = p_0(1 + \delta)$, where p_0 is the central momentum. Since we have only one information x_{in} in \vec{X}_{in} from the hit information of BFT, a third-order polynomial equation $x_{in} = f(\vec{X}_{out}, \delta)$ was used to estimate the δ .

In the ORBIT code, the properties of the K1.8 beam line spectrometer magnets, the effective magnetic length, aperture, field strength of the central ray, and bending angle and the radius of central orbit for the dipole magnet are inputs. The effective magnetic length was determined from a measured magnetic field distribution. The aperture was taken from the design value of the spectrometer magnets. The properties of the magnetic fields of all the magnets were also calculated by using the excitation curve.

Figure 3.9 shows a beam momentum distribution for ${}^6\text{Li}(\pi^-, K^+)$ production runs. The single track events were selected. The momentum bite was typically $\pm 2\%$. The momentum distribution depends on the slit condition. The slit condition in the present experiment was listed in Table 3.2.

Figure 3.9: Typical distribution of the beam momentum at 1.2 GeV/ c Table 3.2: Slit condition of ${}^6\text{Li}(\pi^-, K^+)$ production reaction

Slit	upper [mm]	lower [mm]
IFH	+70	-70
IFV	+2.6	-1.0
Mom	+60	-60
1st mass slit	+1.69	-1.69
2nd mass slit	+1.76	-1.76

The other parameters, y_{in} , $\frac{dx_{in}}{dz}$ and $\frac{dy_{in}}{dz}$ of \vec{X}_{in} are also obtained in reconstructing the momentum. Figure 3.10 shows typical beam profile in vertical and horizontal at VI. The events within the indicated arrows are accepted as good beam pion tracks to suppress the $\pi \rightarrow \mu$ decay events.

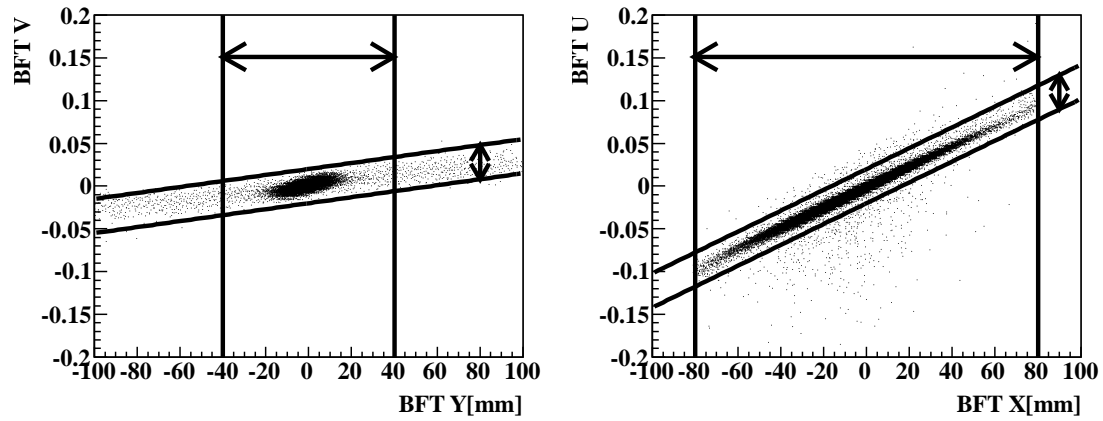


Figure 3.10: Typical distribution of XY and UV at BFT calculated from δ

3.3 Analysis of scattered particles

3.3.1 Hodoscope cut

In order to reduce background particles and the analysis time, hodoscope cuts were applied to TOF-ADC before local straight tracking. Large ADC hits in TOF were rejected as proton like events. The ADC cut region was set for each segment according to a simulation. In this cut, 10% of all events are rejected.

3.3.2 SFT and SDC2 local tracking

The hit information of SFT was selected in the time window with ± 3 ns after slewing correction in the same way as BFT analysis. When there were hits on adjacent fibers, those fibers were made up in to a cluster within the maximum cluster size of three. The hit information of SDC2 is obtained in the same method as in BC3 and BC4.

In finding SFT and SDC2 local tracks, all combinations of all the hit positions in each layer were examined. Those local straight tracks were found by using the least squares method. The minimum number of planes was required to be seven.

Figure 3.11 (a) – (c) shows a typical residual distribution of SFT and SDC2 tracking of SFT-X layer (a), SFT-U layer (b) and one of the SDC2 layer (c). The position resolution was $200 \mu\text{m}$ in SFT-X, $230 \mu\text{m}$ in SFT-UV and $200 \mu\text{m}$ in SDC2, respectively. In the local track search, the accepted χ^2 value was selected to be less than 30 as shown in Fig. 3.11(d).

3.3.3 SDC3 and SDC4 local tracking

The hit information of SDC3 and SDC4 was obtained with the same method as in BC3, BC4 and SDC2. For the SDC3 and SDC4 tracking, all combinations of all the hit positions in each layer were examined. The minimum number of planes was required to be nine. Figure 3.12 shows a typical residual distribution of one of the SDC3 and SDC4 layers. The position resolution was $300 \mu\text{m}$. In the local track search, the accepted χ^2 value was selected to be less than 20.

3.3.4 Momentum reconstruction of a scattered particles

The momentum of the scattered particle was determined by reconstructing a trajectory from the hit positions. The reconstruction was carried out with the Runge-Kutta method [61] for each particle using a calculated magnetic field map. The magnetic field map was calculated with the ANSYS code. The trajectory and the momentum were optimized by minimizing the following χ^2 values iteratively.

$$\chi_{sks}^2 \equiv \frac{1}{n-5} \sum_{i=1}^n \left(\frac{x_i^{tracking} - x_i^{data}}{w_i} \right)^2,$$

where n is the number of the chamber planes with a hit, $x_i^{tracking}$ and x_i^{data} are the hit position on the i -th plane in the tracking in and the data, and w_i is the position resolution of the i -th plane.

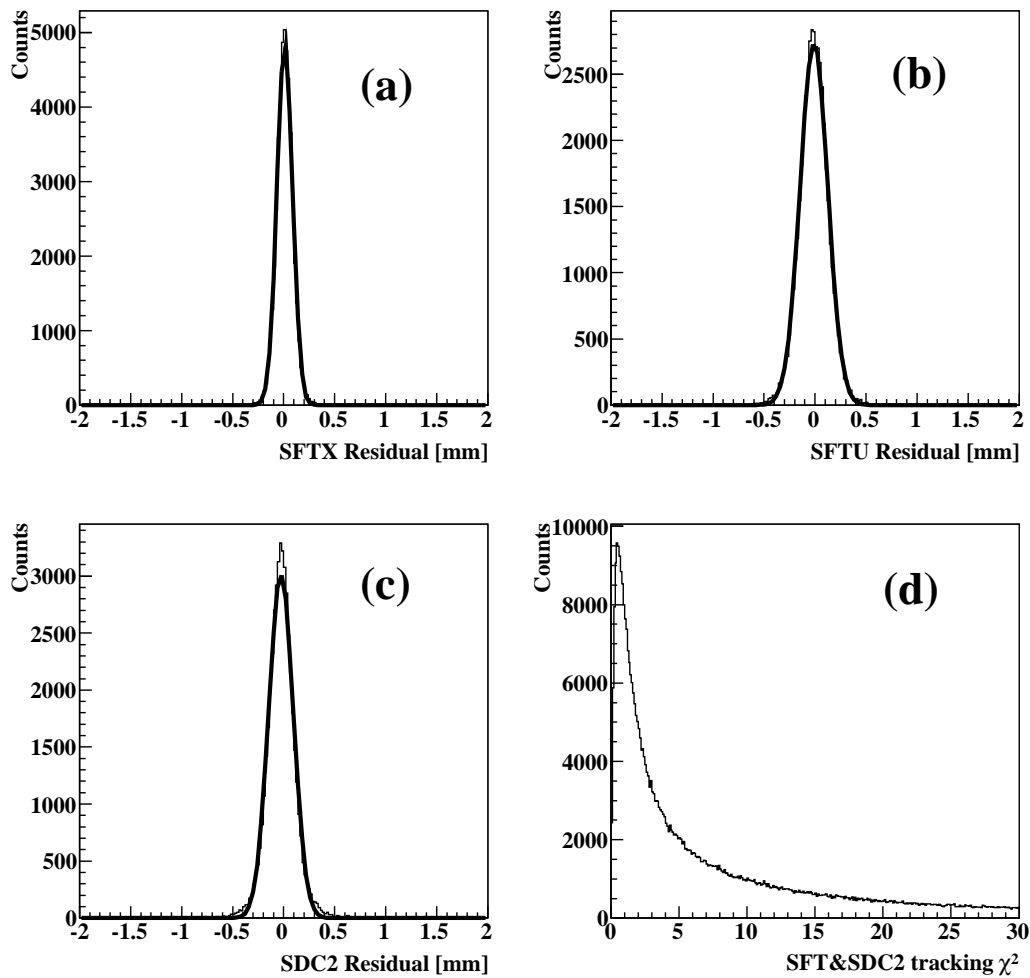


Figure 3.11: Typical residual and χ^2 distributions of SFT-SDC2 local tracking. (a) shows the residual of SFT-X, (b) shows the that of SFT-U and (c) shows the that of one of the SDC2 layer. (d) shows the typical χ^2 distribution.

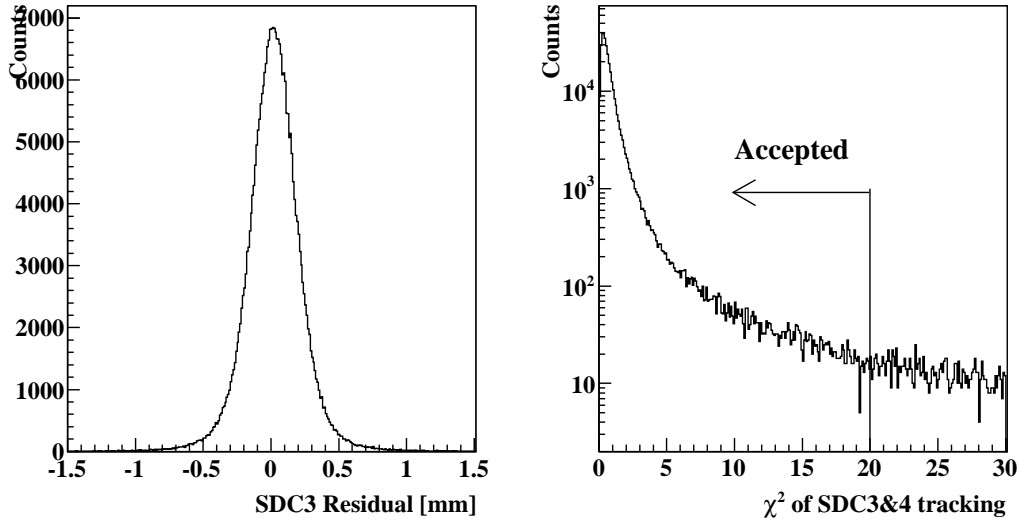


Figure 3.12: Typical residual distribution of one of the SDC3·4 planes (left), and χ^2 distribution of SDC3·4 (right).

The fitting parameters were the momentum (p), the horizontal (x) and vertical (y) positions and their derivatives ($dx/dz, dy/dz$) at the target position. In the present analysis, the initial momentum was set at 0.9 GeV/ c . In the local tracking in SFT-SDC2 and SDC3-SDC4, a straight track was assumed. However, there is a small effect of the fringing magnetic field of SKS. Therefore, in the SKS tracking the full tracking using the field map was performed by considering the fringing field. The track parameter optimization was repeated iteratively until the χ^2 reaches a convergence criteria. The convergence criterion in the iteration is $\delta\chi^2 = (\chi_{k+1}^2 - \chi_k^2)/\chi_k^2 < 10^{-3}$, where k is the number of iteration and χ_k^2 is the tracking χ^2 for the k -th iteration.

Figure 3.13 shows a typical χ^2 distribution in the SKS tracking. The χ^2 is selected less than 10.

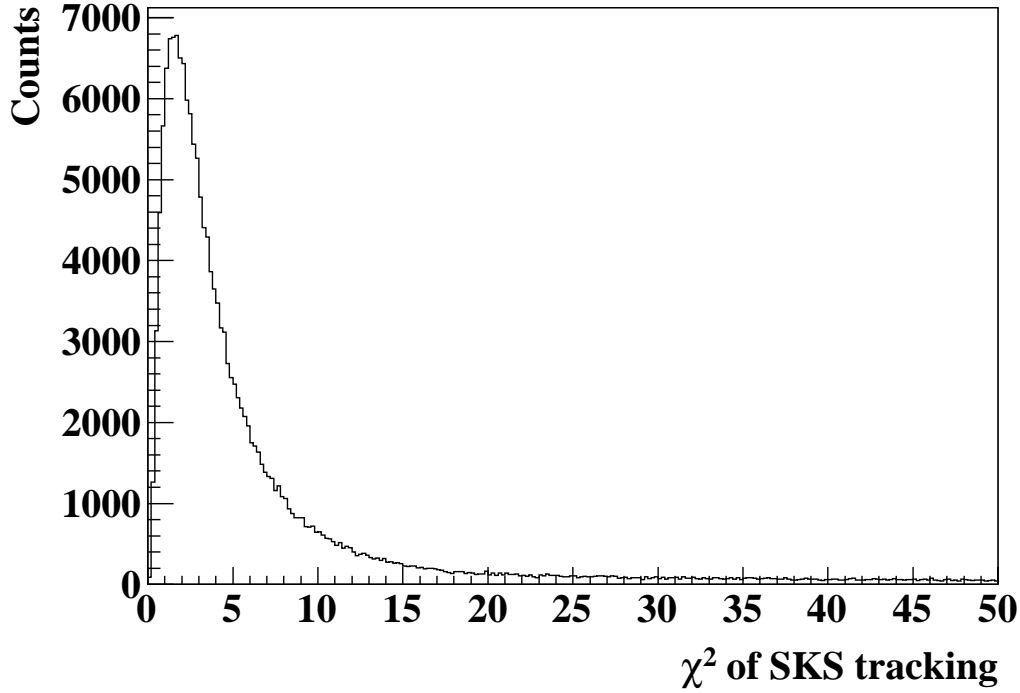


Figure 3.13: Typical χ^2 distribution of SKS tracking.

3.3.5 Particle identification in the SKS spectrometer

The PIK trigger cannot completely remove all the background. The background particles were fast protons which fired LC and were misidentified as kaons and pions which were not rejected by LAC due to its inefficiency. After the Runge-Kutta tracking, the mass of a scattered particle (M_{scat}) was finally obtained as

$$M_{scat} = \frac{p}{\beta} \sqrt{1 - \beta^2}, \quad (3.2)$$

where β is the velocity of a scattered particle obtained from the time-of-flight and the flight path length, and p is the momentum obtained from the SKS tracking. Figure 3.14 shows a typical mass squared spectrum for the ${}^6\text{Li}(\pi^-, K^+)$ reaction with $\chi_{sks}^2 < 10$ and $0.7 < p < 1.2$ GeV/ c cut. A tail in the low mass side of the proton distribution is miss use of timing information of BH2. Very high intensity beam causes accidental hits after the true start timing. If the accidental hit timing was used for the β calculation, it produce the slow component. Around the kaon region ($0.2 < m^2 < 0.3$) is overlapped the proton tail. Also a pion tail is overlapped because of the resolution of mass squared of pion. Since mass squared resolution depends on momentum, momentum dependent cut with 2σ of mass squared resolution is applied to select kaons as shown in Fig. 3.15.

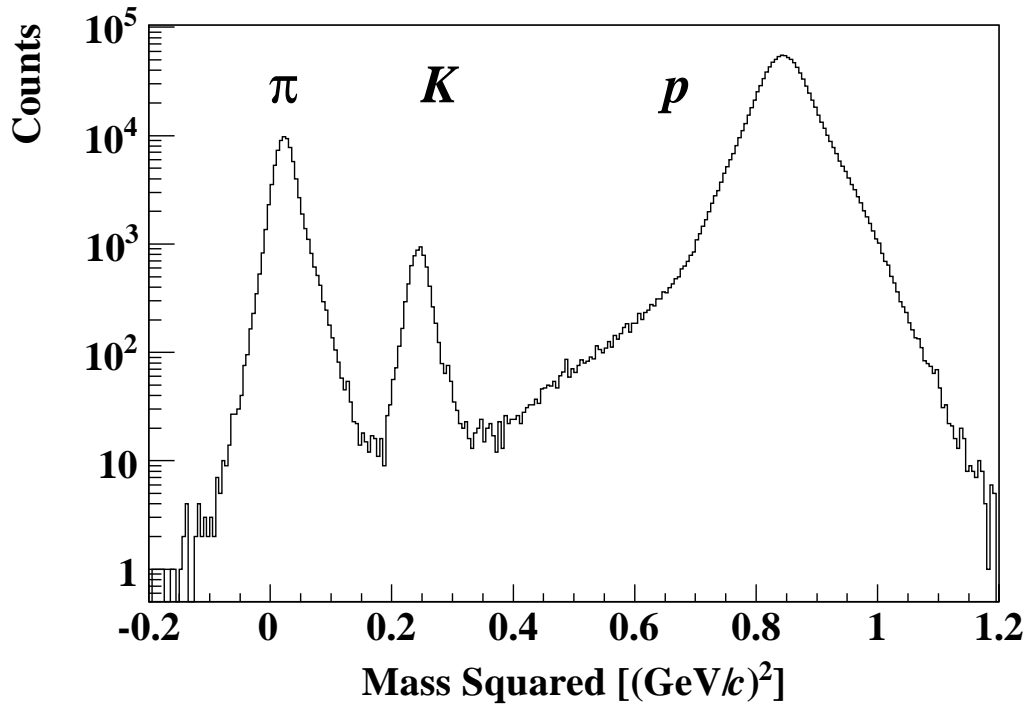


Figure 3.14: Scattered particle mass squared distribution for the ${}^6\text{Li}(\pi^-, K^+)$ data

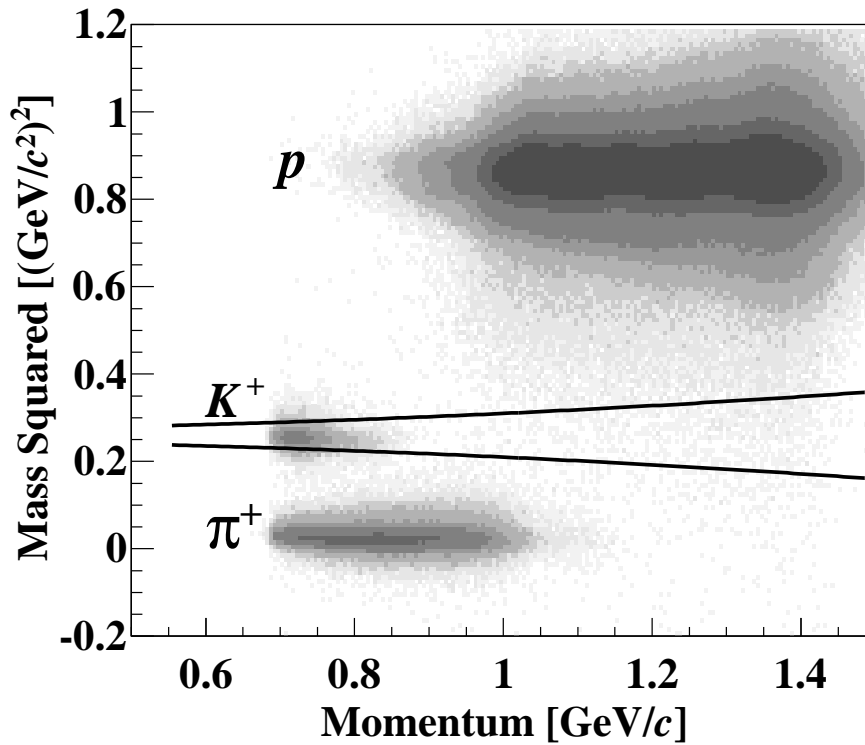


Figure 3.15: Mass squared vs. momentum plot of the scattered particles measured by the SKS spectrometer in the ${}^6\text{Li}(\pi^-, K^+)$ reaction. Two curves in the figure show the momentum dependent 2σ cut for the kaon selection.

3.4 Vertex reconstruction

The scattering angle and the vertex point were obtained from both incident beam and scattered particle trajectories which were obtained by the track reconstruction in the K1.8 beam line spectrometer and the SKS, respectively. Especially, incident beam track was corrected by using the SSD hit position. Since there was material of BH2 between the target and BC4, angle resolution and vertex resolution were worse because of the multiple scattering effect. Correction Step is as follows,

1. Calculate the hit position at BH2 by extrapolating the BC3-4 track.
2. Calculate the angle from hit position of BH2 and SSD.

Figure 3.16 shows a typical distribution of the horizontal (a) and vertical (b) scattering angle difference measured by both spectrometers for the beam-through data with the π^- of 0.9 GeV/ c in empty target data. We obtained the horizontal and vertical angular resolutions of 2.13 ± 0.01 mrad and 2.11 ± 0.01 mrad in σ , respectively.

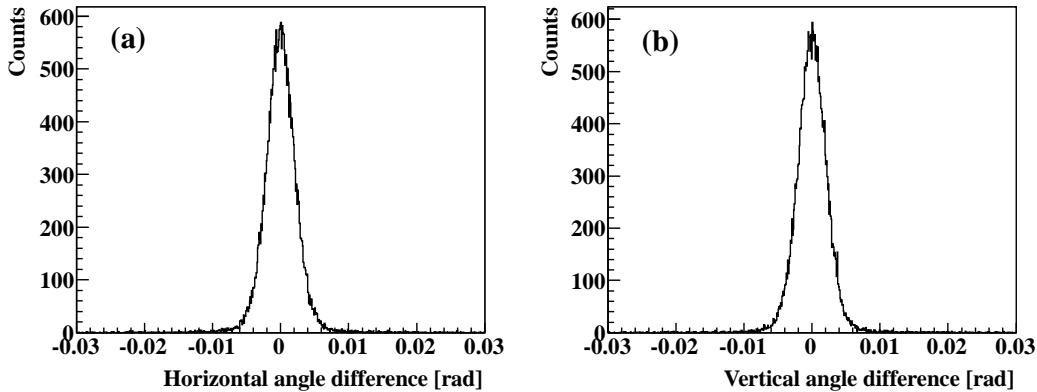


Figure 3.16: Typical distribution of the horizontal (a) and vertical (b) scattering angle difference measured by both spectrometers for the π^- of 0.9 GeV/ c in empty target data. The horizontal and vertical angular resolutions were 2.13 ± 0.01 mrad and 2.11 ± 0.01 mrad in rms, respectively.

The reaction vertex point was obtained from the closest distance between the tracks of beam pion and scattered kaon. Figure 3.17 shows a distribution of the vertex position and the closest distance for the ${}^6\text{Li}(\pi^-, K^+)$ production data, where z-axis was defined as the beam direction. The vertex cut region in z-direction is selected less than the real target length +20 mm, and in x- and y-direction is selected smaller than the real target size. The good vertex event is selected less than 5 mm in the closest distance.

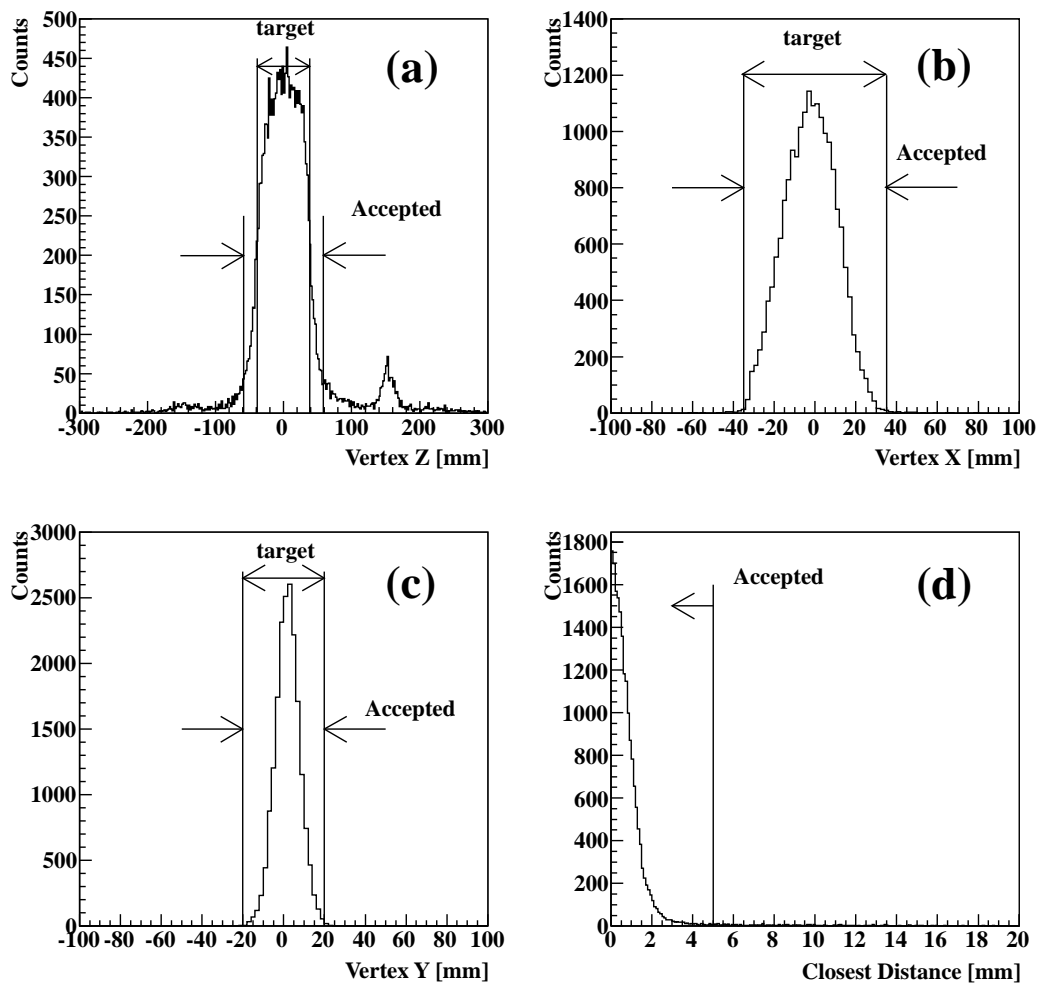


Figure 3.17: Distributions of vertexes and a closest distance. (a) shows a vertex distribution of z-direction, (b) shows that of x-direction and (c) shows that of y-direction. (d) shows a distribution of closest distance.

3.5 Analysis of the beam-through runs

The beam-through runs are taken in four momentum settings at 0.8, 0.9, 1.0 and 1.2 GeV/c. During the runs, the SKS magnet was set at the negative polarity of 2.16 T. Figure 3.18 shows a distribution of the difference of momenta between the beam line spectrometer and the SKS spectrometer at a momentum of +0.9 GeV/c.

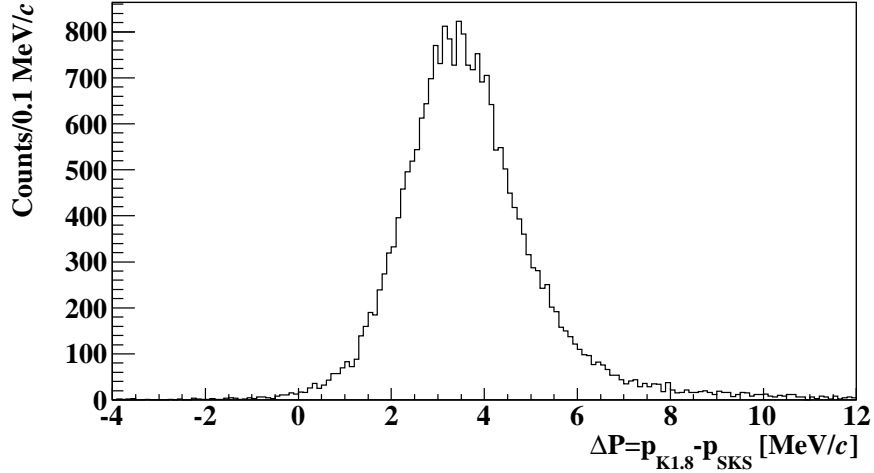


Figure 3.18: The momentum difference between the two spectrometers without any offset correction. The beam momentum setting was 0.9 GeV/c

Figure 3.19 shows the width of the distribution for the momentum difference between two spectrometers (Δp) as a function of the nominal central momentum of the beam line spectrometer. This width comes from the momentum resolution of the two spectrometers ($\sigma_{K1.8}$ and σ_{sks}) and is given as $\sigma_{\Delta p} = (\sigma_{SKS}^2 + \sigma_{K1.8}^2)^{\frac{1}{2}}$. The width is $\sim 0.2\%$ (FWHM) at 0.8 GeV/c, and proportionally increases as the momentum.

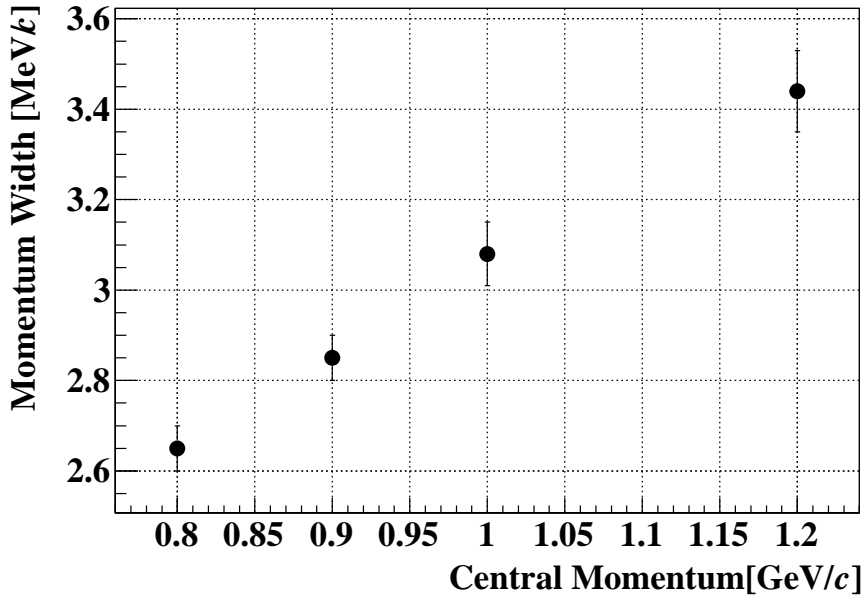


Figure 3.19: The width of the distribution for the momentum difference between the two spectrometers as a function of the central momentum of the beam line spectrometer.

3.6 Momentum correction

3.6.1 Overview

Momentum correction is taken into account for both incoming pion and outgoing kaon. At first, we consider the energy loss of the target and BH2. For beam pion momentum, since measured momentum is before BH2 and target, momentum is corrected at reaction vertex point.

3.6.2 Momentum correction of scattered particles

In the present experiment, the momentum of the scattered particles was reconstructed by using the calculated magnetic field map. However, the present magnetic field map does not completely reproduce the real magnetic field, especially, in fringing fields. This effect can be seen by checking the dependence of missing mass on scattering angle. Figure 3.20 shows a scatter plot between the missing-mass for the $p(\pi^\pm, K^+)\Sigma^\pm$ reaction and the derivatives of horizontal (dx/dz) or vertical (dy/dz) directions at the target point. The higher order correlation between the derivatives and the missing mass is seen in the figure (a, b).

To optimize the energy resolution, this correlation was corrected in the SKS momentum with the derivatives of the horizontal and vertical positions. For the correction, the momentum difference ($P_{calc} - P_{analyzed}$) was used. The analyzed momentum ($P_{analyzed}$) was obtained from the momentum reconstruction by the SKS tracking. This momentum should have some correlation with the derivatives. The calculated momentum (P_{calc}) was obtained from the calculation by the scattering angle and the beam momentum, where

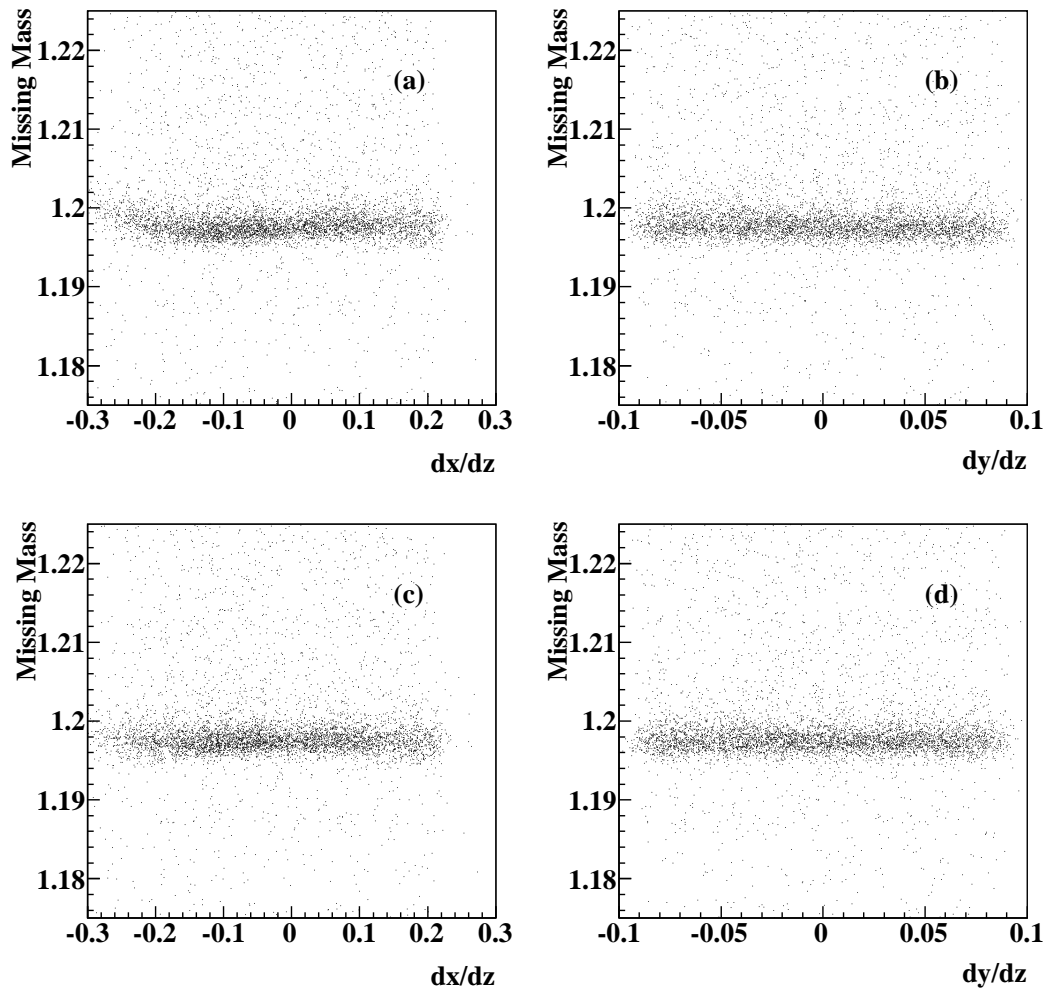


Figure 3.20: A scatter plot between the derivatives of horizontal (dx/dz) or vertical (dy/dz) positions at the target point and the Σ^- missing-mass. The figures after corrected for the correlation are shown in (c, d)

the kinematics of the $p(\pi^\pm, K^+)\Sigma^+$ reaction was assumed. This momentum has no correlation with the derivatives. Thus, the subtraction ($P_{calc} - P_{analyzed}$) has the information of the correlation. The correction for the SKS momentum was made with the 3rd-order poly-nominal in dx/dz and 2nd-order poly-nominal in dy/dz , respectively. In the same way, the SKS momentum was also corrected for the bound region in $^{12}\text{C}(\pi^+, K^+)_{\Lambda}^{12}\text{C}$ production.

3.6.3 Target energy loss and straggling

In order to examine the effects of the target energy loss and its straggling, π^+ beam-through data without and with a target were taken at 0.8, 0.9, 1.0 and 1.2 GeV/ c . As an example, Figure 3.21 shows a distribution of the momentum difference measured by the beam spectrometer and the SKS without(a) and with(b) the $(\text{CH}_2)_n$ target (3.4 g/cm^2) for a 0.9 GeV/ c π^+ beam. The energy loss was obtained as the shift of the centroid. The energy straggling was obtained from the difference of the widths. The results of energy loss and straggling are summarized in Table 3.3. The obtained values are consistent with Bethe-Bloch formula within 0.1 MeV, which is better enough as compared with missing-mass resolution. Therefore, the energy loss was corrected by using Bethe-Bloch formula for ${}^6_\Lambda\text{H}$, Σ^\pm , and ${}^{12}_\Lambda\text{C}$ production runs. Once the missing-mass is reconstructed, the event-by-event correction of the target energy loss was applied according to vertex position.

Table 3.3: target energy loss and stragglings

momentum (GeV/ c)	energy loss (MeV)	straggling FWHM(MeV)
0.8	6.48 ± 0.14	1.39 ± 0.23
0.9	6.47 ± 0.18	1.31 ± 0.24
1.0	6.92 ± 0.34	1.45 ± 0.22
1.2	7.08 ± 0.29	1.23 ± 0.18

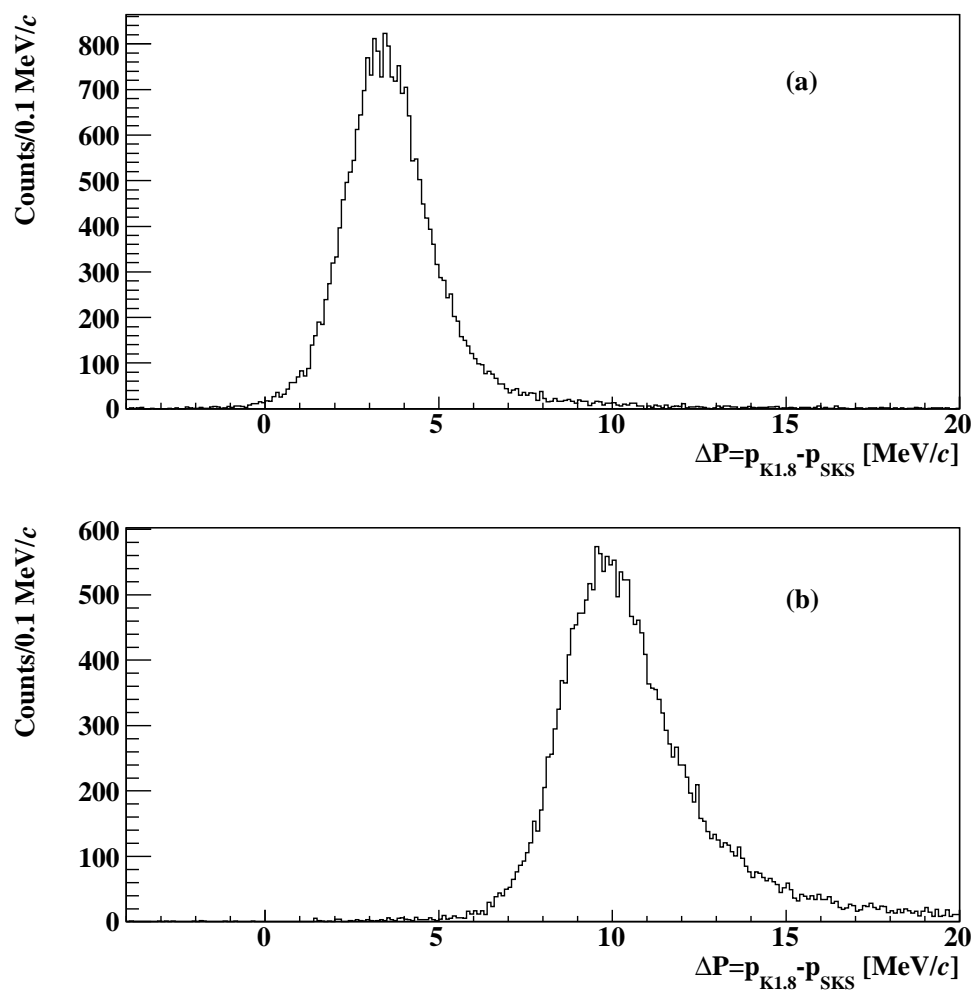


Figure 3.21: Distributions of the momentum difference between the two spectrometers without(a) and with(b) the $(CH_2)_n$ target (3.4 g/cm^2) for a $0.90 \text{ GeV}/c \pi^+$ beam. In (b), centroid is shifted and the width is widened because of the target energy loss and its straggling.

3.6.4 Momentum correction of beam pions

The momenta of particles measured in the K1.8 beam line spectrometer were corrected with a 1st-order poly-nominal function by considering the results of the beam-through run at 0.9 GeV/ c and $p(\pi^-, K^\pm)\Sigma^\pm$ runs at $p_\pi = 1.38$ GeV/ c . Since the SKS magnetic field is fixed in all runs, the momentum of scattered particle measured in the SKS spectrometer is not corrected (As mentioned in Sec 3.6.2, only scattering angle dependency was corrected). The momentum difference between K1.8 and SKS ($dp = p_{sks} - p_{K1.8}$) was measured -2.43 MeV/ c from the beam-through run at 0.9 GeV/ c by considering the energy loss of BH2. In the Σ^\pm production runs the mass difference of $\Sigma^+(\Sigma^-)$ ($M_{measure-\Sigma} - M_{PDG-\Sigma}$) was found to be +1.18 MeV/ c^2 (+0.28 MeV/ c^2). A momentum offset of +1.74 MeV/ c is estimated from the deviation of the measured Σ^+ mass at 1.38 GeV/ c from the PDG value. The effect of the beam polarity change from π^+ to π^- is estimated to be -1.30 MeV/ c from the peak positions of Σ^+ and Σ^- in the missing-mass spectra. After all, the beam momentum was corrected with a 1st-order poly-nominal function of the measured beam momentum ($p_{K1.8}^-$) as follows,

$$p_{corrK1.8}^- = 1.0087p_{K1.8}^- - 0.0103 - 0.0013$$

where, $p_{corrK1.8}^-$ is the corrected momentum for the negative pion beam in a unit of GeV/ c . In the case of 1.2 GeV/ c beam momentum used in the ${}^6\text{Li}(\pi^-, K^+)$ reaction, the amount of correction is -1.2 MeV/ c . Figure 3.22 shows momentum difference for each beam momentum and correction fuction of the beam momentum. The systematical uncertainty of the beam momentum is estimated to be ± 1.32 MeV/ c from the momentum deviations in other beam-through runs at 0.8, 1.0, 1.2 GeV/ c .

Table 3.4: momentum correction

run	$p_{K1.8}$ (GeV/ c)	$p_{corrK1.8}$ (GeV/ c)	dp (MeV/ c)
Beam Through	0.90001 ± 0.0004	0.89758 ± 0.0004	-2.43 ± 0.06
Σ^+	1.37710 ± 0.0005	1.37884 ± 0.0004	$+1.74 \pm 0.12$
Σ^-	1.38220 ± 0.0005	1.38262 ± 0.0005	$+0.44 \pm 0.11$

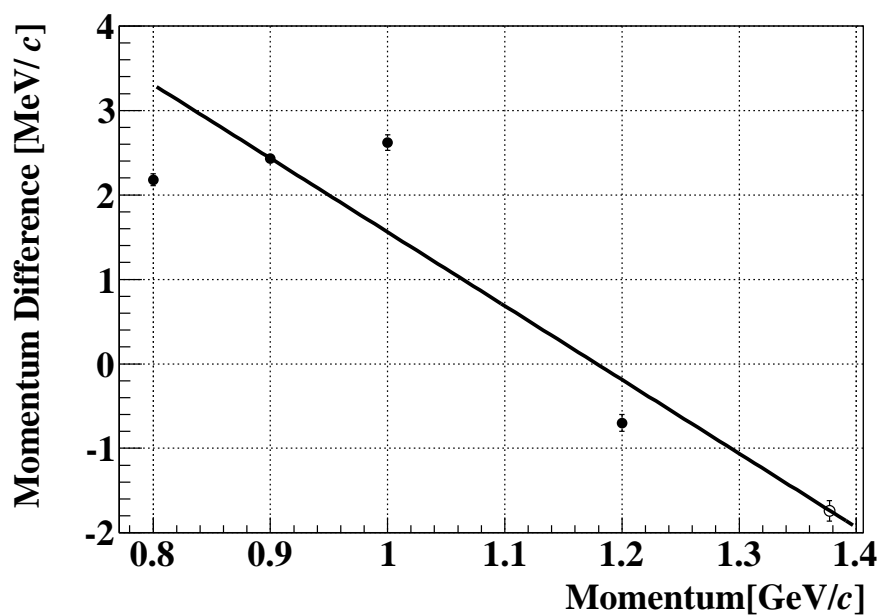


Figure 3.22: Momentum difference measured with the K1.8 beam line and the SKS. Filled circles represent beam through runs at beam momenta of 0.8, 0.9, 1.0 and 1.2 GeV/c. Open circle represents momentum difference of the Σ^+ production run, where expected beam momentum is estimated with the mass difference from PDG value of Σ^+ .

Chapter 4

Experimental results

4.1 Good (π^- , K^+) events

Good (π , K) events are selected as shown in an analysis flow chart in Fig. 4.1. In hodoscope analysis, the number of hits of BH2 within 2 ns of the time window is required to be only one hit, and the number of hits of TOF is required to be one hit as well within 100 ns of time window. Furthermore, large ADC value of TOF is rejected as proton like events. In BFT analysis, hit clusters of BFT are selected within 6 ns of the time window. The number of clusters are not limited at this time. In BC3 and BC4 tracking, χ^2 was required to be less than 30. Hit consistency of hit position between the track and the BH2 hit segment was checked. After the selection, we carry out the K1.8 tracking and reconstruct the beam momentum. The number of K1.8 track candidates were $N_{BFT} \times N_{BC34tracks}$. As shown in Fig. 3.10, K1.8 tracks were selected with BFT XU and YV correlation cuts. After this cut, the number of K1.8 tracks is required to be one.

In SFT-SDC2 and SDC3-SDC4 tracking, χ^2 was required to be less than 30 and 20, respectively. If these are satisfied, SKS tracking is carried out by using a Runge-Kutta method. χ^2 of SKS tracks are selected to be less than 10. Scattered kaons are selected within the mass squared resolution of $\pm 2\sigma$. After this selection, the number of SKS tracks is required to be one. In order to suppress accidental K1.8 tracks, the vertex analysis including the SSD is performed. To increase the S/N ratios, the number of hits of SSD selected to be one. After corrected the K1.8 track by SSD, vertex position is calculated. Good (π , K) reaction events were selected in the criteria that closest distance is less than 5 mm and vertex position is within the real size +20 mm in the z-direction and real size in the x- and y-directions. The efficiency of each analysis procedure is described in Chap 4.2.

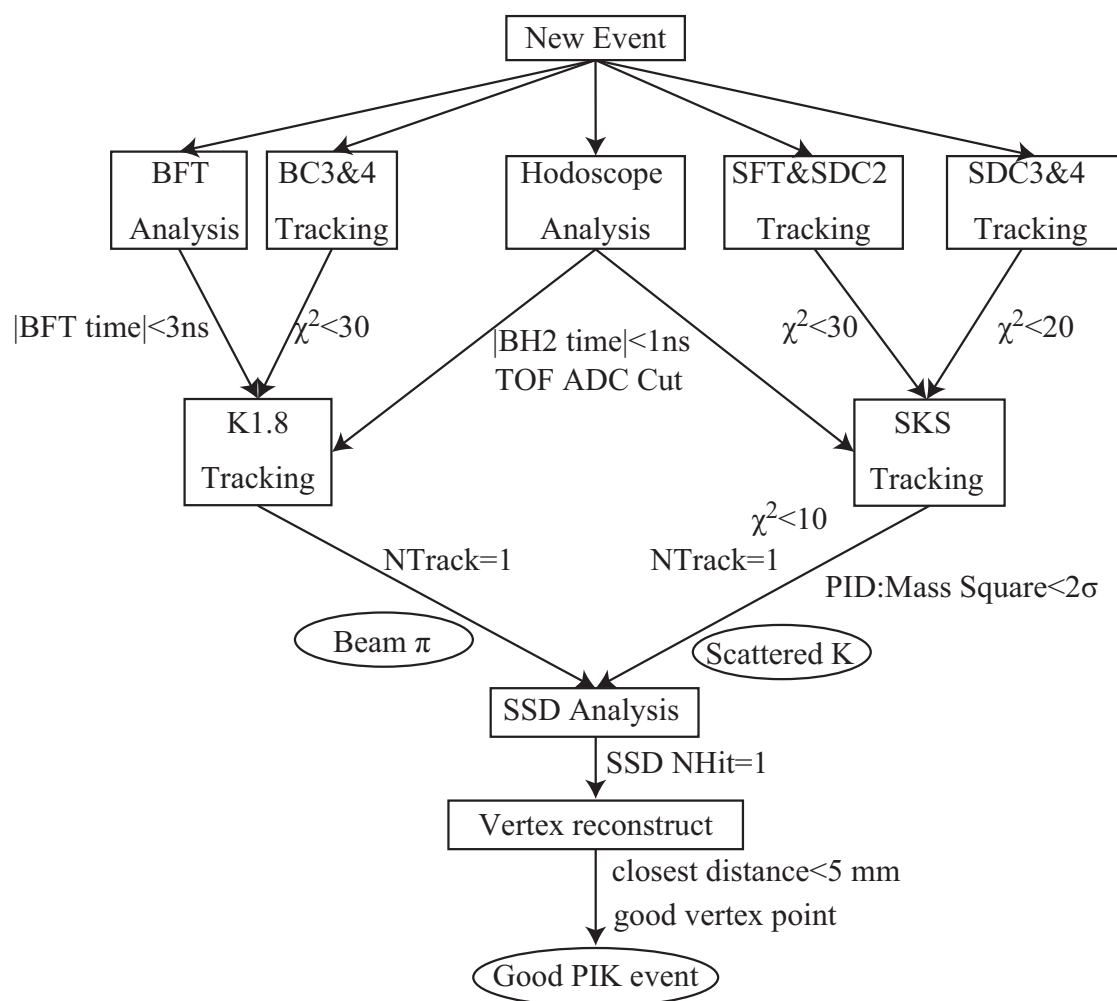


Figure 4.1: Flow chart of the offline analysis. The order of the analysis is shown in each box.

4.2 Cross Section

The cross section was obtained from the experimental yield N_K of the good (π^- , K^+) events as

$$\left(\frac{d\sigma}{d\Omega}\right) = \frac{A}{(\rho x) \cdot N_{Avo}} \cdot \frac{1}{(N_{beam} \cdot f_{beam} \cdot \epsilon_{K1.8})} \cdot \frac{N_K}{\epsilon_{SKS} \cdot \Delta\Omega} \cdot \frac{1}{(\epsilon_{\pi K} \cdot \epsilon_{daq})},$$

$$\epsilon_{K1.8} = \epsilon_{BFT} \cdot \epsilon_{BC3.4} \cdot \epsilon_{K1.8track},$$

$$\epsilon_{SKS} = \epsilon_{TOF} \cdot \epsilon_{LC} \cdot f_{AC} \cdot \epsilon_{SFT.SDC2} \cdot \epsilon_{SDC3.4} \cdot \epsilon_{SKStrack} \cdot \epsilon_{PID} \cdot f_{decay} \cdot f_{abs},$$

$$\epsilon_{\pi K} = \epsilon_{SSD} \cdot \epsilon_{closeDist} \cdot \epsilon_{single-\pi K} \cdot \epsilon_{vertex},$$

where A is the target mass number ($A=6$ in ${}^6\text{Li}$, $A=7$ in proton in the $(\text{CH}_2)_n$ and $A=12$ in graphite), ρx is the target thickness in g/cm^2 , N_{Avo} is the Avogadro's number, N_{Beam} is the number of the total beam particles measured as the scaler counts of the sum of each BH2 segments. $\Delta\Omega$ is the effective solid angle of the SKS. ϵ 's and f 's are the experimental efficiency factors. The factors represent the detector and analysis efficiencies, the data acquisition efficiency, the muon contamination effects in the beam, the K decay effects, and the K absorption effects, where symbols are defined in Table 4.1. The precision of

Table 4.1: The list of the experimental efficiency factors.

Factors	Meaning	Values (%)
ϵ_{daq}	Data-acquisition efficiency	77.6 ± 0.8
ϵ_{BFT}	BFT efficiency	97.6 ± 0.2
$\epsilon_{SFT.SDC2}$	SFT·SDC2 tracking efficiency	92.0 ± 0.6
$\epsilon_{BC3.4}$	BC3·4 tracking efficiency	99.4 ± 0.1
$\epsilon_{K1.8track}$	K1.8 tracking efficiency	96.4 ± 0.3
ϵ_{TOF}	TOF efficiency	99.9 ± 0.1
ϵ_{LC}	LC efficiency	97.8 ± 0.3
f_{LAC}	LAC accidental veto factor	88.0 ± 1.5
$\epsilon_{SDC3.4}$	SDC3·4 tracking efficiency	98.4 ± 0.2
$\epsilon_{SKStrack}$	SKS tracking efficiency	90.2 ± 0.3
ϵ_{SSD}	SSD efficiency	96.1 ± 0.5
ϵ_{PID}	PID efficiency in SKS	95.4 ± 0.2
$\epsilon_{single-\pi K}$	single track ratio	52.1 ± 1.2
$\epsilon_{closeDist}$	closest distance cut efficiency	97.1 ± 0.2
f_{abs}	K^+ absorption factor	95.6 ± 0.5
ϵ_{vertex}	Event vertex cut efficiency	94.8 ± 0.5

the cross section is determined by those of ρx , $\Delta\Omega$ and efficiency factors. The acceptance of the SKS was calculated with a Monte Carlo simulation. Each efficiency factor was estimated with various calibration data or Monte Carlo simulations. In this section, we discuss how they were obtained, and finally we estimate the total systematic error of the cross section.

4.2.1 Efficiency

Several efficiencies and correction factors are mainly the averaged values during the ${}^6\text{Li}(\pi^-, K^+)$ production runs. The error is determined from the root mean squares of the efficiency fluctuation of all runs.

Data acquisition efficiency

The data acquisition efficiency (ϵ_{DAQ}), caused by the dead time of the data acquisition system, was obtained as a ratio of the number of events 1st-level trigger accepted by the data acquisition system to that of the generated triggers. ϵ_{DAQ} was obtained as a function of the trigger rate, and a typical value of ϵ_{DAQ} was $77.6 \pm 0.8\%$ at a trigger rate of about 2200/2.0 sec per spill. The large error comes from difference of the intensity in December 2012 (12 MHz/spill) and January 2013 (14 MHz/spill).

Beam normalization factor

The beam normalization factor (f_{beam}) represents the fraction of pions in N_{beam} . N_{beam} includes electrons and muons because the scaler of BH2 did not require the GC veto. The fraction of electron contamination (f_e) is estimated from the coincidence of GC and BH2. At the high intensity beam, GC signal was saturated at more than 1 MHz due to only one phototube equipped with GC. Electron contamination was evaluated with the low intensity primary proton beam with the same slit condition as in the production runs because the electron contamination also depends on the slit condition. As a result, the electron contamination of the beam was found to be 10%. The contamination of muons is caused from two sources, those delivered from the upstream of the mass slit and those from the $\pi \rightarrow \mu$ decay between the mass slit (MS2) and BH2.

The muons coming from upstream of MS2 is simulated with Decay TURTLE code [59], and estimated to be 0.5%. The Decay TURTLE takes care of the properties of beam, such as the beam profile and the number of beam particles, at each beam line component. For the Decay TURTLE calculation, the profile of the incident beam generated from the T1 target and the properties of the beam line components were parametrized as the input file. For example, the properties of a dipole magnet, such as the aperture, the effective length of the central track, the field strength and gradient, were the inputs. The particle trajectories were simulated with the transfer matrix constructed by the input parameters of the beam line magnets, while in the electrostatic separators, the trajectories were calculated by using the Runge-Kutta calculation method. The trajectories which stopped at the several slits or went out side of the magnet aperture were rejected.

The muons coming from the $\pi \rightarrow \mu$ decay between MS2 and BH2 were estimated from y-direction distribution at BFT. In the K1.8 tracking, after calculating the δ value, y , dx/dz and dy/dz at BFT are obtained from δ . When the y and dy/dz distribution is out of the BFT effective area, we treat it as from the decay muon. Therefore, this factor includes K1.8 tracking efficiency.

In total, the value of $f_{beam} \equiv (1 - f_\mu)(1 - f_e)$ was estimated to be $89.5 \pm 5.0\%$. The reason of the large error is caused the electron contamination factor, f_e . In the present data, according to the primary beam intensity, the ratio of the electron contamination

varied in spite of slit is fixed. In principle, the ratio should be constant even if the primary beam intensity change. Since we don't understand this phenomena completely, we put this change systematic error.

BFT efficiency

In order to obtain the BFT efficiency, we used the BEAM trigger events mixed in the (π, K) data. The BFT efficiency was defined as

$$\epsilon_{BFT} = \frac{N(Hit_{BFT} \times \pi Beam)}{N(\pi Beam)},$$

where $N(\pi Beam)$ is the number of events of the BH2 trigger data, and $N(Hit_{BFT} \times \pi Beam)$ the number of good BFT hits found in the proper BEAM trigger data. The good BFT hits is selected by the ± 3 ns time window. The efficiency is an average value during the ${}^6_\Lambda\text{H}$ production runs.

BC3-BC4 tracking efficiency

The BC3-BC4 tracking efficiency is defined as

$$\epsilon_{BC3-4} = \frac{N(Track_{BcOut} \times \pi Beam)}{N(\pi Beam)}.$$

It was the total efficiency including the detection efficiency and the analysis efficiency to find a good straight track. Due to very high intensity beam, we applied "BH2 Filter" method which put a limitation on the hit candidate search area by using BH2 hit segment information. The BC3-BC4 efficiency is estimated to be $99.4 \pm 0.1\%$.

SSD efficiency

The SSD efficiency is defined as

$$\epsilon_{SSD} = \frac{N(Hit_{SSD} \times Track_{BcOut} \times BEAM)}{N(Track_{BcOut} \times BEAM)}.$$

The $N(Track_{BcOut} \times BEAM)$ requires the extrapolated hit position at SSD estimated from the BC3-BC4 track is in the effective area of SSD. The SSD efficiency is estimated to be $96.1 \pm 0.5\%$.

K1.8 tracking efficiency

The K1.8 tracking efficiency ($\epsilon_{K1.8track}$) was the analysis efficiency to reconstruct a particle trajectory in the beam spectrometer defined as

$$\epsilon_{K1.8track} = \frac{N(K18track \times BFTHit = 1 \times BC3 \cdot 4track = 1)}{N(BFTHit = 1 \times BC3 \cdot 4track = 1)}$$

where $N(BFTHit = 1 \times BC3 \cdot 4track = 1)$ was the number of single good track found in the BFT time cut ($|\text{time}| < 3$ ns) and BC3 and BC4 local tracking ($\chi^2 < 30$), and $N(K18track \times BFTHit = 1 \times BC3 \cdot 4track = 1)$ is the number of good K1.8 track found in the single good tracks of both BFT Hit and BC3 and BC4 local tracking requiring the xu and yv cut in Fig 3.10. It was found to be $96.4 \pm 0.3\%$. This value includes the decay muon comes from downstream of the MS2.

TOF and LC efficiency

The detection efficiency of TOF and LC was estimated from the beam-through run with BEAM trigger. The TOF and LC efficiency was obtained as

$$\epsilon_{TOF} = \frac{N(TOFHits \times SdcOutTrack > 0 \times LCHits > 0 \times AcHits)}{N(SdcOutTrack > 0 \times LCHits > 0 \times AcHits)},$$

$$\epsilon_{LC} = \frac{N(LCHits \times SdcOutTrack > 0 \times TOFHits > 0 \times AcHits)}{N(SdcOutTrack > 0 \times TOFHits > 0 \times AcHits)},$$

where $N(SdcOutTrack > 0 \times TOFHits > 0 \times AcHits)$ is the number of π tracks which should pass through the effective area of TOF selected by the TDC information of LAC and LC, and $N(TOFHits \times SdcOutTrack > 0 \times LCHits > 0 \times AcHits)$ is the number of those π tracks detected by TOF. LC is the same situation as TOF. The momentum range of π is in $0.8 - 1.0$ GeV/ c . The efficiency of TOF and LC are found to be $\epsilon_{TOF} = 99.9 \pm 0.1\%$ and $\epsilon_{LC} = 97.1 \pm 0.2\%$, respectively. In LC efficiency, the μ events from the pion decay after passing through TOF was included in the efficiency. The efficiency was assumed to be the same for K because the light yield of Čerenkov photons by K in the momentum range from 0.8 to 1.0 GeV/ c was high enough than the discriminator threshold.

Accidental veto factor of LAC

The accidental veto factor of LAC was estimated from the special (π, π) trigger data in which the information of LAC was not required. For the estimation, we used scattered proton events which should not be detected by LAC. The LAC accidental veto factor was obtained from

$$f_{AC} = 1 - \frac{N(AC \times Proton)}{N(Proton)},$$

where $N(Proton)$ is the number proton track which should pass through the effective area of LAC. Figure 4.2 shows the TDC spectrum of proton event in the (π, K) trigger. We estimated the efficiencies with the three cut criteria, loose cut (40 ns), normal cut (30 ns) and tight cut (20 ns).

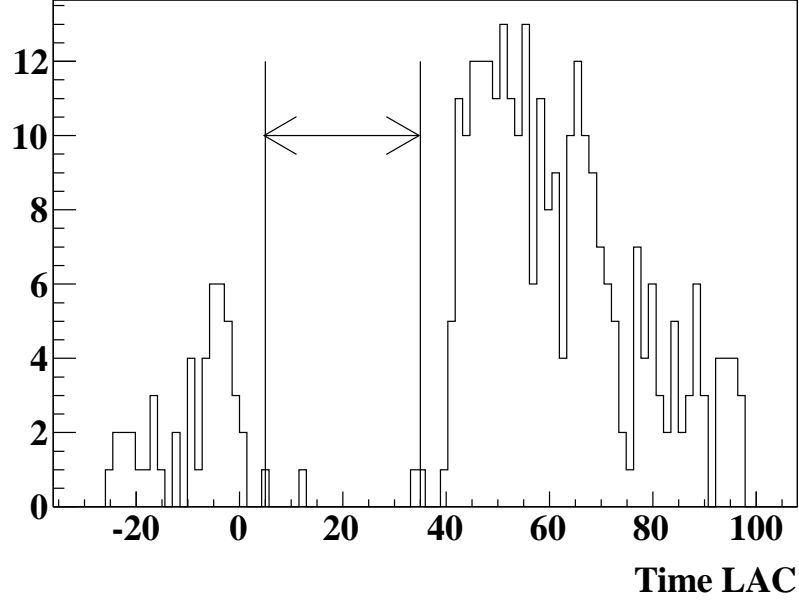


Figure 4.2: Time distribution of LAC in proton event in the (π, K) trigger.

SFT and SDC2 tracking efficiency

The efficiency of SFT and SDC2 tracking ($\epsilon_{SFT.SDC2}$) is the total efficiency including the detector efficiency and the analysis efficiency to find straight tracks at the entrance of the SKS magnet. It was estimated by the same way as that of BC3 and BC4 by using the *BEAM* trigger events mixed in the (π, K) data. It was found to be $92.0 \pm 0.6\%$. Since the efficiency is not affected for a small energy-loss difference between pion and kaon, we assumed the efficiency is the same for K . The SFT and SDC2 local tracking efficiency is the average value during the ${}^6_\Lambda\text{H}$ production run.

SDC3 and SDC4 efficiency

The efficiency of SDC3 and SDC4 ($\epsilon_{SDC3.4}$) is the total efficiency including the detector efficiency and the analysis efficiency to find straight tracks at the exit of the SKS magnet. We estimated the efficiency using scattered proton events recorded in the PIK trigger data (the $(\pi, p)X$ events) in which the particle does not decay in flight. Figure 4.3 shows the scatter plot between the horizontal scattering angle measured by SFT and SDC2 local tracking and the flight time between BH2 and TOF. The proton events were selected as shown in the figure. The SDC3 and SDC4 efficiency was estimated from the number of those selected proton events ($N(Proton)$) as

$$\epsilon_{SDC3.4} = \frac{N(SDC3.4Track \times Proton)}{N(Proton)},$$

where $N(SDC3.4Track \times Proton)$ was the number of good tracks of these proton events found in the SDC3 and SDC4 ($\chi^2 < 20$) local tracking. It was found to be $98.4 \pm 0.2\%$ which was the average of typical runs whose event number was statistically large enough

during the Σ production run. The error was determined from the root mean squares of the efficiency fluctuation for each run.

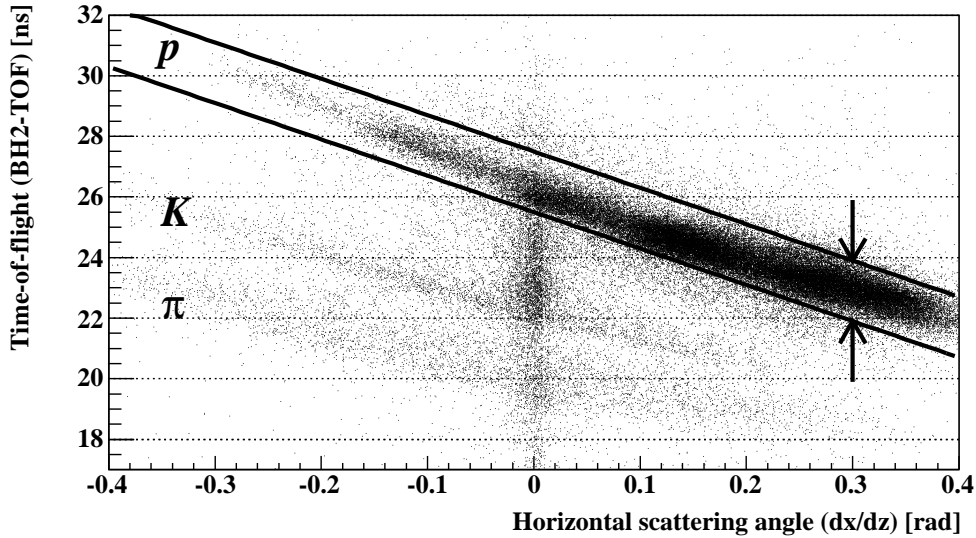


Figure 4.3: The correlation of time-of-flight and scattering angle (dx/dz).

SKS tracking efficiency

The SKS tracking efficiency $\epsilon_{SKS\text{Track}}$ was estimated by using the $(\pi, p)X$ events recorded in the PIK trigger because the proton does not decay in flight. It is obtained as

$$\epsilon_{SKS\text{Track}} = \frac{N(SKSTrack \times SdcInTrack = 1 \times SdcOutTrack = 1 \times Proton)}{N(SdcInTrack = 1 \times SdcOutTrack = 1 \times Proton)},$$

where $N(SdcInTrack = 1 \times SdcOutTrack = 1 \times Proton)$ was the number of single good tracks of proton events found in the SFT and SDC2 ($\chi^2 < 30$) and SDC3 and SDC4 ($\chi^2 < 30$) local tracking, and $N(SKSTrack \times SdcInTrack = 1 \times SdcOutTrack = 1 \times Proton)$ is the number of good SKS track found in the single good tracks of both SFT-SDC2 and SDC3-SDC4 local tracking.

Figure 4.4 shows the efficiency as a function of the scattering angle. The SKS tracking efficiency for each angle (θ_{sks}) was estimated as a ratio of the number of events accepted as a good trajectory within the selected scattering angle region by the tracking analysis to the number of events which have good straight tracks within the selected scattering angle calculated by SFT-SDC2 trajectory ($\theta_{SFT.SDC2}$). The scattering angle ($\theta_{SFT.SDC2}$) was calculated by using the horizontal and vertical angles measured by SFT-SDC2 tracking. Good straight tracks at both of the entrance and exit of SKS were also required. The efficiency for the scattering angle larger than 17 degrees was rapidly worse because the magnetic field was not reproduced well in the fringing field region, namely the region near the pole edge and the coil of the SKS magnet.

Figure 4.5 shows the missing mass resolution of Σ^- as a function of the χ^2_{SKS} . It was found that the events whose the χ^2_{SKS} is less than 10 kept the missing mass resolution

of less than $2.5 \text{ MeV}/c^2$ (FWHM). We took into account of tight cut to $\chi_{SKS}^2 < 10$ to keep good missing mass resolution.

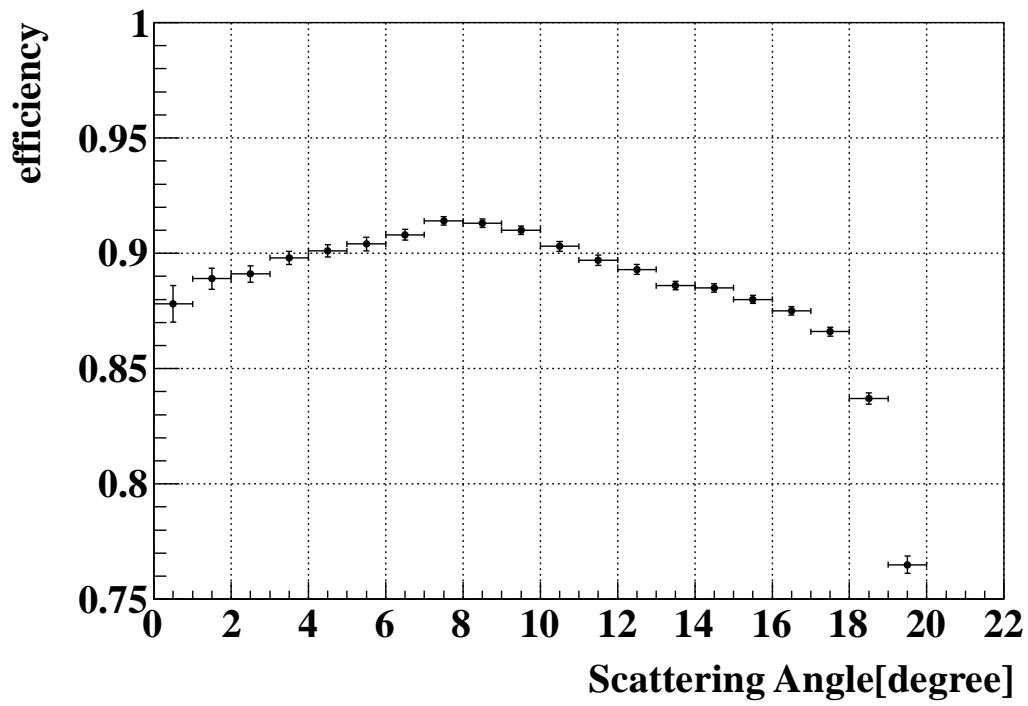


Figure 4.4: The SKS tracking efficiency as a function of the scattering angle.

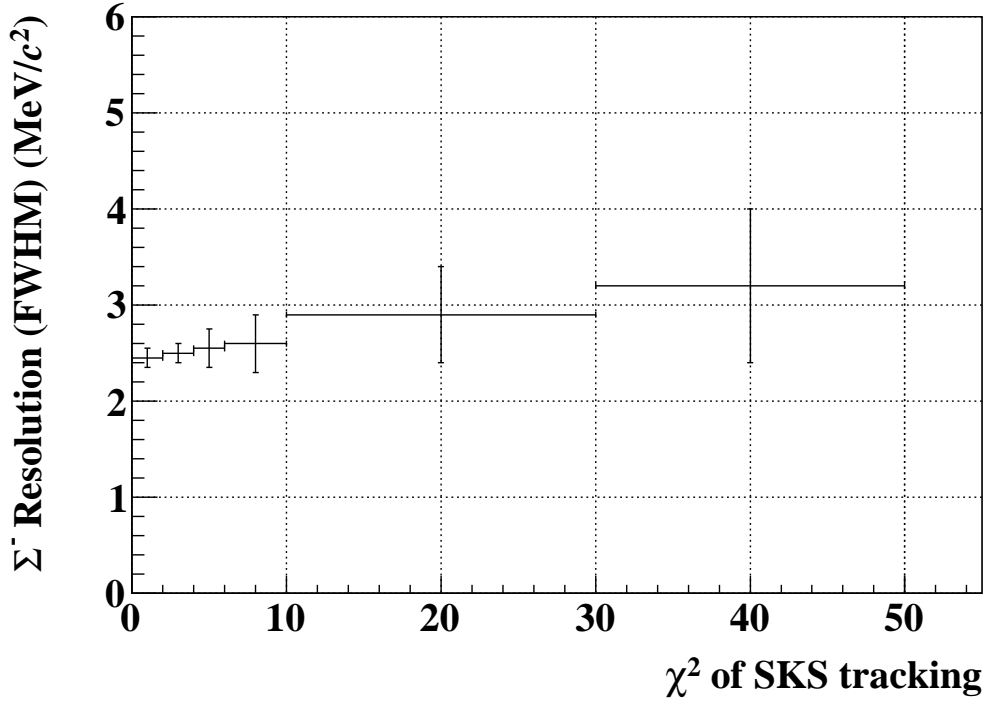


Figure 4.5: The missing-mass resolution of Σ^- as a function of the χ^2_{sks}

Scattered particle identification efficiency

As shown in Fig. 3.14, mass squared is calculated by β and momentum of scattered particles. To select the scattered kaons, we applied the momentum dependent cut for the mass squared because the mass squared resolution depends on the momentum.

As shown in Fig. 3.15, the correlation of the mass squared and the momentum after selecting the $\chi^2_{sks} < 10$. We selected kaons by a momentum dependent cut at $\pm 2\sigma$ of the mass squared resolution as indicated with curves in the figure. The contamination of protons in the K^+ cut region is less than 1% below the particle momentum of 1.1 GeV/c. The efficiency of particle identification was $93.8 \pm 0.2\%$.

Single PIK track efficiency

The number of PIK track is defined as

$$N(PIKtrack) = N(K1.8track) \times N(SKStrack) \times N(SSDHit).$$

Therefore, single PIK track is defined as,

$$\epsilon_{single-\pi k} = \frac{N(PIKtrack = 1)}{N(PIKtrack > 0)}$$

Figure 4.6 shows the number of PIK tracks. The single PIK track efficiency is estimated to be $52.1 \pm 1.2\%$. The reason of lower efficiency is mainly due to high multiplicity in SSD. The single hit(track) ratio of K1.8 track, SKS track and SSD hit were 85.1%, 92.1% and 66.5%, respectively. Most of the high multiplicity hits of SSD were due to accidental hits

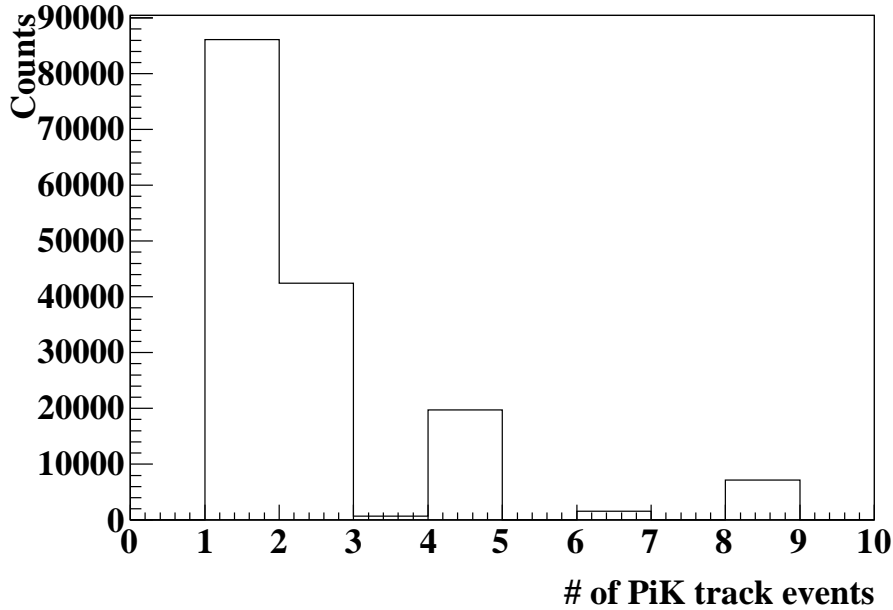


Figure 4.6: The number of PIK tracks candidates.

Vertex cut efficiency

As mentioned in Sec. 3.4, the vertex cut was applied to select good (π, K) events from the target region. The vertex resolution for very forward scattering angle events was worse than the other angular events as shown in Fig. 3.17. Therefore, we estimated the vertex efficiency as a function of scattering angle. A vertex cut region in the z-direction was selected a wider vertex region than the real target size +20 mm and in the x- and y-direction was selected real target size. Figure 4.7 shows the vertex efficiency with each steps of scattering angle. The efficiency (ϵ_{vertex}) was lower at the small angles, and was obtained to be $94.8 \pm 0.5\%$ in average for 2° – 14° . Figure 4.8 shows a scatter plot between the scattering angle and z-vertex distribution. As shown in the figure, the reconstruction of the z-vertex for very forward scattering angles failed because of difficulty to obtain the closest distance between forward track of the beam pion and the scattered kaon. For the scattering angle less than 2° , in particular the z-vertex resolution was too bad to eliminate the contribution of SSD.

K decay factor

Since the $\beta\gamma c\tau$ of kaon around the momentum of 0.8–0.9 GeV/ c is 6.0–6.8 m, a part of the kaons produced in the target decay before they reach the SKS downstream detectors. The survival rate in the SKS track reconstruction process was estimated from the production data event by event. The flight path length from the target to LAC was 4.6 m in average. From this value, averaged K decay factor is estimated to be $43.7 \pm 0.7\%$.

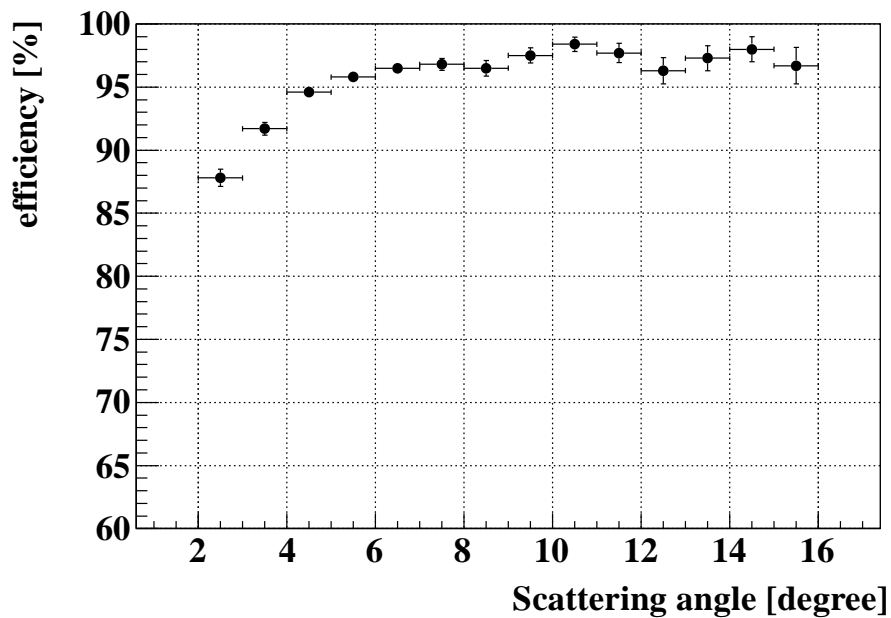


Figure 4.7: Vertex reconstruction efficiency as a function of the scattering angle.

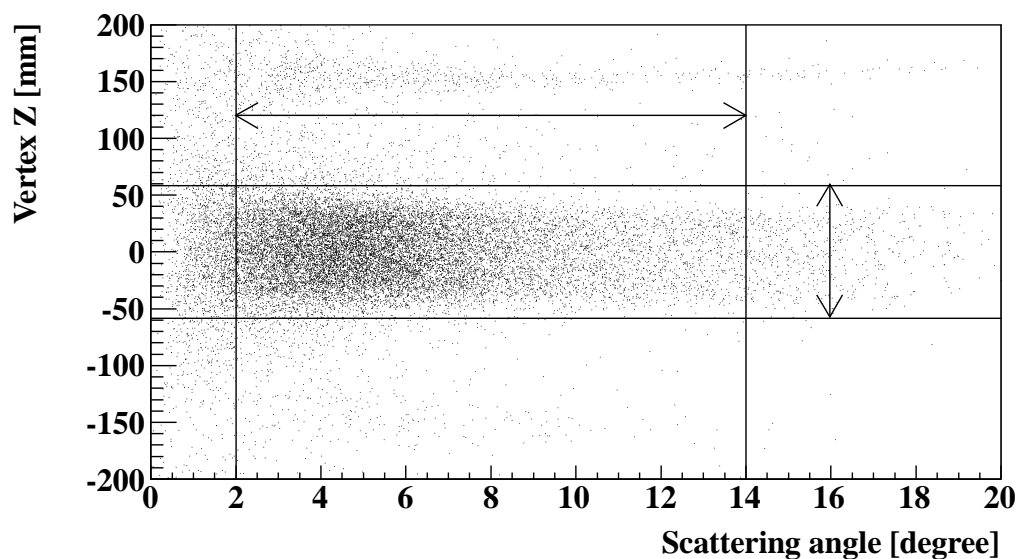


Figure 4.8: Scatter plot between the scattering angle and z-vertex distribution for the (π^-, K^+) data.

K absorption factor

Some of the kaons produced in the target would interact with materials in the spectrometers along the flight path. The K^+N inelastic cross section around 0.85 GeV/ c is about 2.0 mb. The absorption rate (f_{abs}) was estimated by a simulation, in which the target, the counters, the drift chamber gas and windows, the helium bags and air between the detectors were considered as materials in the spectrometer as shown in Table 4.2. Along the path of the scattered kaons, the TOF (3.10 g/cm²) and LAC (2.26 g/cm²) was dominant, while the total material thickness was about 10 g/cm². We took into account both inelastic and elastic interactions in the simulation. The K events were generated at the target with a uniform momentum distribution (0.75–0.95 GeV/ c), a uniform angular distribution ($\theta < 20^\circ$) and a reaction rate (f_{abs}) of the kaon was estimated as

$$f_{abs} = 1 - \frac{N_{KhitonLC}}{N_{Kgenerated}}.$$

The rate was estimated to be $4.4 \pm 0.3\%$. The error was estimated by the difference of the material thickness along the particle trajectories.

Table 4.2: Typical materials in the spectrometers along the flight path.

Material	Thickness (g/cm ²)
Target	3.50
TOF	3.10
LAC	2.26
AC frame (Al)	0.54

4.3 Acceptance of SKS

The effective solid angle of the SKS ($\Delta\Omega$) was calculated with a simulation. For a fixed interval of the scattering angle of $\Delta\theta$, the effective solid angle was calculated as a function of scattering angle θ and momentum p . In the event generation, the distribution of the beam profile defined as a function of (x_b, y_b, u_b, v_b) was produced from the experimental data, where x_b, y_b, u_b and v_b are the horizontal and vertical positions and their derivatives of a beam particle at the target. The scattered kaons were generated uniformly in polar angle θ ($\cos(\theta - \frac{1}{2}\Delta\theta) < \cos\theta < \cos(\theta + \frac{1}{2}\Delta\theta)$), uniformly in azimuthal angle ϕ ($0 < \phi < 2\pi$) and uniformly momentum p ($p - \frac{1}{2}\Delta p < p < p + \frac{1}{2}\Delta p$).

In the simulation, the combination of the TOF and LC counters used in the matrix trigger was also taken into account. In the present analysis, we selected events in the scattering angle from 2° to 14° . Therefore, the effective solid angle was calculated for $2^\circ < \theta < 14^\circ$.

Figure 4.9 shows the acceptance of SKS in the 2.2 T mode. It includes the matrix of TOF and LC combinations. The acceptance is represented by the arbitrary unit (number of triggered event in the simulation).

The momentum region of the scattered particle of 0.85–0.90 GeV/ c corresponds to the bound region of the ${}^6_\Lambda\text{H}$ hypernucleus, and less than 0.85 GeV/ c corresponds to the continuum region of the Λ and Σ state. The momentum corresponds to bound region of ${}^6_\Lambda\text{H}$ is well covered by the SKS spectrometer.

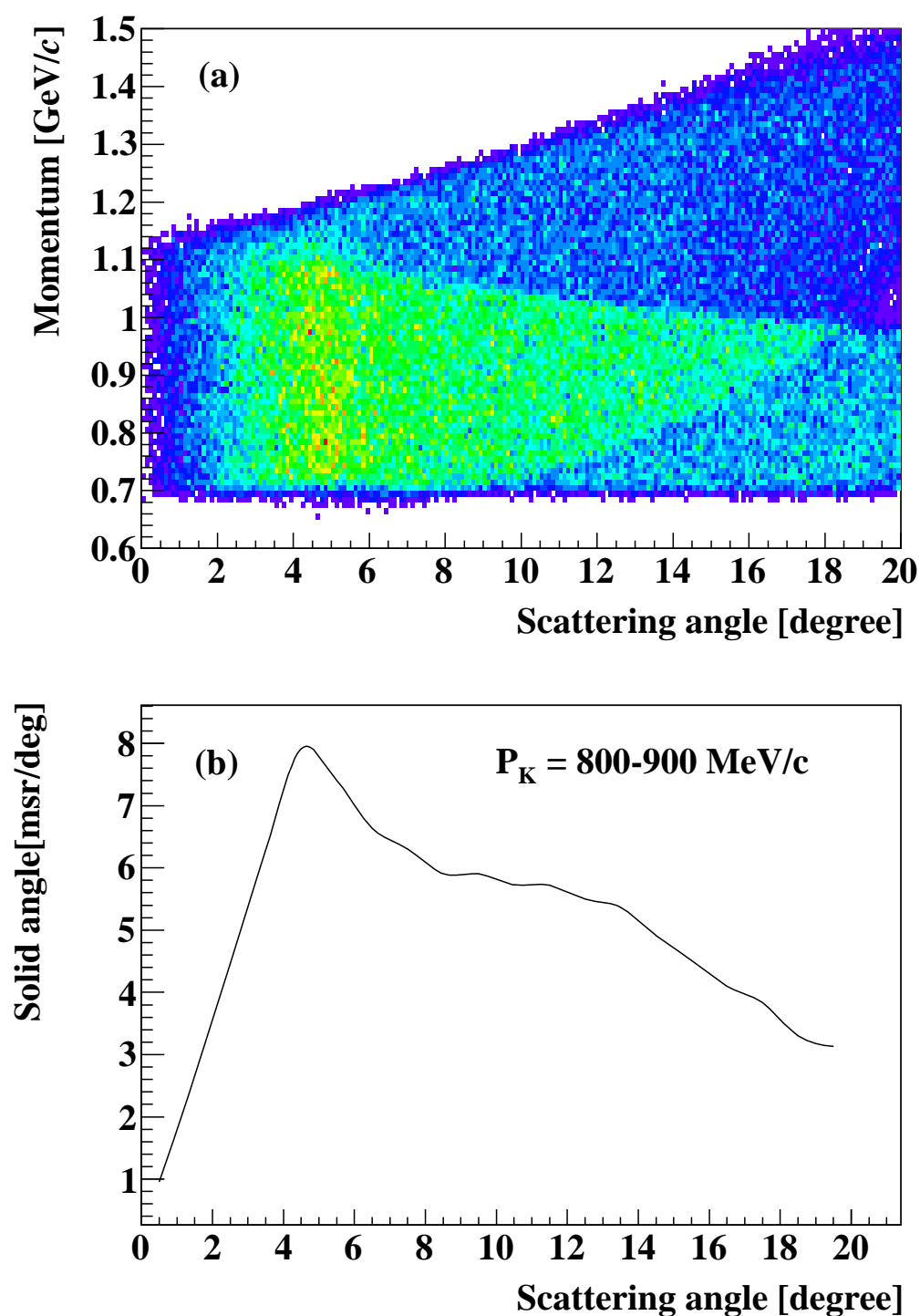
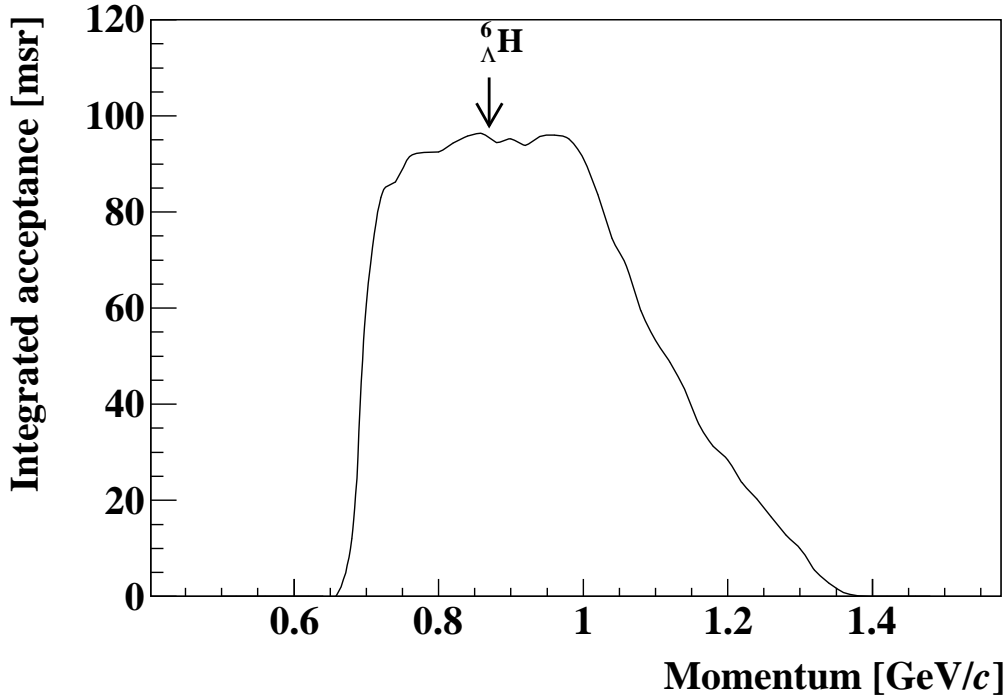


Figure 4.9: The acceptance of SKS in the 2.2 T mode. It shows the total acceptance with TOF and LC matrix combination trigger selection. (a) : The scattering angle vs momentum plot. The acceptance is represented by the arbitrary unit (number of triggered event in the simulation.). (b) : Solid angle per deg in the region of $p_K = 800-900$ MeV/c as a function of scattering angle.

Figure 4.10: The integrated acceptance from 2° to 14°

4.4 Missing-mass spectrum of the ${}^6\text{Li}(\pi^-, K^+)$ reaction

As mentioned in Sec.3.1, missing mass was obtained from this expression.

$$M = \sqrt{(E_\pi + M_A - E_K)^2 - (p_\pi^2 + p_K^2 - 2p_\pi p_K \cos \theta_{\pi K})},$$

p_π and p_K were used corrected value which is described in Sec.3.6.4 and Sec.3.6.2. E_π and E_K were used energy loss corrected value at the target with Bethe-Bloch formula.

The double differential cross section is defined as

$$\frac{d^2\sigma}{d\Omega dM} = \frac{A}{N_A \cdot \rho x} \cdot \frac{n_K}{N_{\text{beam}} \cdot \Delta\Omega \cdot \Delta M \cdot \epsilon}, \quad (4.1)$$

where n_K is the number of detected kaons in the missing-mass interval ΔM . ϵ is the over all experimental efficiency described in Sec.4.2. Where, $\epsilon_{skstrack}$ and ϵ_{vertex} are corrected with event by event in each θ . $\Delta\Omega$ is also scaled with SKS acceptance in each θ . The other values are constant of all runs.

Figure 4.11 (a) shows the missing-mass spectrum of the ${}^6\text{Li}(\pi^-, K^+)$ reaction at the momentum of 1.2 GeV/c in the experimental counts per 1 MeV/c². Figure 4.11 (b) shows the missing-mass spectrum of the double differential cross section of the laboratory frame, $d^2\bar{\sigma}_{lab}/d\Omega/dM$ in a unit of nb/sr/(MeV/c²). Both spectra are selected the scattering angle from 2° to 14° in the laboratory frame because the estimation of the spectrometer acceptance has small ambiguity in the angular range. The uncertainty of the missing

mass scale is $\pm 1.26 \text{ MeV}/c^2$ which is estimated from the beam momentum uncertainty $\pm 1.34 \text{ MeV}/c$. The continuum of the unbound Λ formation reaction and the component of the Σ^- quasi-free production reaction are observed in the missing-mass range of 5810–5880 MeV/c^2 and above 5880 MeV/c^2 , respectively. A magnified view in the missing-mass range of 5795–5830 MeV/c^2 is shown in the inset. Around the ${}^4_{\Lambda}\text{H}+2n$ particle decay threshold indicated by the arrow (5801.7 MeV/c^2), no significant peak structure is observed.

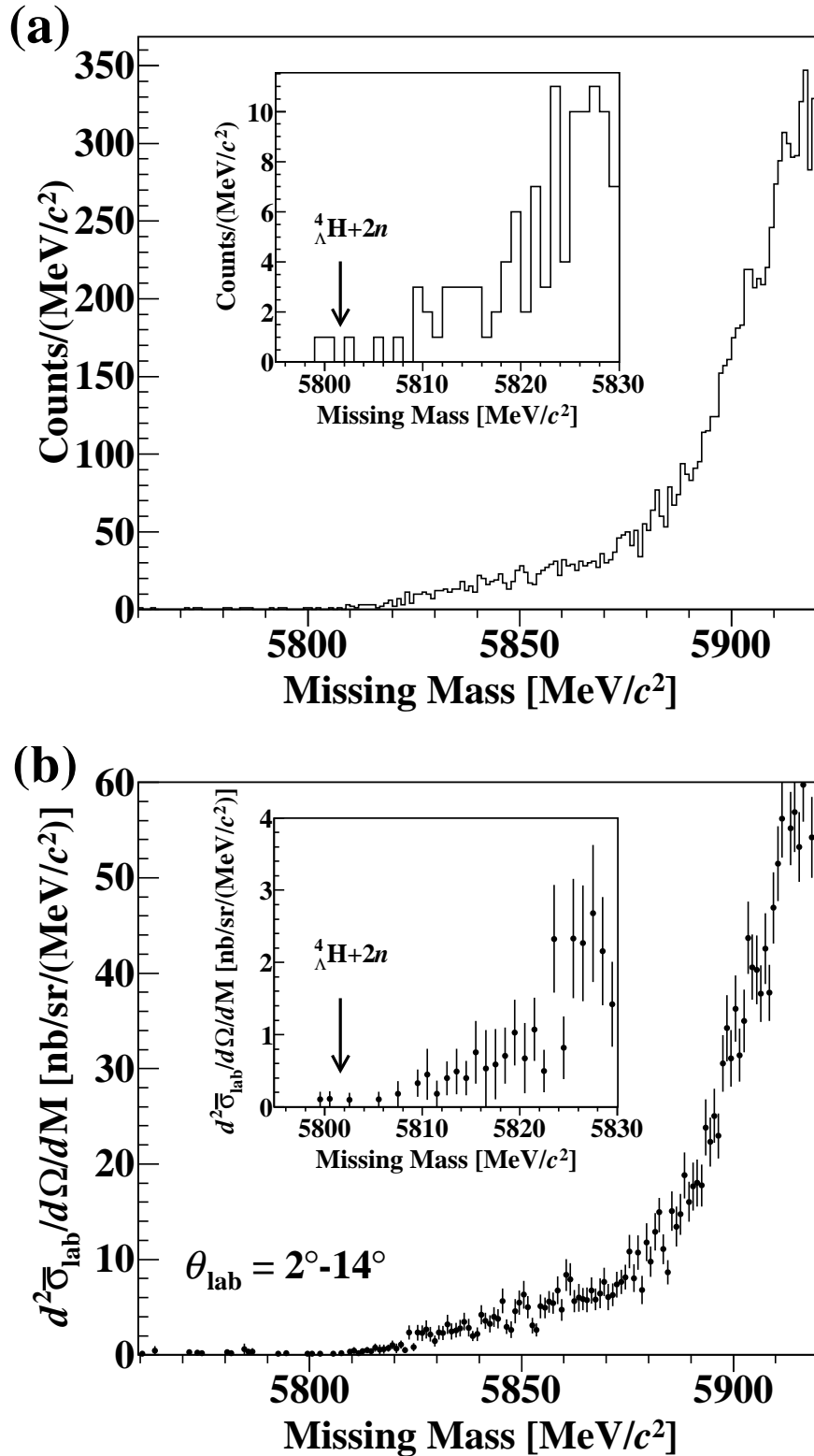


Figure 4.11: (a) The missing-mass acceptance uncorrected spectrum of the ${}^6\text{Li}(\pi^-, K^+)$ reaction at the momentum of $1.2 \text{ GeV}/c$. (b) The missing-mass acceptance corrected spectrum.

Chapter 5

Discussions

5.1 Analysis of ${}^{12}_{\Lambda}\text{C}$

In order to evaluate the missing-mass resolution in a kinematical condition close to that of the ${}^6\text{Li}(\pi^-, K^+)_{\Lambda}{}^6\text{H}$ reaction, we measured the ${}^{12}\text{C}(\pi^+, K^+)_{\Lambda}{}^{12}\text{C}$ reaction at the momentum of 1.2 GeV/ c . A graphite target of 3.6 g/cm² in thickness was used, and the beam intensity was 4.1×10^6 pions/spill. Figure 5.1 shows the excitation energy spectrum of the ${}^{12}_{\Lambda}\text{C}$ hypernucleus obtained from the measurement. Although it is not acceptance corrected, the acceptance is almost flat in the excitation energy between -5 MeV and 10 MeV. The ground (s_{Λ}) and excited (p_{Λ}) states were clearly observed. The ground state region was fitted with three Gaussian distributions corresponding to the ground and to known excited states at 2.833 MeV and 6.050 MeV [62]. A same width of the Gaussian function is used for the three states. The missing-mass resolution is estimated to be 3.23 ± 0.02 MeV in FWHM for the ${}^6\text{Li}(\pi^-, K^+)_{\Lambda}{}^6\text{H}$.

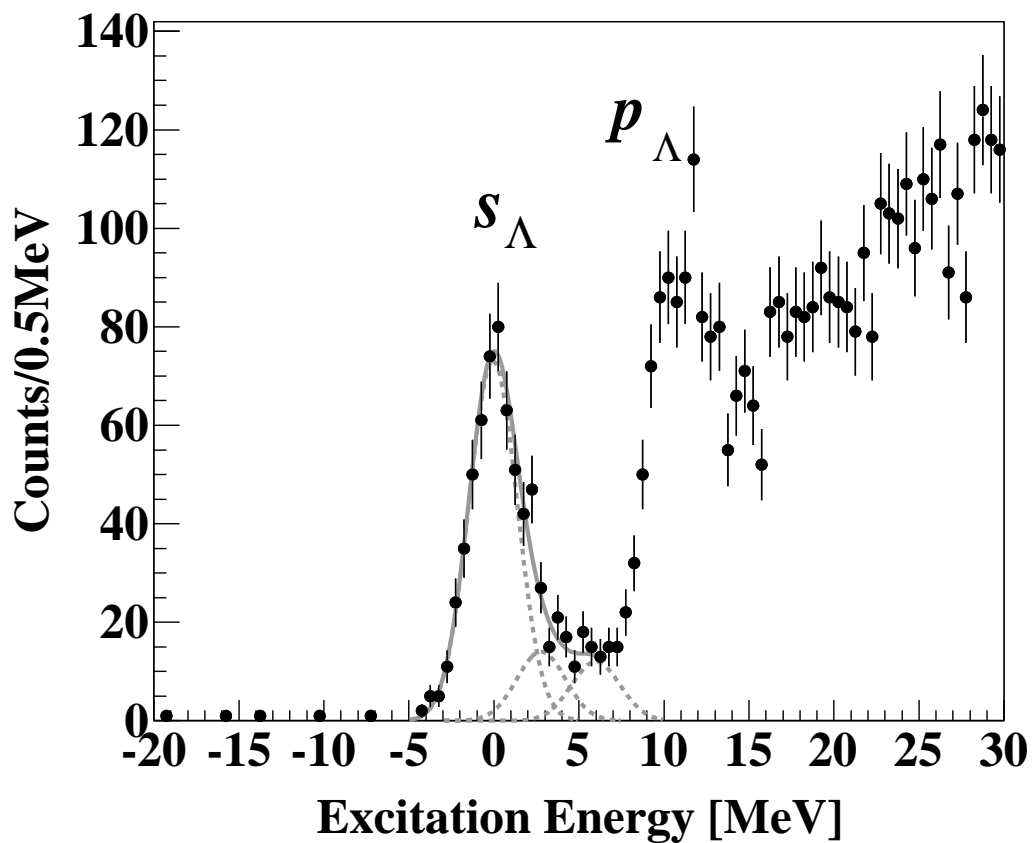


Figure 5.1: Excitation energy spectrum of the $^{12}C(\pi^+, K^+)_{\Lambda}^{12}C$ reaction at the momentum of 1.2 GeV/c. The ground s_{Λ} and excited p_{Λ} states are clearly observed. The missing mass resolution is estimated by fitting the ground and known excited states. The dashed curves show the best fit Gaussian functions for these states and the solid curve is the sum.

5.2 Analysis of the Σ^\pm

We measured the $p(\pi^-, K^+)\Sigma^-$ and the $p(\pi^+, K^+)\Sigma^+$ reactions at 1.377 GeV/c to calibrate the beam momentum with a $(\text{CH}_2)_n$ target of 3.4 g/cm² in thickness. The pion beam momentum of 1.377 GeV/c was selected so that the produced K^+ momentum in the $p(\pi^\pm, K^+)\Sigma^\pm$ reaction coincides with that in the ${}^6\text{Li}(\pi^-, K^+){}_\Lambda^6\text{H}$ reaction at 1.2 GeV/c. The beam intensities in the Σ^- and Σ^+ production runs were 1.3×10^7 and 3.5×10^6 pions/spill, respectively. Figure 5.2 shows the missing mass spectrum for Σ^+ and Σ^- . The peaks of Σ^+ and Σ^- were clearly observed. The background around the peak of Σ^+ was due to Λ quasi-free production from ${}^{12}\text{C}$ in $(\text{CH}_2)_n$. Since there was no difference of missing mass resolution between the Σ^+ and Σ^- production runs, 2.54 ± 0.03 MeV/c² in FWHM for both measurements, it is concluded that the beam rate dependence of the mass resolution is negligible. The differential cross section of the Σ^- production reac-

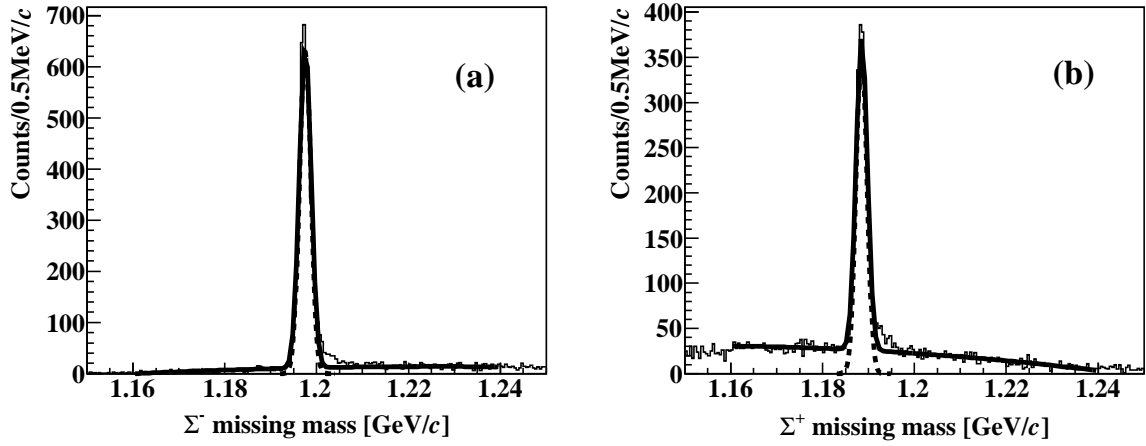


Figure 5.2: Missing-mass spectrum of Σ^\pm .

tion is shown in Fig. 5.3 as a function of the scattering angle in the laboratory frame. Figure. 5.4 shows the differential cross section of Σ^+ production after subtracting the Λ quasi-free events by linear fit. Figure 5.5 and Figure 5.6 shows the integrated differential cross section, $d\sigma/d\Omega_{\text{cm}}$, in the center of mass frame (full circle) in the angular range of $\cos\theta_{\text{cm}} = 0.8-1.0$ for the $\pi^- p \rightarrow K^+\Sigma^-$ reaction. The cross section is compared with the cross sections previously reported by Good et al. [63] (open circles) and Dahl et al. [64] (open box). The differential cross sections gradually decrease with the increase of the π^- beam momentum. It seems the present result is consistent with the general trend.

Figure 5.6 shows the cross section for the $\pi^+ p \rightarrow K^+\Sigma^+$ reaction, which is also compared with an old reported data by Candlin et al. [65]. It increases gradually with the increase of the π^+ beam momentum, and the present result is consistent with the general trend. From these comparison, we estimate the systematic error of the present cross section measurement is 10%.

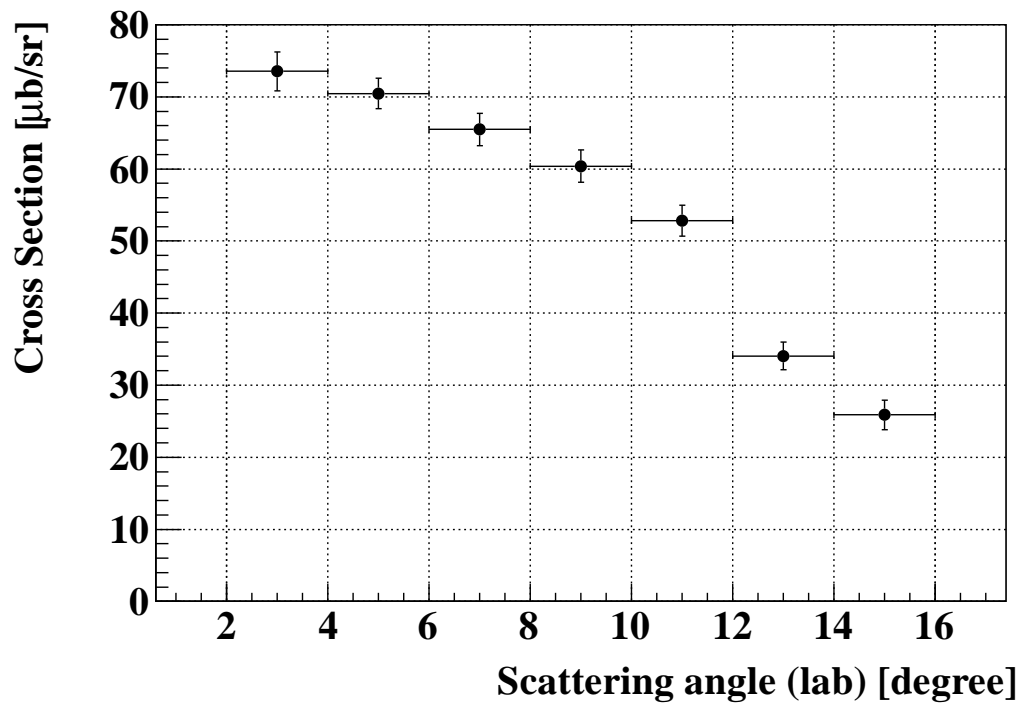


Figure 5.3: The differential cross section of the Σ^- production as a function of the scattering angle.

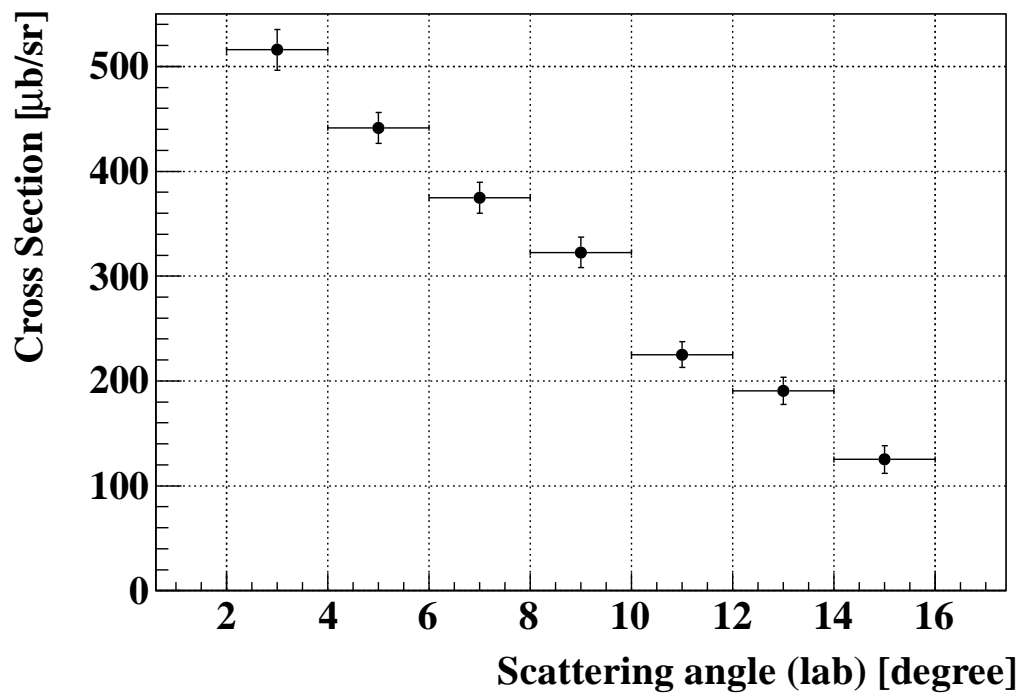


Figure 5.4: The differential cross section of Σ^+ production as a function of the scattering angle.

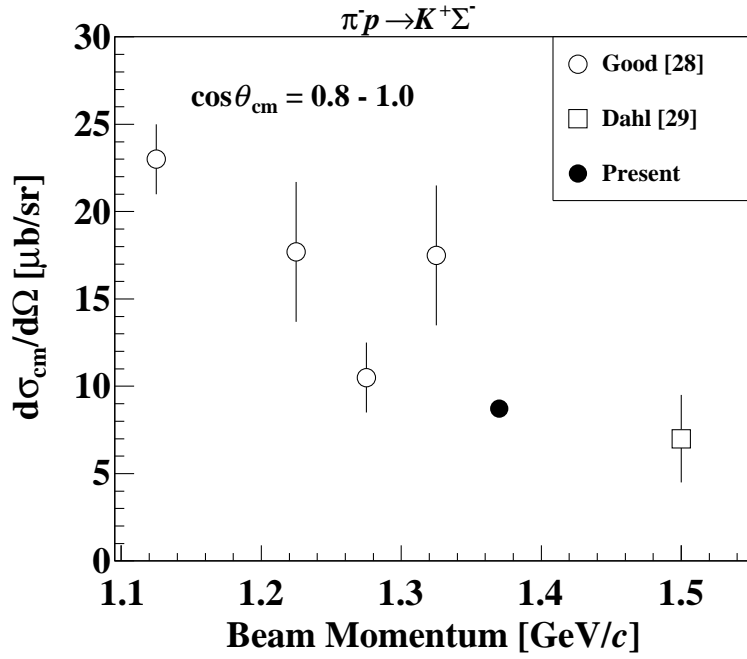


Figure 5.5: The differential cross section of the Σ^- production compared with old experiments as a function of the π^- beam momentum.

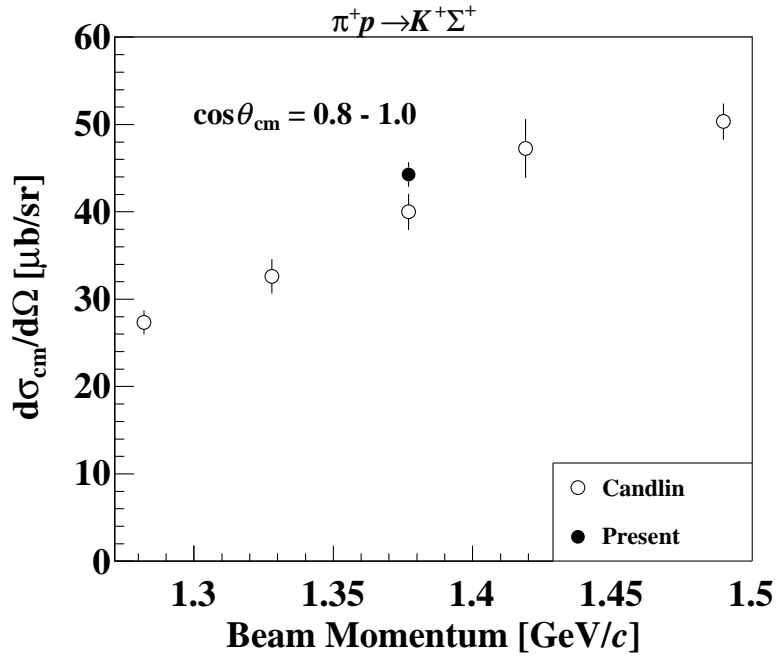


Figure 5.6: The differential cross section of the Σ^+ production compared with an old experimental data as a function of the π^+ beam momentum.

5.3 Background level

In order to estimate the statistical significance of a small peak structure in the hypernuclear mass spectra, we need to understand the background level in the spectrum. In the present analysis, it was estimated with several procedures. The over bound region (5790–5802 MeV/ c^2) means the region where the binding energy is larger than that for the ground state of a produced Λ hypernucleus. Accordingly, the yield in this region means the background level if existed. Figure 5.7 shows a ${}^6\text{Li}(\pi^-, K^+)$ spectrum in the over bound regions with three different cut parameter conditions in mass squared resolution, χ_{sks}^2 and vertex. We found the main component of background comes from particle miss-identification in the mass squared cut. As shown in Fig. 3.14, high intensity beam causes different start timings after the true start timing. In that case, time-of-flight from BH2 to TOF is faster than the true timing, which causes the particle miss-identification. In the present analysis, background level in the region of 5700 to 5780 MeV/ c^2 was estimated to be 0.39 ± 0.05 events per MeV/ c^2 .

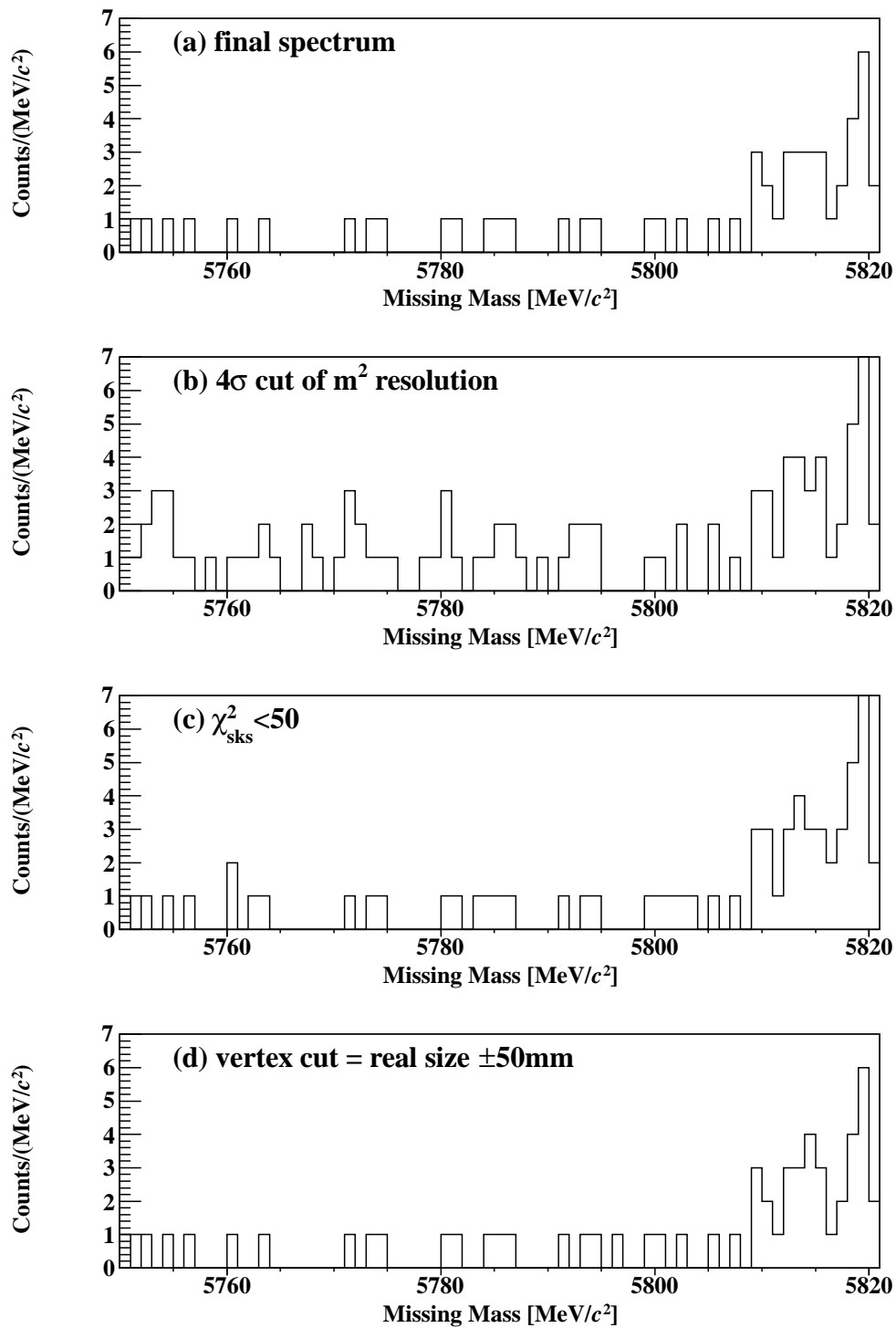


Figure 5.7: Background level in the over bound regions of the ${}^6\text{Li}(\pi^-, K^+)$ reaction in the final analysis (a); (b)–(d) are the same histograms with loosened cut conditions in mass squared resolution, χ^2_{sks} and vertex cut

5.4 Estimation of upper limit

As a first step of the calculation of an upper limit of the differential cross section, $d\bar{\sigma}_{lab}/d\Omega$, for a state of ${}^6_{\Lambda}\text{H}$, we estimated the number of observed events in the missing-mass region around the ${}^4_{\Lambda}\text{H}+2n$ threshold. For the estimation of the number of events associated to the production of a state, we set a missing-mass window of $\pm 2\sigma$, 5.44 MeV/ c^2 , in the missing-mass region. There were 3 events in the threshold region within the missing-mass window. Therefore, we interpret the 3 events as observed events which include background and possible signal events.

Another necessary information for the upper limit estimation is the number of background events. Population of events are observed in the missing-mass region lower than 5780 MeV/ c^2 where we do not expect any physical backgrounds. The level of the event population is 0.39 ± 0.05 events per 1 MeV/ c^2 in average. These events are instrumental background due to particle miss-identifications. We assumed a similar level of backgrounds at the ${}^4_{\Lambda}\text{H}+2n$ threshold. The number of background events was estimated by multiplying the average background level with the width of the missing-mass window.

If Poisson statistics is applied, the upper limit of the number of signal events is estimated to be 4.80 at 90 % confidence level. Although we assumed a flat distribution of the background events, the missing-mass dependence of the background level is not observed well due to the low statistics. Therefore, we employ another upper limit of 6.68 events coming from the background free hypothesis as a conservative estimation.

As shown in Fig 4.11, the differential cross sections are roughly 0.1 nb/sr for 1 event for the observed 3 events. However, the differential cross sections largely depend on the observed scattering angles and may have a statistical bias. If an event happens to be observed at the forward angle, the cross section is underestimated, and vice versa, in our set up. To avoid the bias of the observation, we estimate the differential cross section averaged over the selected angular range from 2° to 14° , and we obtain a value of 0.18 nb/sr for 1 event. By using the value, the upper limit of the differential cross section averaged in the scattering angle from 2° to 14° is estimated to be 1.2 nb/sr at 90% confidence level.

5.5 Structure of ${}^6_{\Lambda}\text{H}$

In our ${}^6\text{Li}(\pi^-, K^+)$ spectrum in Fig. 4.11, neither significant peak structure nor a large yield is observed around the ${}^4_{\Lambda}\text{H}+2n$ particle decay threshold in the ${}^6\text{Li}(\pi^-, K^+)$ reaction. The ${}^6_{\Lambda}\text{H}$ hypernucleus is believed to have the ${}^4_{\Lambda}\text{H}+2n$ structure dominantly and have the 0^+ ground and the 1^+ excited states which are analogous to the 0^+ and 1^+ spin-doublets in ${}^4_{\Lambda}\text{H}$. Our reaction should favor the 1^+ state direct population at forward angles, because the dominant spin non-flip amplitude of the (π^-, K^+) reaction would not change the spin of ${}^6_{\Lambda}\text{H}$ with the same spin of ${}^6\text{Li}$. We summarized three kinds of scenarios about ${}^6_{\Lambda}\text{H}$ structure as shown in Fig 5.8. As far as the FINUDA result is concerned [66], the observed ${}^6_{\Lambda}\text{H}$ candidate events were interpreted as the primary population of the excited 1^+ state by the $(K_{\text{stopped}}^-, \pi^+)$ reaction followed by the γ -ray transition to the ground 0^+ state because the direct population of the 0^+ state should be suppressed due to the small spin-flip amplitude in the $(K_{\text{stopped}}^-, \pi^+)$ reaction. The FINUDA results indicate that the excited 1^+ state, whose excitation energy is considered to be about 1 MeV, should be particle bound, otherwise the γ -ray transition to the 0^+ ground state should be impossible. If the 1^+ state was bound and the production cross section was comparable with that for ${}^{10}_{\Lambda}\text{Li}$ of 11.3 nb/sr, more than 60 events should be observed as a peak in the Λ bound region in the missing-mass spectrum of the ${}^6\text{Li}(\pi^-, K^+)$ reaction. Therefore, our observation is in conflict with the simple interpretation of the FINUDA observation.

Hiyama et al. [41] suggested that both 0^+ and 1^+ states are unbound. If it is the case, production cross sections may be smaller than the sensitivity of our measurement due to the broad wave-functions of the unbound states which should have a small overlap with the wave-function in the initial ${}^6\text{Li}$ nucleus.

Gal and Millener [40] discussed another possible interpretation of the FINUDA observation. They suggested a possibility of an unbound 1^+ state, whose particle decay width is extremely small and comparable with that of the $M1$ γ decay to the ground 0^+ state due to kinematical and dynamical suppression of the emission of two neutrons from the 1^+ excited state.

The FINUDA collaboration also discussed another scenario for the spectrum of ${}^6_{\Lambda}\text{H}$ in which two out of the three candidate events came from the population of the spin-triplet states, 1^+ , 2^+ and 3^+ , at around 3 MeV excitation [66]. Therefore, it is interesting to compare our upper limit, 1.2 nb/sr, with quantitative theoretical estimations of the production cross sections because the cross sections are sensitive to the binding energies and the wave-functions of the low-lying states.

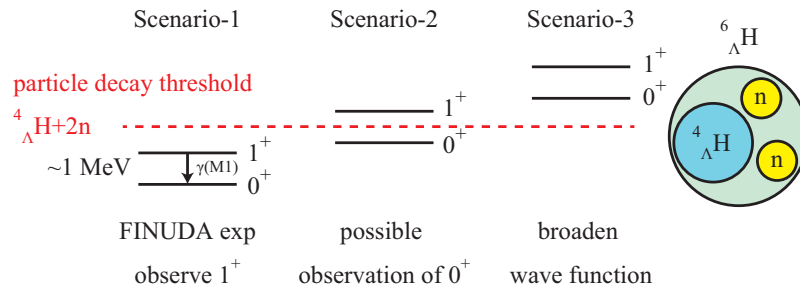


Figure 5.8: Level structure of ${}^6_{\Lambda}\text{H}$ with respect to the particle decay threshold of ${}^4_{\Lambda}\text{H}+2n$.

Chapter 6

Conclusion

We have performed the measurement of ${}^6\text{Li}(\pi^-, K^+)$ reaction at a beam momentum of 1.2 GeV/ c and the missing-mass spectrum was obtained for the first time. To evaluate the missing-mass resolution of ${}^6\text{Li}(\pi^-, K^+)$ reaction, we have also measured ${}^6_{\Lambda}\text{C}$ production with the ${}^{12}\text{C}(\pi^+, K^+)$ reaction. A clear peak structure was observed in the bound region, and the missing-mass resolution was estimated to be 3.23 ± 0.02 MeV/ c^2 . The Σ^\pm productions by the $p(\pi^\pm, K^+)$ reactions were measured to calibrate the absolute mass scale. For both Σ^- and Σ^+ productions, the production cross section was consistent with old experimental data. The momentum correction uncertainty was estimated to be 1.34 MeV/ c which corresponds to 1.26 MeV/ c^2 in the absolute mass uncertainty.

In the missing-mass spectrum of the ${}^6\text{Li}(\pi^-, K^+)$ reaction, no significant peak structure was observed around the ${}^4_{\Lambda}\text{H}+2n$ threshold. There were 3 events in the threshold region within the missing-mass window. Therefore, we interpret the 3 events as observed events which include background and possible signal events. The background level was estimated to be 0.39 ± 0.05 events per 1 MeV/ c^2 by evaluating the unphysical missing-mass region in the missing mass of 5700–5780 MeV/ c^2 . When the Poisson statistics is applied, we obtained the upper limit of 4.80 events at the 90% confidence level, and 6.68 events in the case of background free assumption.

The differential cross section per event was 0.18 ± 0.02 nb/sr under the average over the selected angular range from 2° to 14° . Therefore the upper limit of the differential cross section in the scattering angle from 2° to 14° is estimated to be 1.2 nb/sr at the 90% confidence level.

Our result did not favor a simple interpretation of the FINUDA observation that both 0^+ and 1^+ states of ${}^6_{\Lambda}\text{H}$ are bound. It suggests that reconsideration of the structure of the ${}^6_{\Lambda}\text{H}$ hypernucleus as well as ${}^5\text{H}$ would be needed. It is a key to fully understand whether the 1^+ excited state is bound or not.

Acknowledgements

First of all, I would like to acknowledge the J-PARC E10 collaborators and every person I had a fortune to work with. If there were not for their contribution and advices, I would have never been able to complete this work.

I would like to express my great thanks to Prof. Tomofumi Nagae, who has been my supervisor at Kyoto University. He gave me a chance to research hypernuclei. He always encouraged to me helpful suggestion about not only physics but also my life.

During my research at graduate school, I almost spent and worked at J-PARC. Especially, I belonged to Advance Science Research Center (ASRC) of Japan Atomic Energy Agency (JAEA) during doctor course. I applicate to Prof. Ken'ichi Imai, who has my supervisor at ASRC. He always encouraged me with his warm advice and vivid sense for physics when I had a trouble in the experiment and data analysis. I have also learned from him about attitudes to the physical research as a physicist.

I would like to express my great thank to Prof. Atsushi Sakaguchi, who is the spokesperson of the J-PARC E10 experiment. When I was second degree of doctor course, I expressed him that I want to write with a result of E10 experiment. He kindly accepted my request, and made me the great part of J-PARC E10 experiment. I discussed with him so many times about experimental preparation and data analysis. Thanks to him, I could get a good result of J-PARC E10 experiment.

I would like to thank to experimental preparation work together with Mr. S. Hayakawa, Mr. R. Ota, Ms. M. Nakagawa and Mr. T. Soyama. I enjoyed and spent them. I could not carry out the experiment without their great contributions. It was indeed a great pleasure to work with them. For the construction of LAC, I would like to applicate to Mr. K. Matsuoka, Mr. T. Tanaka, Mr. K. Yoshida, who made a great effort the construction.

I would like to acknowledge the Dr. Kotaro Shiotori and Mr. Tomonori Takahashi. They were pioneers of K1.8 beam line group. I have learned from them not only many experimental techniques and analyses but also how to survive the J-PARC life.

I would like to greatly acknowledge the Hyperball group members. Prof. H. Tamura, Prof. T. Koike, Dr. M. Ukai, Dr. K. Miwa suggested me the plan of experimental preparation work, and I learned the experimental techniques from them. I would applicate Mr. R. Honda, who worked together with me during preparation. He introduced some new systems, Mass trigger, EASIROC, Fiber tracker. Were not for him, the experiment would not succeed. I would like to thank Mr. T.O. Yamamoto, Mr. Y. Sasaki, Mr. Y. Akazawa, Mr. K. Tanabe, Mr. Y. Yamamoto and Mr. T. Shiozaki for taking the E10 experimental shift.

I have spent my graduate school days as a member of the "Experimental Nuclear and

Hadronic Physics Laboratory (NH)”. I wish to acknowledge the help and encouragement by Prof. Takahiro Kawabata, Prof. Megumi Naruki, Dr. Tetsuya Murakami, Dr. Masayuki Niiyama and Dr. Hiroyuki Fujioka. I would like to express my great thanks to Dr. A.O. Tokiyasu, Mr. M. Moritsu and Mr. Y. Ichikawa. I worked K1.8 beam line construction with them. After the earthquake, two new members, Mr. S. Kanatsuki and Mr. H. Ekawa participated in reconstruction of K1.8 beam line. They helped us and made good efforts. For E10 experiments, Mr. N. Amano helped us to take a shift.

I have joined two experiment, J-PARC E19 and E27. I would address my thanks to all the members of J-PARC E19 and E27 collaboration. I could not complete this thesis work without their great effort.

The present experiment was made possible by the staffs of J-PARC and KEK. I would like to express my great thanks to the Hadron beam channel group, accelerator group and electronics group for their strong support for the experiment. Especially, I would like to appreciate to Prof. Toshiyuki Takahashi and Prof. Masaharu Ieiri to plan the schedule of beam time based on our request.

Finally, but not the least, I want to express my sincere gratitude to my parents, Tsuneo Sugimura and Yachiyo Sugimura.

Appendix A

Missing-mass spectrum of the ${}^6\text{Li}(\pi^-, K^+)$ reaction

The missing-mass spectrum of the ${}^6\text{Li}(\pi^-, K^+)$ reaction is shown in Fig.4.1 are presented as table in Table A.1. The quoted values of M are the centers of the bins.

Table A.1: The missing-mass spectrum of the ${}^6\text{Li}(\pi^-, K^+)$ reaction as a table

M (MeV/ c^2)	Cross section (nb/sr/(MeV/ c^2))	error
5.7805	0.261516	0.261516
5.7815	0.170215	0.170215
5.7825	-	-
5.7835	-	-
5.7845	0.589593	0.589593
5.7855	0.308068	0.308068
5.7865	0.342676	0.342676
5.7875	-	-
5.7885	-	-
5.7895	-	-
5.7905	-	-
5.7915	-	-
5.7925	0.104584	0.104584
5.7935	-	-
5.7945	0.197870	0.197870
5.7955	-	-
5.7965	-	-
5.7975	-	-
5.7985	-	-
5.7995	0.104559	0.104559
5.8005	0.108269	0.108269
5.8015	-	-
5.8025	0.098477	0.098477

M (MeV/c ²)	Cross section (nb/sr/(MeV/c ²))	error
5.8035	-	-
5.8045	-	-
5.8055	0.103825	0.103825
5.8065	-	-
5.8075	0.179096	0.179096
5.8085	-	-
5.8095	0.325925	0.188481
5.8105	0.449910	0.352849
5.8115	0.182671	0.182671
5.8125	0.395366	0.234316
5.8135	0.489352	0.312158
5.8145	0.396608	0.238876
5.8155	0.754853	0.436248
5.8165	0.533196	0.533196
5.8175	0.590120	0.488420
5.8185	0.709881	0.388345
5.8195	1.02689	0.454379
5.8205	0.673250	0.486807
5.8215	1.07305	0.437719
5.8225	0.496787	0.293376
5.8235	2.32697	0.744588
5.8245	0.819468	0.435082
5.8255	2.33014	0.828373
5.8265	2.26743	0.801049
5.8275	2.68054	0.949193
5.8285	2.15475	0.749864
5.8295	1.42254	0.586638
5.8305	2.33893	0.746463
5.8315	2.30281	0.736015
5.8325	3.19736	0.995696
5.8335	2.44683	0.865902
5.8345	2.57790	0.777335
5.8355	2.77793	0.881818
5.8365	3.46666	0.931516
5.8375	2.84105	0.925927
5.8385	1.99716	0.533171
5.8395	2.16059	0.739589
5.8405	4.20301	1.02601
5.8415	3.57399	0.864990
5.8425	3.25384	0.919864
5.8435	3.97098	1.03070
5.8445	3.79696	1.00140
5.8455	5.65548	1.32041
5.8465	2.94090	0.765158

98 APPENDIX A. MISSING-MASS SPECTRUM OF THE ${}^6\text{Li}(\pi^-, K^+)$ REACTION

M (MeV/ c^2)	Cross section (nb/sr/(MeV/ c^2))	error
5.8475	2.62424	0.865682
5.8485	4.59302	1.26970
5.8495	5.44791	1.27135
5.8505	6.30463	1.45576
5.8515	4.97309	1.16659
5.8525	3.06908	0.820089
5.8535	2.60092	0.683837
5.8545	5.08681	1.24657
5.8555	4.92305	1.08983
5.8565	5.55673	1.15272
5.8575	5.42241	1.10359
5.8585	6.76361	1.46104
5.8595	4.70967	1.13872
5.8605	8.37088	1.66527
5.8615	7.93109	1.69320
5.8625	5.62511	1.14676
5.8635	5.98901	1.45607
5.8645	5.82849	1.17543
5.8655	5.75540	1.28771
5.8665	6.75213	1.39380
5.8675	5.80457	1.13888
5.8685	6.44626	1.56303
5.8695	7.63998	1.48310
5.8705	6.04636	1.37347
5.8715	6.29386	1.21563
5.8725	7.35880	1.36258
5.8735	7.66088	1.27017
5.8745	8.14266	1.30887
5.8755	10.8407	1.73948
5.8765	8.04116	1.44520
5.8775	10.7107	1.81752
5.8785	6.80287	1.48018
5.8795	11.7969	1.97306
5.8805	9.75552	1.59309
5.8815	12.8948	1.97793
5.8825	14.9469	2.12047
5.8835	11.0865	1.56808
5.8845	8.64651	1.28232
5.8855	15.0740	2.06657
5.8865	13.4330	2.08694
5.8875	14.7249	2.12751
5.8885	18.8072	2.40380
5.8895	16.0272	2.09475
5.8905	17.6510	2.51655

M (MeV/ c^2)	Cross section (nb/sr/(MeV/ c^2))	error
5.8915	18.0245	2.46906
5.8925	17.7537	2.20348
5.8935	23.8277	2.93337
5.8945	22.3178	2.56707
5.8955	25.0563	2.81378
5.8965	22.9536	2.36004
5.8975	30.5418	2.97880
5.8985	34.2414	3.46362
5.8995	31.0684	2.97440
5.9005	36.2834	3.45551
5.9015	31.4122	2.77643
5.9025	35.0061	3.28644
5.9035	43.7021	3.79665
5.9045	40.6269	3.43175
5.9055	40.3594	3.60800
5.9065	37.8680	2.96893
5.9075	42.5734	3.72817
5.9085	37.9506	2.94243
5.9095	46.8424	3.75536
5.9105	51.4945	3.92490
5.9115	56.2153	4.12532
5.9125	60.5918	4.26411
5.9135	55.1737	3.84419
5.9145	56.8731	4.17269
5.9155	53.2186	3.65415
5.9165	59.7576	3.90035
5.9175	68.2275	4.36938
5.9185	54.2183	4.24307
5.9195	64.5318	4.75118

Bibliography

- [1] B. Povh, Prog. Part. Nucl. Phys. **18** (1987) 183.
- [2] R. Chrien, C. Dover, Ann, Rev. Nucl. Part. Sci. **39** (1989) 113.
- [3] H. Bando, T. Motoba, J. Zofka, Internat. J. Modern Phys. **21** (1990) 4021.
- [4] M. Danysz and J. Pniewski, Philos. Mag. **44** (1953) 348.
- [5] W. Brückner, *et al.*, Phys. Lett. B **55** (1975) 107.
- [6] M. May *et al.*, Phys. Rev. Lett. **47** (1981) 1106.
- [7] P.H. Pile *et al.*, Phys. Rev. Lett. **66** (1991) 2585.
- [8] W. Brückner, *et al.*, Phys. Lett. B **62** (1976) 481.
- [9] W. Brückner, *et al.*, Phys. Lett. B **79** (1978) 157.
- [10] R. Bertini *et al.*, Nucl. Phys. A **360** (1981) 315.
- [11] R.E. Chrien *et al.*, Phys. Lett. B **89** (1979) 31.
- [12] M. Akei *et al.*, Nucl. Phys. A **534** (1991) 478.
- [13] T. Hasegawa *et al.*, Phys. Rev. Lett. **74** (1995) 224.
- [14] T. Hasegawa *et al.*, Phys Rev. C **53** (1996) 1210.
- [15] H. Hotchi *et al.* (KEK E369 Collaboration), Phys. Rev. C **64** (2001) 044302.
- [16] H. Tamura *et al.* (KEK E419 Collaboration), Phys. Rev. Lett. **84** (2000) 5963.
- [17] T. Nagae *et al.*, Phys. Rev. Lett. **80** (1998) 1605.
- [18] H. Outa *et al.*, Prog. Theor. Phys. Suppl. **117** (1994) 117.
- [19] T. Harada *et al.*, Nucl. Phys. A**507** (1990) 715.
- [20] H. Noumi *et al.*, Phys. Rev. Lett **89** (2002) 072301.
- [21] B.F. Gibson, A. Goldberg and M.S. Weiss, Phys. Rev. C **6** (1972) 741.
- [22] M. Bedjidian *et al.*, Phys. Lett. B **62** (1976) 467.

- [23] M. Bedjidian *et al.*, Phys. Lett. B **83** (1979) 252.
- [24] K. Tanida *et al.*, Phys. Rev. Lett **86** (2001) 1982.
- [25] H. Akikawa *et al.*, Phys. Rev. Lett. **88** (2002) 082501.
- [26] H. Tamura *et al.*, Nucl. Phys. A**754** (2005) 58c.
- [27] Y. Miura *et al.*, Nucl. Phys A**754** (2005) 75c.
- [28] M. Ukai *et al.* (BNL E930 Collaboration), Phys. Rev. C **77** (2008) 054315.
- [29] Y. Akaishi, T. Harada, S. Shinmura, Khin Swe Myint, Phys. Rev. Lett. **84** (2000) 3539.
- [30] S. Sinmura, Y. Akaishi and T. Harada, Prog. Theor. Phys. **65**, 1290 (1981).
- [31] L. Majling, Nucl. Phys. A **585** (1995) 211c.
- [32] K. Kubota *et al.*, Nucl. Phys. A **602** (1996) 327.
- [33] M. Agnello *et al.* (FINUDA Collaboration), Phys. Lett. B **640** (2006) 145.
- [34] M. Agnello *et al.* (FINUDA Collaboration), Phys. Rev. Lett. **108** (2012) 042501.
- [35] P.K. Saha *et al.* (KEK-E521 Collaboration), Phys. Rev. Lett. **94** (2005) 052502.
- [36] T. Fukuda *et al.*, Nucl. Instr. Meth. A **361** (1995) 485.
- [37] T. Harada, A. Umeya, and Y. Hirabayashi, Phys. Rev. C **79** (2009) 014603.
- [38] R.H. Dalitz and R. Levi Setti, Nuovo Cimento **30** (1963) 489.
- [39] Y. Akaishi and T. Yamazaki, Frascati Physics Series XVI (1999) 59.
- [40] A. Gal and D.J. Millener, Phys. Lett. B **725** (2013) 445.
- [41] E. Hiyama *et al.*, Nucl. Phys. A **908** (2013) 29.
- [42] A.A. Korshennikov *et al.*, Phys. Rev. Lett. **87** (2001) 092501.
- [43] M. Meister *et al.*, Nucl. Phys. A**723** (2003) 13.
- [44] Y.B. Gurov *et al.*, Eur. Phys. J. A **24** (2005) 231.
- [45] S. Nagamiya, Prog. Theor. Exp. Phys. **2012**, 02B001 (2012).
- [46] M. Ikegami, Prog. Theor. Exp. Phys. **2012**, 02B002 (2012).
- [47] H. Hotchi, Prog. Theor. Exp. Phys. **2012**, 02B003 (2012).
- [48] T. Koseki, Prog. Theor. Exp. Phys. **2012**, 02B004 (2012).

- [49] K.H. Tanaka *et al.*, The technical report of the hadron experimental facility, KEK internal 2007-1.
- [50] T. Takahashi *et al.*, Prog. Theor. Exp. Phys. **2012**, 02B010 (2012).
- [51] Digital Teslameter 151 (DTM-151), <http://www.group3technology.com/meters/dtm151.php>
- [52] RCNP-E384 Experiment,
http://www.rcnp.osaka-u.ac.jp/Divisions/plan/b-pac/ex_appro/summary/pdf/E384.pdf
- [53] R. Honda and K. Miwa, Proceedings of 3rd International Workshop on New Photon-Detectors, PoS Press, Orsay, 2012, p.031.
- [54] Y. Igarashi *et al.*, IEEE Trans. Nucl. Sci., vol**52**, 2866 (2005).
- [55] EFM-3000AX, http://echo-denshi.co.jp/nmr_magnetic.htm
- [56] <http://lambda.phys.tohoku.ac.jp/~takahasi/TUL-8040/>.
- [57] T.K. Ohsuka *et al.*, IEEE Trans. Nucl. Sci., vol**1** (1986) 98.
- [58] Z-86, <http://kokorowo.shop-pro.jp/?pid=6204691>
- [59] K.L. Brown, Ch. Iselin, D.C. Carey: Decay Turtle, CERN 74-2 (1974), Urs Rohrer: Compendium of Decay Turtle Enhancements.
- [60] S. Morinobu, private communication.
- [61] J. Myrheim and L. Bugge, Nucl. Instr. Meth. **160**, 43 (1979).
- [62] K. Hosomi *et al.* (KEK E566 Collaboration), Nucl. Phys. A **914** (2013) 184.
- [63] M.L. Good and R.R. Kofler, Phys. Rev. **183** (1969) 1142.
- [64] O.I. Dahl *et al.*, Phys. Rev. **163** (1967) 1430.
- [65] D.J. Candlin *et al.*, Nucl. Phys. B **226** (1983) 1.
- [66] M. Agnello *et al.* (FINUDA Collaboration), Nucl. Phys. A **881** (2012) 269.